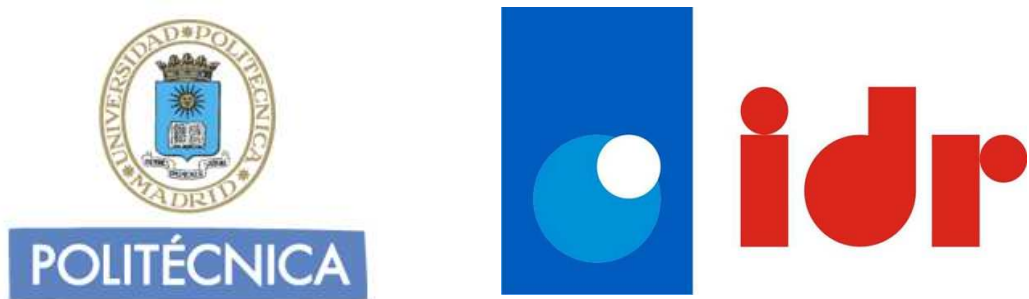


UNIVERSIDAD POLITÉCNICA
DE MADRID

INSTITUTO UNIVERSITARIO DE MICROGRAVEDAD
“IGNACIO DA RIVA”



TRABAJO FIN DE MÁSTER

**Estudio, diseño, y correlación de un modelo térmico en
ESATAN-TMS del sistema de control térmico del
proyecto TASEC-Lab**

Autor: JONATHAN MARTIN PALOMO

MÁSTER UNIVERSITARIO EN SISTEMAS ESPACIALES

SEPTIEMBRE 2021

(Page intentionally left blank).

Abstract

School of Aeronautical and Space Engineering

University Master's Degree in Space Systems

Study, design, and correlation of a thermal model in ESATAN-TMS of the thermal control system of the TASEC-Lab project.

by Jonathan MARTIN PALOMO

The Thermal Analysis Support and Environment Characterization Laboratory (TASEC-Lab) is an experiment designed to study the convection heat transfer, the thermal environment and the balloon dynamics during the ascent and float phases of a stratospheric balloon.

TASEC-Lab experiment has been designed, integrated and tested in the Universidad Politécnica de Madrid by bachelor, master and doctorate students and it consists of an aluminium structure of 130 x 130 x 330 mm with three compartments. The lower one contains the Electrical Power Subsystems, the upper one the Heat Transfer Laboratory and in the middle the Electronics. It also carries a cup anemometer to be tested at low pressure conditions in order to provide the relative speed of the balloon-gondola system in order to characterize the dynamics and the forced convection heat transfer.

One of the main systems in the experiment is the thermal control system. In order to design this system so that all the elements of the experiment are within the temperature range within which they must operate, a model of the experiment has been made using the ESATAN-TMS software, paying special attention to the characterization of the convective heat exchange that takes place between the different parts of the experiment and the air that surrounds them. For this, correlations have been used that allow characterizing this heat exchange from expressions obtained after carrying out empirical experiments.

Finally, once a complete model has been developed, it has been correlated using the data obtained after carrying out two Thermal Balance Tests, which have allowed to conclude that in general the model is adequately adjusted to the real behaviour of the experiment, but it must seek greater precision in the characterization of convective heat exchange.

(Page intentionally left blank).

Acknowledgements

The project carried out and which is reflected in the completion of this TFM has given me the opportunity to work on a real project and thus be able to know all its phases, from design to launch. For this I would like to thank all those who have made it possible.

First of all, I wanted to thank Alejandro, my professional tutor, who has taught me to use ESATAN from practically zero and has always been willing to help me with any problems that arose.

Also, to Lilian, Fernando and Manú, with whom I have worked so hard to carry out the thermal model of the experiment.

I must make a special mention to David González, the coordinator of the program, for the great work he has done so that it could be carried out successfully, as well as the rest of the members in charge of developing the rest of the subsystems.

I would like to thank the Ignacio da Riva Institute for allowing me to be present during the launch of the experiment, as it was a very enriching experience.

I also want to take this opportunity to dedicate my classmates, with whom I have worked for the last two years and from whom I have learned so much.

Finally, I want to thank my family and friends for supporting me at all times.

(Page intentionally left blank).

Contents

List of figures.....	IX
List of tables	XII
Abbreviations	XIV
Symbols	XV
Physical Constants	XVII
Introduction.....	2
Chapter 1. Theory introduction.....	4
1.1. Spatial thermal control.....	5
1.2. Heat transfer by conduction.	6
1.2.1. Problem statement.....	7
1.2.2. Conduction heat transfer - thermal properties.	8
1.3. Heat transfer by convection.	11
1.3.1. Boundary layer concept.	11
1.3.2. Nusselt Number	13
1.4. Heat transfer by radiation.	15
1.4.1. Thermal radiation.....	15
1.4.2. Blackbody radiation.....	16
1.4.3. Radiative properties.....	17
1.4.4. Kirchhoff's Law.....	20

1.4.5.Greybody	20
1.4.6.View factor	20
1.4.7.Radiative exchange between two surfaces	22
1.5. Spatial environment.....	23
1.5.1.Solar radiation	23
1.5.2.Albedo	24
1.5.3.Planetary infrared radiation.....	25
1.5.4.Re-radiation to Space	25
1.6. ESATAN-TMS software.....	26
1.7. References of this chapter.....	28
Chapter 2. Mission description	30
2.1. Introduction.....	31
2.2. Stratospheric balloons.....	32
2.2.1.Composition.....	32
2.2.2.Types of balloons	32
2.2.3.Materials and construction.....	33
2.2.4.Phases of flight	33
2.2.5.Main applications.....	35
2.3. TASEC-Lab description.....	36
2.4. References of this chapter.....	39

Chapter 3. Model description.....	40
3.1. Introduction.....	41
3.2. Geometrical model.....	42
3.2.1.Used materials and optical sets.....	42
3.2.2.Geometrical model components.....	44
3.2.3.Power dissipation.....	54
3.3. Mathematical model	55
3.3.1.Atmospheric nodes.....	55
3.3.2.Convective thermal couplings	56
3.3.3.Comparison with experimental results.	71
3.3.4.Thermal Environment.....	72
3.4. References of this chapter.....	76
Chapter 4. Vacuum chamber tests.....	78
4.1. Tests description.....	79
4.1.1.Thermal balance test (TBT).....	79
4.1.2.Low pressure functional test	80
4.2. TBT set up.....	81
4.2.1.Pressure profile	81
4.2.2.I/F boundary conditions	82
4.2.3.Temperature profile	83
4.2.4.Power dissipation profile.....	84
4.2.5.Thermocouples positions.....	86

4.2.6. Test Results.....	88
4.3. Functional test set up.....	91
Chapter 5. Model correlation.....	92
5.1. Introduction.....	93
5.2. ESATAN-TMS predicted results	95
5.2.1. Hot Operational Case	95
5.2.2. Cold Operational Case.....	97
5.3. Modified parameters in the model	99
5.4. Correlation of the thermal model.....	100
5.4.1. Temperature deviation.....	101
5.4.2. Average temperature deviation	105
5.4.3. Standard deviation of temperature	107
5.5. Correlation conclusions.....	109
5.6. References of this chapter.....	110
Conclusions and future work.....	112
Annex A	114
Annex B	118

List of figures

Figure 1.1: Environmental heat fluxes for a planet-orbiting spacecraft (from page 23 of [1]).	5
Figure 1.2: Temperature distribution along the x direction and its variation as a function of time and the direction of the heat flux qx .	6
Figure 1.3: Temperature distribution along the x direction at steady-state through a body and the direction of the heat flux qx .	7
Figure 1.4: Range of values of thermal conductivity for various states of matter at normal temperatures and pressures (adapted from page 61 of [2]).	8
Figure 1.5: Temperature distribution along the x direction at steady-state through two bodies in contact and the direction of the heat flux qx .	9
Figure 1.6: Velocity boundary layer development on a flat plate (adapted from page 349 of [2]).	11
Figure 1.7: Thermal boundary layer development on a flat plate (adapted from page 350 of [2]).	12
Figure 1.8: Heat transfer through a fluid layer (adapted from page 336 of [3]).	14
Figure 1.9: Spectrum of electromagnetic radiation (adapted from page 726 of [2]).	15
Figure 1.10: Intensity of radiation emitted from a differential area, dA . (adapted from page 76 of [1]).	18
Figure 1.11: The absorption, reflection, and transmission of incident thermal radiation by a semi-transparent material (adapted from page 582 of [3]).	19
Figure 1.12: View factor between two infinitesimal diffuse surfaces (from page 83 of [1]).	21
Figure 1.13: Solar spectral irradiance (adapted from page 135 of [4]).	23
Figure 1.14: ESATAN-TMS workbench window aspect (from ESATAN-TMS workbench user manual).	26
Figure 2.1: NASA balloon size comparison at launch and at float altitude (from [1]).	34
Figure 2.2: View of the electronics compartment, as well as the pressure sensors from the Environmental Lab (on the left).	36
Figure 2.3: View of the upper part of the TASEC-Lab, where it can see the four slots through which the air exchange with the environment occurs.	37
Figure 2.4: View of the gondola arm on which the anemometer is mounted.	38
Figure 2.5: View of the gondola with the two experiments integrated into the gondola.	38
Figure 3.1: Aspect of the interior of the model of the experiment carried out in ESATAN.	41
Figure 3.2: Distribution of the different materials in the model.	42
Figure 3.3: Distribution of the different optical sets in the model.	43

Figure 3.4: Picture of the frames [3]	44
Figure 3.5: Representation of the frames in ESATAN.....	44
Figure 3.6: ESATAN representation of the structure whit the trays.	45
Figure 3.7: Battery representation whit its Delrin support.....	47
Figure 3.8: PCBs representation over the Delrin base.	48
Figure 3.9: Converters representation.....	49
Figure 3.10: CAD representation of the plate and its support.....	50
Figure 3.11: ESATAN representation of the plate and its support.	50
Figure 3.12: CAD representation of the anemometer.....	51
Figure 3.13: Anemometer whit the heater attached.....	52
Figure 3.14: Position of the TASEC-Lab and the cup anemometer on the gondola.	53
Figure 3.15: Position of the interior atmospheric nodes.....	55
Figure 3.16: Correlations for vertical plates.....	61
Figure 3.17: Selected correlation for vertical plates.	62
Figure 3.18: Correlations for horizontal plates (Upper surfaces).....	65
Figure 3.19: Correlations for horizontal plates (Lower surfaces).....	66
Figure 3.20: Selected correlation for horizontal plates (Upper surfaces).....	67
Figure 3.21: Selected correlation for horizontal plates (Lower surfaces).....	67
Figure 3.22: Scheme showing the parameters which affect the system during the ascent phase (from [14])......	72
Figure 3.23: Density profile during the ascent of the balloon.....	74
Figure 3.24: Temperature profile during the ascent of the balloon.	74
Figure 4.1: Experiment in the vacuum chamber before the tests.....	79
Figure 4.2: Pressure profile of the TBT.....	81
Figure 4.3: Baseplate and shroud temperature profile of the TBT.	83
Figure 4.4: Plate heater power dissipation profile for the hot case.	85
Figure 4.5: Plate heater power dissipation profile for the cold case.	85
Figure 4.6: Temperature measurements during the hot case test.....	88
Figure 4.7: Temperature measurements of the plate and the air in the experiment compartment during the hot case test.....	89
Figure 4.8: Temperature measurements during the cold case test.	90
Figure 4.9: Temperature measurements of the plate and the air in the experiment compartment during the cold case test.....	90
Figure 5.1: Temperature margins defined in the ECSS standard (from [1])......	93
Figure 5.2: Temperature prediction during the hot case simulation.....	95
Figure 5.3: Temperature prediction of the plate and the air in the experiment compartment during the hot case simulation.	96
Figure 5.4: Temperature measurements of the plate and the air in the experiment compartment during the hot case test.....	96
Figure 5.5: Temperature prediction during the cold case simulation.	97

Figure 5.6: Temperature prediction of the plate and the air in the experiment compartment during the cold case simulation.....	98
Figure 5.7: Temperature measurements of the plate and the air in the experiment compartment during the cold case test.....	98
Figure 5.8: Temperature difference between the measured by the vacuum chamber thermocouples value and the predicted value at each instant of time during the hot case.	101
Figure 5.9: Temperature difference between the measured by the CubeSat thermocouples value and the predicted value at each instant of time during the hot case.	102
Figure 5.10: Temperature difference between the measured by the vacuum chamber thermocouples value and the predicted value at each instant of time during the cold case.	103
Figure 5.11: Temperature difference between the measured by the CubeSat thermocouples value and the predicted value at each instant of time during the cold case.	104
Figure A.1: Raspberry Pi 3B+ heat distribution (load) [2].....	114
Figure A.2: Raspberry Pi 3B+ heat distribution (idle) [2].....	114
Figure A.3: Achieved temperature distribution on the board (load).....	115
Figure A.4: Achieved temperature distribution on the board (idle).....	115

List of tables

Table 3.1: Properties of the materials used in the model.....	42
Table 3.2: Optical sets of the materials used in the model.	43
Table 3.3: Model details for frames.	45
Table 3.4: Thermal couplings for frames.	45
Table 3.5: Model details for trays.....	46
Table 3.6: Thermal couplings for trays.....	46
Table 3.7: Model details for the closure panels.	47
Table 3.8: Thermal couplings for the closure panels.	47
Table 3.9: Model details for the battery.....	48
Table 3.10: Thermal couplings for the battery.	48
Table 3.11: Model details for the PCBs.....	49
Table 3.12: Thermal couplings for the PCBs.....	49
Table 3.13: Model details for the HTL.	51
Table 3.14: Thermal couplings for the HTL.	51
Table 3.15: Model details for the anemometer.....	52
Table 3.16: Thermal couplings for the anemometer.....	52
Table 3.17: Model details for the Gondola.....	53
Table 3.18: Thermal couplings for the Gondola and the rest of the elements.	53
Table 3.19: Power Consumption of the different elements of the experiment.	54
Table 3.20: Value of the parameters m and n as a function of the Rayleigh number vertical surfaces.....	59
Table 3.21: Nusselt numbers as a function of the Rayleigh number for vertical plates.	60
Table 3.22: Range of each correlation for vertical surfaces.	62
Table 3.23: Nusselt numbers as a function of the Rayleigh number for horizontal plates.	63
Table 3.24: Value of the parameters m and n as a function of the Rayleigh number for horizontal surfaces (upper surface).....	64
Table 3.25: Value of the parameters m and n as a function of the Rayleigh number for horizontal surfaces (lower surface)	64
Table 3.26: Range of each correlation for horizontal surfaces.	68
Table 3.27: Nusselt numbers as a function of the Reynolds number for cylinders in cross flow.....	70
Table 3.28: Result comparison for different level pressures.....	71
Table 4.1: Calculated temperature of each interface for the hot and the cold case.	83
Table 4.2: Final temperature of each interface for the hot and the cold case.....	83
Table 4.3: Power Consumption of the different elements of the experiment.	84
Table 4.4: Position of each thermocouple on the elements of the experiment and vacuum	

chamber	86
Table 4.5: Position of each thermocouple of the CubeSat.....	87
Table 4.6: Heat Transfer Lab power consumption of each mode, end mode criterion and safety criterion.....	91
Table 5.1: Average temperature deviation of each vacuum chamber thermocouple sensor for the hot and the cold case.....	105
Table 5.2: Average temperature deviation of each CubeSat thermocouple sensor for the hot and the cold case.	106
Table 5.3: Standard deviation of temperature of each vacuum chamber thermocouple sensor for the hot and the cold case.	107
Table 5.4: Standard deviation of temperature of each CubeSat thermocouple sensor for the hot and the cold case.	108

Abbreviations

AM0	Air Mass 0
AM1.5	Air Mass 1.5
CAD	Computer-Aided Design
CFRP	Carbon Fibber-Reinforced Plastic
COC	Cold Operating Case
ECMWF	European Centre for Medium-Range Weather Forecasts
ECSS	European Cooperation for Space Standardization
ESA	European Space Agency
ESATAN-TMS	ESATAN Thermal Modelling Suite
GEO	Geosynchronous Equatorial Orbit
GPS	Global Positioning System
HOC	Hot Operating Case
HTL	Heat Transfer Laboratory
IMU	Inertial Measurement Unit
IR	Infrared
LDB	Long Duration Balloons
LEO	Low Earth Orbit
MARS	Meteorological Archival and Retrieval System
MCS	Monte Carlo Simulation
OLR	Outgoing Long Wave Radiation
PCB	Printed Circuit Board
SEA	Statistical Error Analysis
SLI	Single Layer Insulation
SZA	Solar Zenith Angle
TASEC-Lab	Thermal Analysis Support and Environment Characterization Laboratory
TBT	Thermal Balance Test
TVT	Thermal Vacuum Test

Symbols

A	Area	m^2
a	Albedo coefficient	—
C	Heat capacity	J/K
C_f	Friction coefficient	—
C_p	Specific heat	$\text{J}/(\text{kg} \cdot \text{K})$
E	Photon's energy	J
F	View factor	—
G	Incident radiation	W/m^2
G_s	Solar constant.	W/m^2
Gr	Grashof number	—
h	Thermal contact conductance	$\text{W}/(\text{m}^2 \cdot \text{K})$
h_c	Convection heat transfer coefficient	$\text{W}/(\text{m}^2 \cdot \text{K})$
I	Incident radiation intensity	$\text{W}/(\text{m}^2 \cdot \text{sr} \cdot \mu\text{m})$
k	Thermal conductivity	$\text{W}/(\text{m} \cdot \text{K})$
L	Distance	m
Nu	Nusselt number	—
Pr	Prandtl number	—
\dot{q}	Heat flux	W/m^2
\dot{Q}	heat flow	W
Ra	Rayleigh number	—
Re	Reynolds number	—
t	Time	s
T	Temperature	K or $^{\circ}\text{C}$

α	Absorptivity	—
ε	Emissivity	—
θ	Angle	rad
λ	Wavelength	μm
μ	Dynamic viscosity	$(\text{N} \cdot \text{s})/\text{m}^2$
ρ	Density	kg/m^3
ρ_r	Reflectance	—
τ	Transmittance	—
τ_s	Shear stress	N/m^2
v	Frequency	rad/s
φ	Angle	rad
ψ	Angle	rad

Physical Constants

c	Speed of light	$2.9979 \cdot 10^8$ m/s.
h	Planck's constant.	$6.6256 \cdot 10^{-34}$ J · s
σ	Stefan-Boltzmann's constant	$5.67 \cdot 10^{-8}$ W/(m ² · K ⁴)

(Page intentionally left blank).

Introduction

The objective of this document is to present the work carried out for the creation of a thermal model of the Thermal Analysis Support and Environment Characterization Laboratory (TASEC-Lab) experiment. TASEC-Lab is an experiment designed, integrated and tested in the Universidad Politécnica de Madrid by bachelor, master and doctorate students. The objective of this experiment is to characterize the heat exchange by convection during the ascent and the floating phase of a stratospheric balloon, as well as to characterize the dynamics of its flight.

For this purpose, first chapter of the document describes all the theoretical concepts that will be necessary to adequately understand the process of creation and correlation of the thermal model of the experiment, from the mechanisms of heat exchange by conduction, convection and radiation, to a brief description of the space environment or the utilities of ESATAN-TMS software.

In second chapter, a detailed description of the mission is made, starting with the stratospheric balloons, the types that exist, their characteristics, the typical phases of their flights, etc., to later describe in detail the TASEC-Lab.

The third chapter describes the thermal model created to simulate the behaviour of the experiment, describing both the geometric model created in ESATAN and the mathematical model, which includes the correlations that characterize the heat exchange by convection that takes place between the different geometries and the air that surrounds them. The mathematical model also includes the environmental model, that is, the pressure or temperature conditions of the atmosphere during the ascent or the value of the different solar charges that affect it.

The fourth chapter describes tests carried out in the vacuum chamber, which are a Thermal Balance Test (TBT) and a Low pressure functional test procedure (TPT), as well as the results obtained during these tests, especially those obtained from the TBT, since they will be the ones that will serve to correlate the model in the fifth and final chapter.

The correlation of the model is done following the criteria established by the ECSS standards in the fifth chapter, comparing the results obtained during the TBT and those obtained in the simulations carried out in ESATAN to finally decide if the model is valid and also, propose future lines of work and possible improvements model.

(Page intentionally left blank).

Chapter 1.

Theory introduction

1.1. Spatial thermal control.

A spacecraft is a system designed to meet specific requirements for the space mission that it must fulfil. Then, the conditions in which the system is going to operate must be studied, from the beginning of the design phase to the end of its life in orbit, so intermediate stages must also be considered, such as production, integration, tests, and launch.

The spatial thermal control refers to the task of maintaining the temperature of the spacecraft, and therefore of all its subsystems, equipment, payloads, and in general all its elements, within an operational range that allows them to perform their function during the entire mission without failures. Therefore, the thermal control of a spacecraft is essential to ensure its long-term survival.

The main external heat fluxes to the spacecraft are shown in Figure 1.1, but the heat produced by the operation of their own equipment must also be taken into account. In addition, the exterior surfaces will evacuate heat to the exterior. This implies that the spacecraft will not have a uniform temperature, so in general, it will be necessary to study each surface separately depending on its position during the orbit and its mode of operation, so in most cases, it is necessary to evacuate heat from the parts that tend to overheat and heat those whose temperature may be below their operating range, facilitating the flow of heat between them.

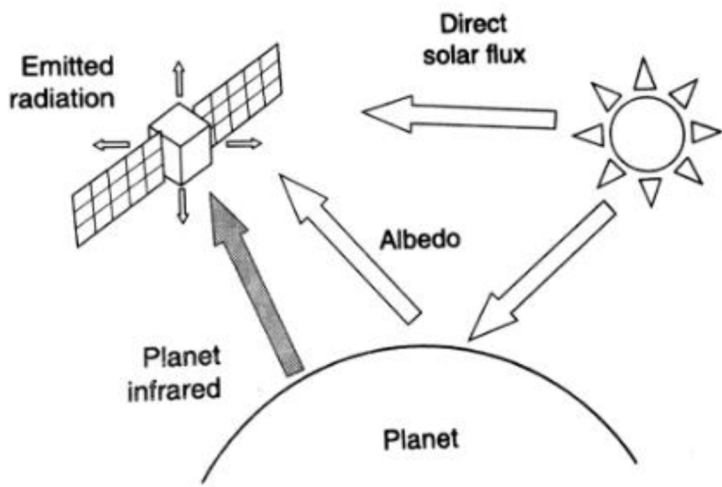


Figure 1.1: Environmental heat fluxes for a planet-orbiting spacecraft (from page 23 of [1]).

Therefore, the thermal control of a spacecraft is based on the study of the different heat flows existing in it, how these affect the temperature of each element, and the design solutions that allow these temperatures to be maintained within their operating range.

1.2. Heat transfer by conduction.

Conduction is a mechanism of heat transfer from the hottest parts of a body to the coldest ones, (but also between different bodies in contact) by which internal energy is transmitted between particles that are in contact within a body. Therefore, it is an interaction at the atomic and molecular level.

When a particle has a higher temperature it also has a higher energy level, so the collisions that occur constantly between neighbouring particles cause a transfer of energy between them. This means that when there is a temperature gradient, heat transfer occurs in the decreasing direction of that gradient, as can be seen in Figure 1.2.

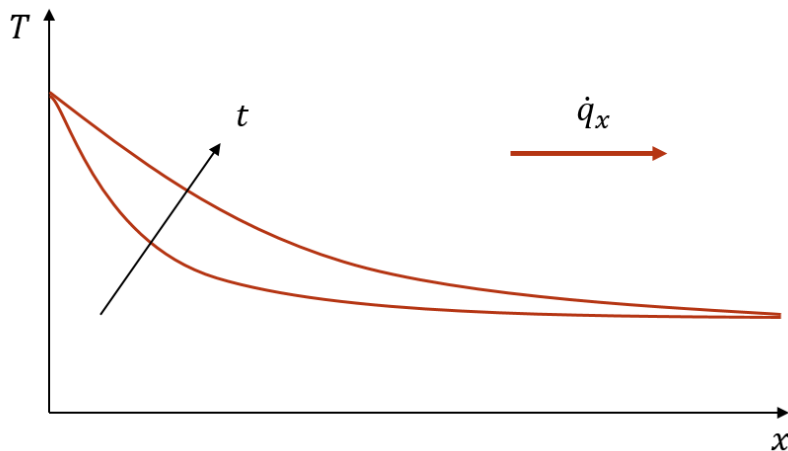


Figure 1.2: Temperature distribution along the x direction and its variation as a function of time and the direction of the heat flux \dot{q}_x .

Conduction is therefore a heat transfer mechanism that occurs in all materials, regardless of their properties or their state. However, conduction is a heat transfer mechanism that occurs mainly in solids, since convection also acts in gases and liquids, a mechanism that will later deepen.

In the case of fluids (gases and liquids), conduction can only be considered when talking about a closed volume, when it is only interesting to know the heat flow from one surface to another through a fluid, regardless of what happens inside of it.

1.2.1. Problem statement.

Heat flow can be quantified using the appropriate rate equations, equations that allow the amount of energy transferred per unit of time to be calculated. For conduction, the rate equations used are Fourier's Laws. For a unidirectional temperature gradient, the rate equation can be expressed as:

$$\dot{Q}_x = -k \cdot A \cdot \frac{dT}{dx} \quad [\text{W}] \quad (1.1)$$

where \dot{Q}_x is the heat flow in x direction [W], k is the thermal conductivity [W/(m · K)], A is the area in the normal direction to the heat flow [m^2] and dT/dx is the temperature gradient in x direction [K/m].

Equation (1.1) allows to calculate the heat flow through an area. In steady-state conditions, to calculate the heat flow between two surfaces of area A , at temperatures T_1 and T_2 respectively and separated by a distance L , that equation can be expressed as:

$$\dot{Q}_x = k \cdot A \cdot \frac{T_1 - T_2}{L} \quad [\text{W}] \quad (1.2)$$

where $T_1 > T_2$. As can be seen in Figure 1.3, when the steady-state is reached the temperature distribution inside the body is linear.

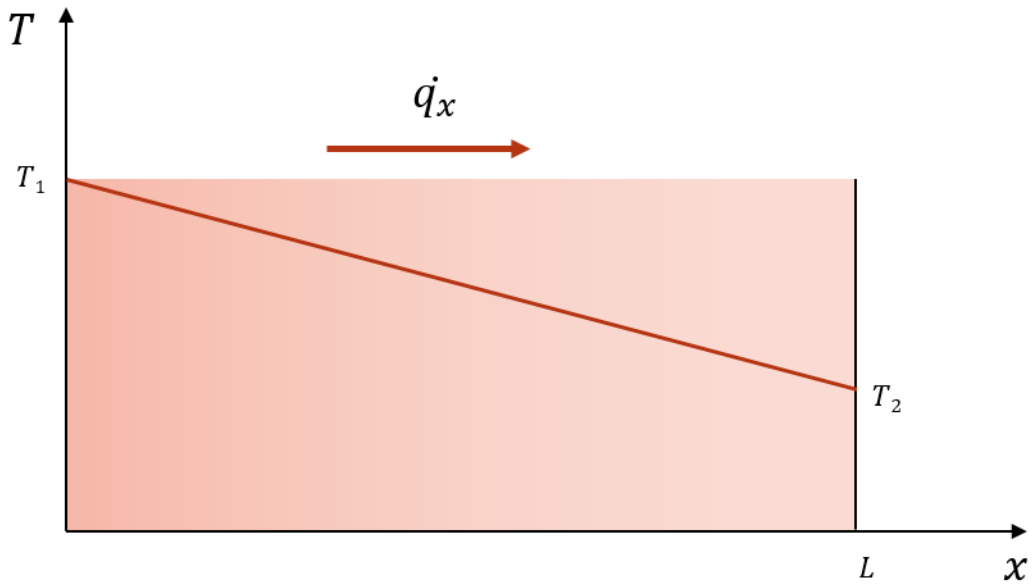


Figure 1.3: Temperature distribution along the x direction at steady-state through a body and the direction of the heat flux \dot{q}_x .

1.2.2. Conduction heat transfer - thermal properties.

Thermal conductivity

Thermal conductivity, k , is the ability of a material to transmit heat. It is determined as the amount of heat that passes through a certain material, per unit time through a unit area, and causes a temperature gradient between two opposite faces of $1\text{ }^{\circ}\text{C}$, per unit distance, in the direction of the heat flow. Assuming that this heat flow is in the x direction, the thermal conductivity can be expressed as:

$$k_x = -\frac{\dot{Q}_x/A}{\partial T/\partial x} \quad [\text{W}/(\text{m} \cdot \text{K})] \quad (1.3)$$

In orthotropic materials, this property can vary depending on the direction considered (something that commonly occurs in composite material laminates). However, in isotropic materials, this property is independent of the direction in which the heat flow moves within the material, so it can be considered that $k_x = k_y = k_z = k$.

From Equation (1.3) it can be deduced that as the thermal conductivity of a material decreases, the temperature gradient that exists within it increases (thermal insulators), while if it has a high thermal conductivity, the material will have a uniform temperature (metals). In general, gases have a reduced thermal conductivity, being less than that of liquids which is less than that of solids, as can be seen in the Figure 1.4. This tendency is explained by the separation that exists between the particles depending on the state of the substance, since this parameter determines the amount of heat that is transferred by conduction.

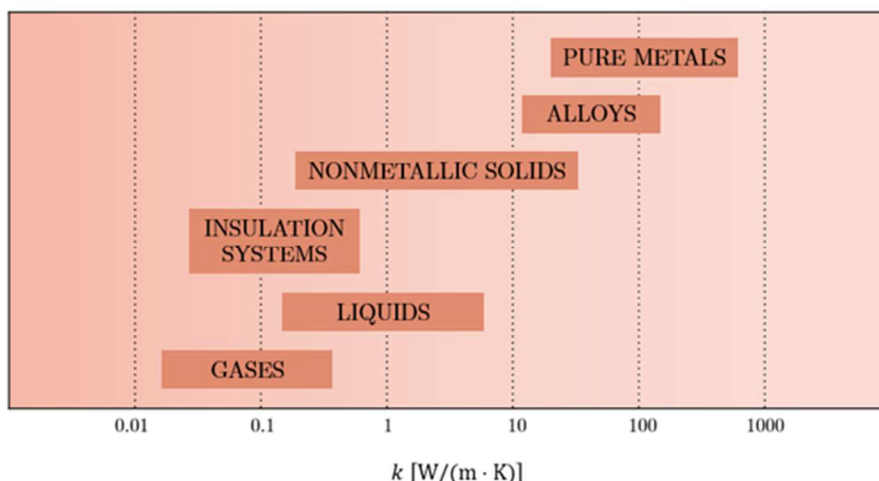


Figure 1.4: Range of values of thermal conductivity for various states of matter at normal temperatures and pressures (adapted from page 61 of [2]).

Thermal contact conductance

Thermal contact conductance, h , is the capacity to transmit heat between two different bodies that are in contact. The value of this property increases as the contact between bodies improves, tending to infinity in the case of perfectly joined bodies. Developing Equation (1.1) for the case shown in Figure 1.5, the heat that passes through two bodies in contact can be expressed as:

$$\dot{Q}_x = \frac{T_1 - T_3}{\frac{L_a}{k_a \cdot A} + \frac{1}{h \cdot A} + \frac{L_b}{k_b \cdot A}} \quad [W] \quad (1.4)$$

where \dot{Q}_x is the heat flow in x direction [W], k_a and k_b is the thermal conductivity of each body [W/(m · K)], h is the thermal contact conductance [W/(m² · K)], L_a and L_b the dimension of each body and $T_1 - T_3$ the temperature gradient at each end of the two bodies in x direction [K].

In Figure 1.5 it can be seen that there is a temperature jump in the contact area between the two bodies, which will depend on the value of the thermal contact conductance. In addition, the slope that follows the distribution of temperatures within each of the bodies will depend on their properties.

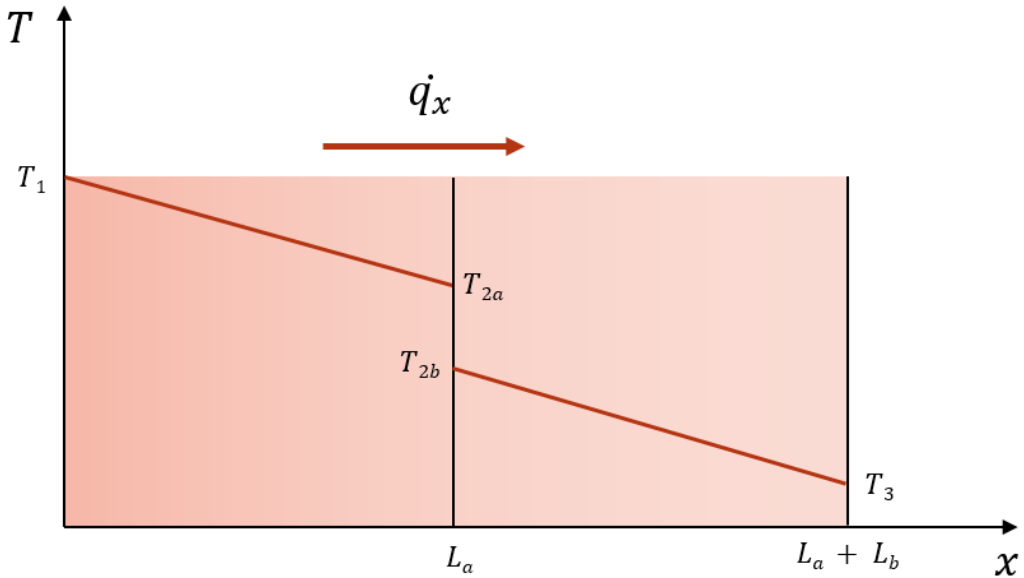


Figure 1.5: Temperature distribution along the x direction at steady-state through two bodies in contact and the direction of the heat flux \dot{q}_x .

There are some factors that determine the value of the thermal contact conductance:

- **Contact pressure:** it is the factor that most affects the contact conductance, as its value increases as the pressure increases. This implies that, for example, screwed interfaces will have a capacity to transmit a greater heat flow the tighter these screws are, since in this way the microscopic distance between the faces in contact of each body is reduced.
- **Interstitial materials:** the nature of the materials that can exist between the two bodies can also affect the flow of heat that is transmitted. These materials can be adhesives that join the two faces, thermal pastes that improve the ability to transfer heat or simply impurities or dirt.
- **Surface deformations:** When one of the two surfaces in contact is elastically or plastically deformed, the contact area increases and, therefore, the contact conductance increases too. This deformation can be caused, for example, by forces acting on one of the bodies, or by an inadequate tightening of the screws.
- **Roughness, cleanliness and surface finish:** the properties of the surface in contact also have an influence on the value of the contact conductance.

1.3. Heat transfer by convection.

Conduction is the most common heat transmission mechanism in solids or, in general, any medium within its particles remain practically immobile (as in quiescent fluids). However, in the presence of any other type of fluid in which there is a bulk fluid motion or a random motion of fluid molecules (conduction and diffusion), convection must be taken into account. This means that conduction in a fluid is a limiting case of convection in which there is no movement of particles inside it.

Convection implies a faster heat exchange than conduction, since as the fluid in contact with a surface heats up, it moves, causing parts of the fluid whose temperature is lower to come into contact with the surface.

The fluid displacement may be due to the buoyancy effect or the fact that the fluid itself is in motion. This allows the convection to be classified as natural or forced.

1.3.1. Boundary layer concept.

In order to define how heat exchange occurs by convection, it is necessary to first define the concept of boundary layer. However, the velocity boundary layer and the thermal boundary layer must be defined separately, since their characteristics are different.

The Velocity Boundary Layer.

To define the concept of boundary layer, a fluid flow is considered over a flat plate, as can be seen in Figure 1.6. The particles of the fluid that are in contact with the surface are assumed to have zero velocity, so these particles tend to slow down the rest of the fluid particles that come into contact with them in the layers furthest from the surface. The thickness of the boundary layer, $\delta(x)$, is the distance between the surface and the part of the fluid where the previous effect is negligible ($u = 0.99 \cdot u_\infty$ [2]).

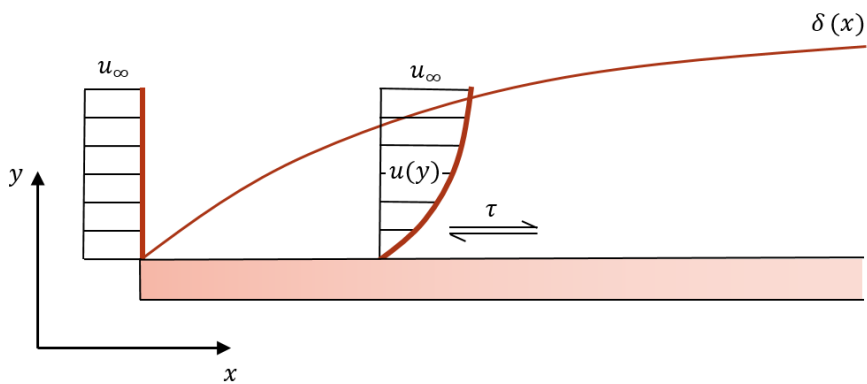


Figure 1.6: Velocity boundary layer development on a flat plate (adapted from page 349 of [2])

This effect by which the particles that are in contact with the surface act to retard the motion of particles in the adjoining fluid layer is associated with shear stresses, τ , which act in planes parallel to the surface. In this way, as the fluid is further from the surface, in the y -axis direction, its velocity increases until its velocity is equal to that of the free stream. This is what is known as the boundary layer velocity profile, $u(y)$.

In Figure 1.6 it can also be observed that the thickness of the boundary layer increases in the direction of the x -axis, which is due to the fact that the effects of the viscosity of the fluid penetrate further into it. The friction coefficient defines the effect that the viscosity of a fluid will have on its behaviour when it is in contact with a surface as follows:

$$C_f = \frac{\tau_s}{\rho \cdot u_\infty^2 / 2} \quad [-] \quad (1.5)$$

where τ_s is the surface shear stress, ρ the density of the fluid and u_∞ the velocity of the free stream. Assuming a Newtonian fluid the value of the surface shear stress can be calculated as knowing the velocity gradient at the surface:

$$\tau_s = \mu \cdot \frac{\partial u}{\partial y} \Big|_{y=0} \quad [N/m^2] \quad (1.6)$$

where μ is the dynamic viscosity of the fluid.

The Thermal Boundary Layer.

As with the velocity boundary layer, the thermal boundary layer appears when a fluid passes next to a surface that is at a different temperature. Considering a fluid flow over a isothermal flat plate, as can be seen in Figure 1.7, the particles of the fluid that are in contact with the plate achieve a thermal equilibrium with it and cause a temperature gradient between the temperature of the plate and that of the fluid free steam.

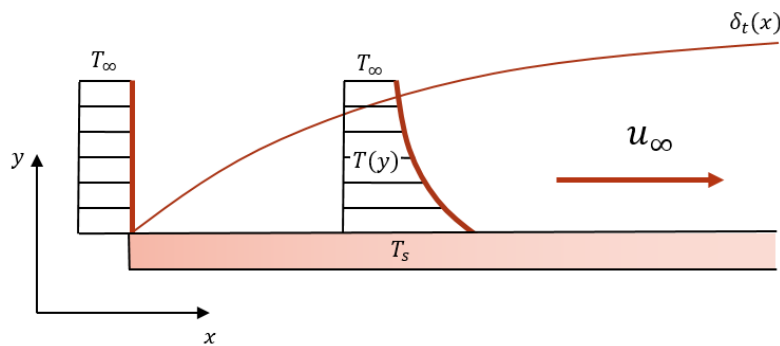


Figure 1.7: Thermal boundary layer development on a flat plate (adapted from page 350 of [2]).

Generally, the thickness of the thermal boundary layer, $\delta_t(x)$, is defined using the ratio $(T_s - T)/(T_s - T_\infty) = 0.99$ [2]. As the fluid advances in the direction of the x -axis, the boundary layer penetrates further into the fluid, as it happens with the velocity boundary layer.

The heat flux that exists at any distance in the direction of the x -axis can be calculated by applying Fourier's law to the fluid when $y = 0$, obtaining the following expression:

$$\dot{q}_s = -k \cdot \frac{\partial T}{\partial y} \Big|_{y=0} \quad [\text{W/m}^2] \quad (1.7)$$

As can be seen, on the surface heat is transmitted by conduction, since that part of the fluid is not in motion. The subscript s is used to emphasize that this heat flow occurs at the surface. Using Newton's law of cooling, this flux can be expressed as:

$$\dot{q}_s = h_c \cdot (T_s - T_\infty) \quad [\text{W/m}^2] \quad (1.8)$$

where h_c is the thermal contact conductance between the surface and the fluid or convection heat transfer coefficient. Combining the Equation (1.7) with the Equation (1.8) it can be obtained the value of h_c :

$$h_c = \frac{-k \cdot \frac{\partial T}{\partial y} \Big|_{y=0}}{T_s - T_\infty} \quad [\text{W}/(\text{m}^2 \cdot \text{K})] \quad (1.9)$$

This expression allows to observe that the calculation of the convection coefficient is not easy, since measuring the gradient in the thermal boundary layer is extremely difficult. Also, this value varies with the distance along the x -axis.

1.3.2. Nusselt Number

In studies related to convection, the use of dimensionless numbers is common to reduce the number of variables used. The Nusselt number allows to dimensionless the convection coefficient, and is defined as:

$$\text{Nu} = \frac{h_c \cdot L_c}{k} \quad [-] \quad (1.10)$$

where L_c is the characteristic length and k the thermal conductivity of the fluid.

To understand the physical meaning of the Nusselt number, a fluid layer of thickness L will be considered, within there is a difference of temperatures $\Delta T = T_2 - T_1$, as shown in the Figure 1.8.

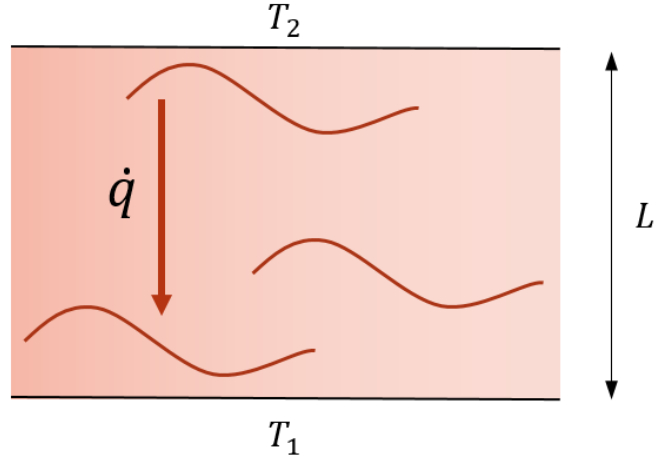


Figure 1.8: Heat transfer through a fluid layer (adapted from page 336 of [3]).

The value of the flow that is produced by convection is obtained using the expression of Equation (1.11), while the value that would occur if the fluid layer had no movement, that is, by conduction, using the expression of Equation (1.12).

$$\dot{q}_{conv} = h_c \cdot \Delta T \quad [\text{W/m}^2] \quad (1.11)$$

$$\dot{q}_{cond} = k \cdot \frac{\Delta T}{L} \quad [\text{W/m}^2] \quad (1.12)$$

Taking their ratio, it results:

$$\frac{\dot{q}_{conv}}{\dot{q}_{cond}} = \frac{h_c \cdot \Delta T}{k \cdot \Delta T / L} = \frac{h_c \cdot L}{k} = \text{Nu} \quad [-] \quad (1.13)$$

Therefore, the Nusselt number represents the enhancement of heat transfer through a fluid layer as a result of convection relative to conduction across the same fluid layer.

1.4. Heat transfer by radiation.

The previously described heat transfer mechanisms (conduction and convection) require a material medium for the heat flow to exist, however, radiation does not require the existence of matter. This is the reason why solar radiation is able to transmit through a vacuum. The complete spectrum of radiation can be seen in Figure 1.9. In this figure it can be seen that there are different types of radiation whose nature will depend on the mechanism that produces it.

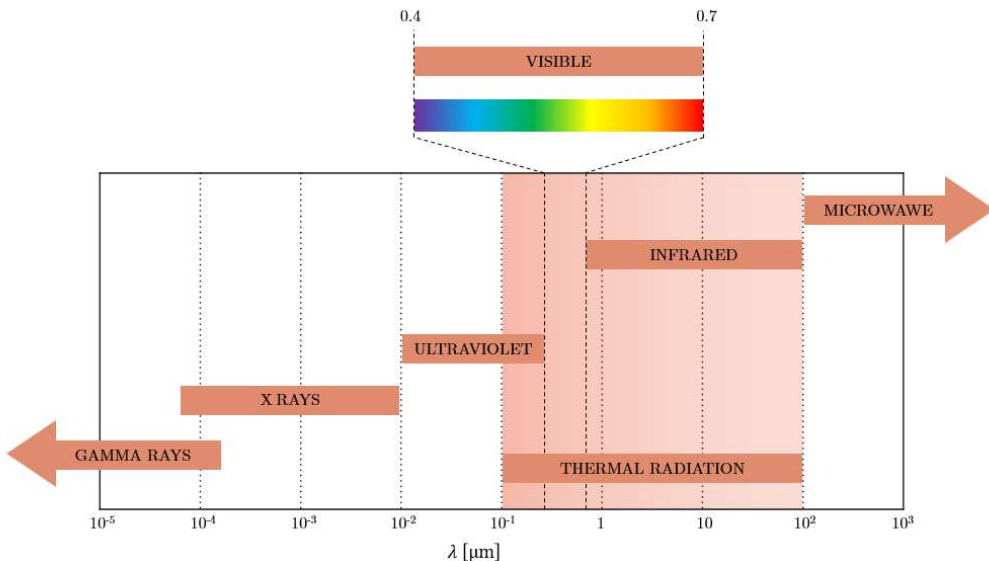


Figure 1.9: Spectrum of electromagnetic radiation (adapted from page 726 of [2])

As can be seen in the Figure 1.9, only part of the spectrum of electromagnetic radiation causes thermal heat transfer. This part of the spectrum, which has a range between $0.1 \mu\text{m}$ and $100 \mu\text{m}$, is called thermal radiation because it is caused by and affects the thermal state of matter. It includes part of the ultraviolet band, the visible light and the infrared band.

1.4.1. Thermal radiation

The thermal radiation emission mechanism is related to the energy released as a result of oscillations or energy transitions of molecules, atoms and electrons in matter, which are due to the internal energy of said particles and, therefore, their temperature.

The transfer of energy by thermal radiation is faster (at the speed of light) and does not suffer attenuation due to its movement through vacuum. As with conduction and convection, energy transfer takes place from matter with higher energy (that is, higher temperature) to those with lower energy.

The propagation properties of electromagnetic waves can be applied since thermal radiation is an electromagnetic radiation. The most relevant are the frequency, v , and the wavelength, λ , which are related to each other by the following expression:

$$\lambda = c/v \quad [\mu\text{m}] \quad (1.14)$$

where c is the speed of light in the medium. In the case of propagation in a vacuum, $c = c_0 = 2.9979 \cdot 10^8 \text{ m/s}$.

All forms of matter emit radiation because they are at a temperature that is not zero. The amount of radiation emitted at each frequency depends on the internal energy and, therefore, on the temperature. A useful way to view electromagnetic radiation is as the propagation of discrete packets of energy called photons or quanta (according to Max Plank's quantum theory) with an energy of:

$$E = h \cdot v \quad [\text{J}] \quad (1.15)$$

where $h^1 = 6.6256 \cdot 10^{-34} \text{ J} \cdot \text{s}$ is Planck's constant.

1.4.2. Blackbody radiation

A blackbody is an ideal surface that absorbs all incident radiation, at all wavelengths and in all directions. Therefore, the radiation is neither reflected nor passes through the body. The absorbed radiation gradually warms up the body and this energy is re-emitted throughout its surface in a homogeneous way and at different wavelengths. As a consequence of this definition, the blackbody has three properties:

- a) It is the surface that emits the most for a given temperature and wavelength.
- b) Blackbody radiation does not depend on direction, that is, blackbody radiation is diffuse.
- c) The total radiation of the blackbody in a vacuum depends only on the temperature.

It can therefore be said that a blackbody is nothing more than anything that emits radiation when heated.

¹ The typical symbol used for Planck's constant should not be misunderstood with the thermal contact conductance, the meaning given to h in this document.

The Stefan-Boltzmann law states that the thermal radiation energy emitted by a blackbody at an absolute temperature, T , per unit time and per unit area can be expressed as follows:

$$E_b(T) = \sigma \cdot T^4 \quad [\text{W/m}^2] \quad (1.16)$$

where σ is the Stefan-Boltzmann constant $\sigma = 5.67 \cdot 10^{-8} \text{ W/(m}^2 \cdot \text{K}^4)$ and the subscript b refers to blackbody. This law is nothing more than the integration of the Planck distribution along all the wavelengths of the frequency spectrum that appears in the following expression:

$$E_b(T) = \int_0^{\infty} E_{b,\lambda}(\lambda, T) \cdot d\lambda = \sigma \cdot T^4 \quad [\text{W/m}^2] \quad (1.17)$$

The Stefan-Boltzmann law, and can be used to obtain the energy emitted by a blackbody in all directions and all wavelengths.

1.4.3. Radiative properties

Most of the materials are, in practice, opaque to thermal radiation, so it is considered a surface phenomenon and its characteristics will depend on the properties that this material has on its surface. However, other materials such as glass or water allow thermal radiation to penetrate inside or even pass through them, so the entire volume of the material interacts with this thermal radiation and cannot be considered a surface phenomenon. Therefore, the concepts of emissivity, absorptivity, reflectivity, and transmissivity are defined below.

As previously defined, a blackbody is a perfect emitter and absorber of energy, which means that no real body can emit more energy at a certain temperature. The blackbody will therefore be used as a reference to describe the radiative properties of materials. The radiative properties of a surface are determined by comparing the intensity of radiation (emitted or incident) from that surface with that of the blackbody.

The incident radiation intensity, $I_{\lambda,i}$, is the speed at which the radiation energy, $d\dot{Q}_i$, hits or is emitted by a surface with a certain direction (characterized by θ and ψ , as it can be seen in the Figure 1.10), at a given wavelength, λ , on a unit of receiving surface area normal to this direction.

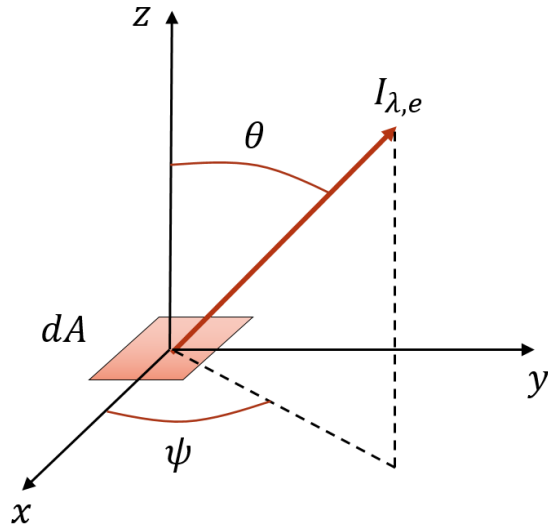


Figure 1.10: Intensity of radiation emitted from a differential area, dA . (adapted from page 76 of [1]).

Emissivity

The emissivity, ε , of the surface of a material is its effectiveness in emitting energy as thermal radiation and is the ratio between the intensity of radiation emitted by the surface at a given temperature, $I_{\lambda,e}$, and the intensity of radiation emitted by a blackbody at the same temperature, $I_{b\lambda,e}$. Its value varies between 0 and 1 ($0 < \varepsilon < 1$).

$$\varepsilon_{\lambda,\theta}(\lambda, \theta, \Phi, T) = \frac{I_{\lambda,e}(\lambda, \theta, \psi, T)}{I_{b\lambda,e}(\lambda, T)} \quad [-] \quad (1.18)$$

where λ is the wavelength, T the temperature of the body and θ and ψ are used to designate the directional behaviour of this property. If the radiation is diffuse, it is emitted equally in all directions of space, so it is true that $\varepsilon_{\lambda,\theta}(\lambda, \theta, \psi, T) = \varepsilon_{\lambda}(T)$

Absorptivity, reflectivity and transmissivity

The second group of radiant properties is related to the thermal radiation that hits on the surface of a material. A surface irradiated by thermal radiation from other surfaces that will be partially reflected, partially absorbed, and partially transmitted, depending on the surface properties of the material, as it can be seen in the Figure 1.11. Based on this fact, the following three radiative properties are defined:

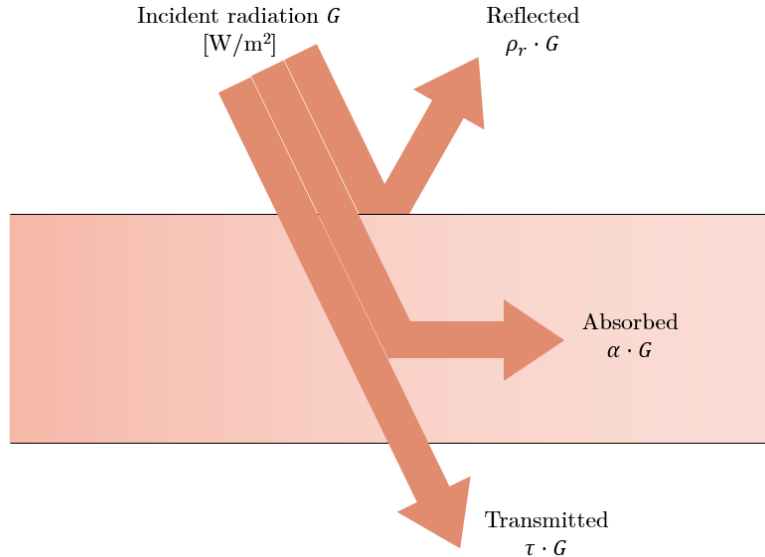


Figure 1.11: The absorption, reflection, and transmission of incident thermal radiation by a semi-transparent material (adapted from page 582 of [3]).

- **Absorptivity**

Spectral directional absorbance is defined as the fraction of incident thermal radiation, $I_{\lambda,i}$, which is absorbed for a given direction and wavelength, $I_{\lambda,i,abs}$.

$$\alpha(\lambda, \theta, \Phi, T) = \frac{I_{\lambda,i,abs}(\lambda, \theta, \psi, T)}{I_{\lambda,i}(\lambda, \theta, \psi)} \quad [-] \quad (1.19)$$

- **Reflectance**²

Spectral directional reflectance is defined as the fraction of incident thermal radiation, $I_{\lambda,i}$, which is reflected for a given direction and wavelength, $I_{\lambda,i,ref}$.

$$\rho_r(\lambda, \theta, \Phi, T) = \frac{I_{\lambda,i,ref}(\lambda, \theta, \psi, T)}{I_{\lambda,i}(\lambda, \theta, \psi)} \quad [-] \quad (1.20)$$

- **Transmittance**

Spectral directional transmittance is defined as the fraction of incident thermal radiation, $I_{\lambda,i}$, which is transmitted for a given direction and wavelength, $I_{\lambda,i,tr}$.

$$\tau(\lambda, \theta, \Phi, T) = \frac{I_{\lambda,i,tr}(\lambda, \theta, \psi, T)}{I_{\lambda,i}(\lambda, \theta, \psi)} \quad [-] \quad (1.21)$$

² Although reflectivity is generally referred to as ρ , the subscript r has been added to the symbol, ρ_r , to differentiate it from density, which is what ρ means in this document.

The previously defined coefficients verify the relationship $\alpha + \rho_r + \tau = 1$, both globally and for a given wavelength or direction. For opaque surfaces, the transmittance is zero ($\tau = 0$). Thus, in this case $\alpha + \rho_r = 1$.

1.4.4. Kirchhoff's Law

Kirchhoff's law defines that $\alpha(\lambda, \theta, \psi, T) = \varepsilon(\lambda, \theta, \psi, T)$, which means that the total emissivity of a surface of area A_s , at a temperature T is equal to the total absorptivity for radiation coming from a blackbody at the same temperature, for each direction and wavelength.

$$\begin{aligned} G_{abs} &= \alpha \cdot G = \alpha \cdot \sigma \cdot T^4 \\ E_{emit} &= \varepsilon \cdot \sigma \cdot T^4 \\ A_s \cdot \alpha \cdot \sigma \cdot T^4 &= A_s \cdot \varepsilon \cdot \sigma \cdot T^4 \end{aligned} \tag{1.22}$$

If the surface is diffuse, then from Kirchhoff's law it can be derived that $\alpha(\lambda, T) = \varepsilon(\lambda, T)$. From this point on, it will be considered that the studied surfaces are diffuse.

1.4.5. Greybody

A surface is defined as grey when its properties are independent of the wavelength considered, so in that case it can be considered from Kirchhoff's law that $\alpha(T) = \varepsilon(T)$.

Although most of the real surfaces are not exactly grey, in practice they will be considered that they are, since the equations are still valid taking into account this assumption, as long as the properties do not change with the wavelength in the range of interest. Therefore, for a given temperature it can be said that $\alpha = \varepsilon$.

1.4.6. View factor

The view factor, F_{ij} , between two surfaces i and j is defined as the part of the radiation that leaves the surface i that reaches the surface j . Mathematically, the view factor between two infinitesimal diffuse surfaces dA_i and dA_j , with uniform radiation intensity, can be expressed as:

$$dF_{ij} = \frac{\cos\theta_i \cdot \cos\theta_j}{\pi \cdot r^2} \cdot dA_j \quad [-] \tag{1.23}$$

where r is the distance between both surfaces, and θ_i and θ_j are the angles between the normal vector to each of them and its line of view, as it can be seen in the Figure 1.12.

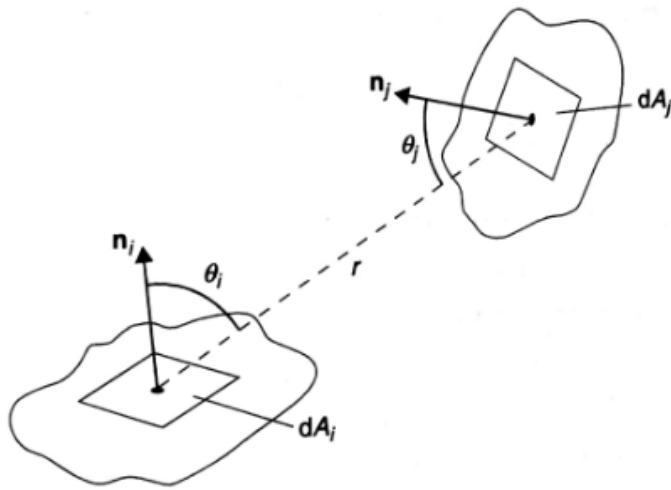


Figure 1.12: View factor between two infinitesimal diffuse surfaces (from page 83 of [1]).

Since the considered surfaces are diffuse, finite and have a radiation intensity, the view factor can be defined as:

$$F_{ij} = \frac{1}{A_i} \cdot \int_{A_i} \int_{A_j} \frac{\cos \theta_i \cdot \cos \theta_j}{\pi \cdot r^2} \cdot dA_i \cdot dA_j \quad [-] \quad (1.24)$$

By exchanging the subscripts i and j , a very useful reciprocity relationship can be obtained to determine a factor of view when its reciprocal is known, and which is the following:

$$A_i \cdot F_{ij} = A_j \cdot F_{ji} \quad [-] \quad (1.25)$$

Another of the most interesting properties regarding view factors is the fact that the sum of the view factors of a set of n surfaces forming an enclosure is equal to 1, that is:

$$\sum_{j=1}^n F_{ij} = 1 \quad [-] \quad (1.26)$$

It must be taken into account that the term F_{ii} may exist, which is the factor of view of a surface with respect to itself, because if the surface is concave it can see itself and this term will be different from zero.

1.4.7. Radiative exchange between two surfaces

Once all the parameters that affect the heat exchange by radiation have been defined, the heat exchange of a body with its environment will depend on the flows that exist between the different surfaces of the body with its environment (which can be elements external to the body, others surfaces of the body or even a surface with itself, depending on the geometry of the body). Considering two surfaces i and j , the radiative exchange between them can be defined as:

$$\dot{Q}_{ij} = \varepsilon_i \cdot \varepsilon_j \cdot \sigma \cdot F_{ij} \cdot A_i \cdot (T_j^4 - T_i^4) \quad [\text{W}] \quad (1.27)$$

where \dot{Q}_{ij} is the heat flow between the surfaces, ε_i and ε_j the emissivity of each surface, F_{ij} the view factor that surface i has of surface j , A_i the area of surface i , σ the Stefan-Boltzmann constant, and T_i and T_j the temperature of each surface. In the case that the surfaces can be considered as blackbodies, Equation (1.27) can be expressed as:

$$\dot{Q}_{ij} = \sigma \cdot F_{ij} \cdot A_i \cdot (T_j^4 - T_i^4) \quad [\text{W}] \quad (1.28)$$

In this way, by introducing the appropriate view factor in each case, the radiative exchange that will exist between two surfaces can be calculated.

1.5. Spatial environment

As previously mentioned, solar radiation, both direct and reflected by the planet it orbits, is the main source of external heat for spacecraft, but in low earth orbits (LEO), the infrared radiation that comes from the planet must also be taken into account.

However, in this project the air temperature must also be considered as a source/sink of heat, since all the operation will be carried out within the atmosphere. Each of these contributions is depicted deeply below, with the exception of the atmospheric environment, which will be deepened later (see Chapter 3).

1.5.1. Solar radiation

The Sun is the main source of heat and energy for a body close enough to the Sun. The spectral distribution of solar radiation is approximately that of a blackbody at 5778 K [4], therefore its effects are primarily perceived as short-wave radiation, as it can be seen in the Figure 1.13, where AM0 (Air Mass 0) is the radiation level outside of the Earth's atmosphere and AM1.5 is the radiation level after passing through the atmosphere 1.5 times, about the level at solar zenith angle 48.19°, an average level at the Earth's surface.

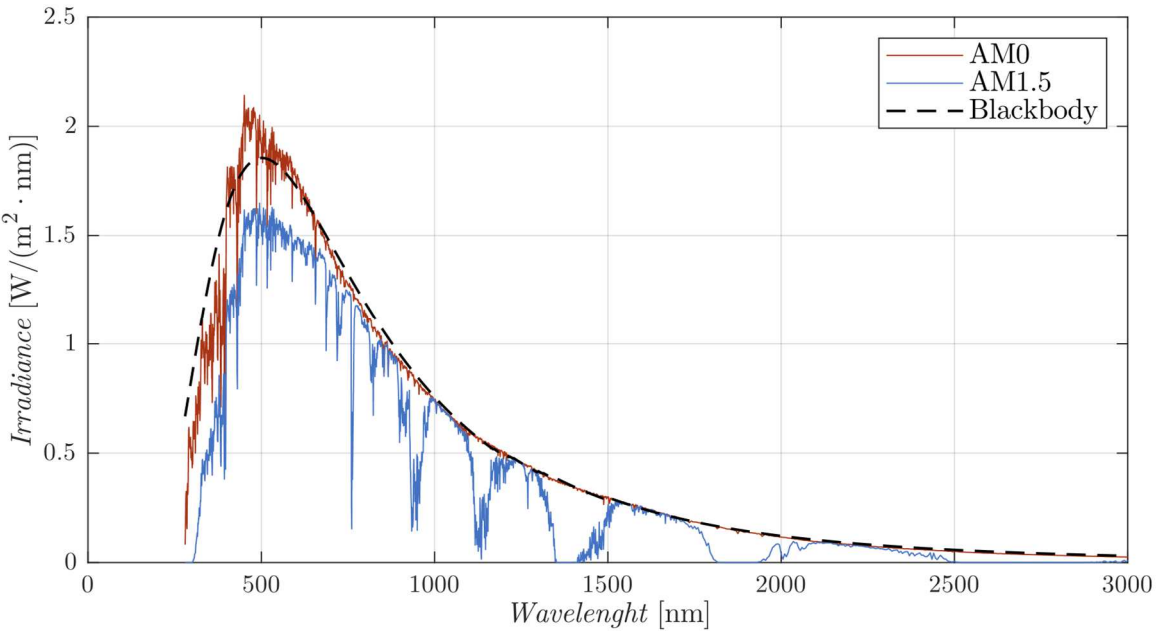


Figure 1.13: Solar spectral irradiance (adapted from page 135 of [4]).

Solar irradiance is the magnitude used to describe the incident solar energy on a surface normal to the Sun's rays. At the edge outside the atmosphere, when the Earth is at its average distance from the Sun, this magnitude is called the solar constant and its value is $G_{S,mean} = 1361 \text{ W/m}^2$ [4].

The value of this solar constant is not actually constant. Depending on the average number of sunspots, which varies with an 11-year solar cycle, the energy emitted by the Sun varies following a cycle with the same period. Also, the eccentricity and inclination of the Earth's orbit causes a variation in the energy received from the Sun between that received at aphelion, when it has a value of $G_{S,ap} = 1316 \text{ W/m}^2$ [4], and at perihelion, when it has a value of $G_{S,per} = 1407 \text{ W/m}^2$ [4].

This means that, although the assumption that the Sun is equivalent to a blackbody at 5778 K allows a very close calculation of the radiation coming from the Sun, a more detailed study makes necessary to consider these variations.

The calculation with a simple analytical expression of the solar radiation absorbed by a flat surface of area A , whose normal vector forms an angle θ with the solar rays is:

$$\dot{Q}_{sun} = \alpha \cdot G_s \cdot A \cdot \cos\theta \quad [\text{W}] \quad (1.29)$$

where α is the solar absorptance of the surface and G_s the solar constant.

1.5.2. Albedo

Albedo is the part of solar radiation incident on a planet that is reflected or scattered across the planet's surface and atmosphere, if it exists. The albedo coefficient, a , is defined as the fraction of incident solar radiation that is reflected by the planets.

Determining this value is a complex task, since the surface of the Earth is very irregular. The oceans absorb most of the incident radiation, while ice or snow reflects most of the solar radiation. The mean value for Earth is taken as 0.3 [4]. For simplified analytical estimates, the albedo energy absorbed by a surface of area A can be calculated as follows:

$$\dot{Q}_{alb} = a \cdot G_s \cdot A \cdot F_{SC-P} \cdot \cos\varphi \quad [\text{W}] \quad (1.30)$$

for $-\pi/2 \leq \varphi \leq -\pi/2$, where a is the planetary albedo coefficient, G_s the solar constant, φ the solar zenith angle and F_{SC-P} the factor of view between the surface and the planet. The angle φ takes into account the fact that the albedo is at its maximum at the subsolar point and becomes zero when the planet seen by the space system is in eclipse. In the case of Earth orbits, albedo charges are relevant only for low Earth orbits. For telecommunications satellites in geostationary orbits (GEO), these loads are practically negligible

1.5.3. Planetary infrared radiation

Planetary radiation is diffuse radiation within the infrared part of the spectrum, emitted by a planet due to the fact that it is at a temperature that is not zero, and is a combination of radiation emitted by the planet's surface and by atmospheric gases. As with the albedo coefficient, the radiation emission from the surface of a planet is not uniform and varies depending on the presence of, for example, oceans, populated areas or desert.

The radiative properties of a planet can be calculated from the energy balance equation, since although they are not at a constant temperature, the solar energy absorbed by the planet is almost balanced with the radiation emitted.

From the blackbody temperature of the planet T_P , that for Earth has a mean value of 288 K [4], the planetary infrared heat load on a surface of area A can be calculated as follows:

$$\dot{Q}_{planet} = \varepsilon \cdot A \cdot F_{SC-P} \cdot \sigma \cdot T_P^4 \quad [W] \quad (1.31)$$

where ε is the infrared emissivity of the surface, σ the Stefan-Boltzmann constant and F_{SC-P} is the view factor between the surface of the space system and the planet.

As in the case with albedo charges, infrared planetary radiation is relevant for low altitude orbits, while its influence on satellites in geostationary orbits is negligible.

1.5.4. Re-radiation to Space

Since outer space is at a temperature that is lower than that of spacecraft, there will be a re-radiation flow into space. This flow goes from the spacecraft to the space that surrounds it. For a surface of area A this flow can be calculated as:

$$\dot{Q}_{space} = -\varepsilon \cdot A \cdot \sigma \cdot (T^4 - T_{Space}^4) \quad [W] \quad (1.32)$$

where ε is the infrared emissivity of the surface, σ the Stefan-Boltzmann constant, T the temperature of the surface and T_{Space} the space sink temperature, which has a value of 3 K [4].

1.6. ESATAN-TMS software

The ESATAN Thermal Modelling Suite (ESATAN-TMS), which development was undertaken by ITP Engines UK Ltd. under an European Space Agency (ESA) contract, is a software that allows a complete thermal analysis that allows the prediction of the distribution of temperatures in components and systems in the engineering field, especially those related to space systems.

ESATAN perform thermal analysis by the thermal network technique, that is, it accepts models of components or systems presented to it in thermal network terms along with the instructions that are necessary to find the solution.

The function of ESATAN is to solve problems that the user introduces, for example, using the program's graphical interface (ESATAN-TMS Workbench), that is shown in Figure 1.14. In this way, the user is able to visually specify the model and obtain the temperature distribution that will be obtained in both steady-state or transient solutions.

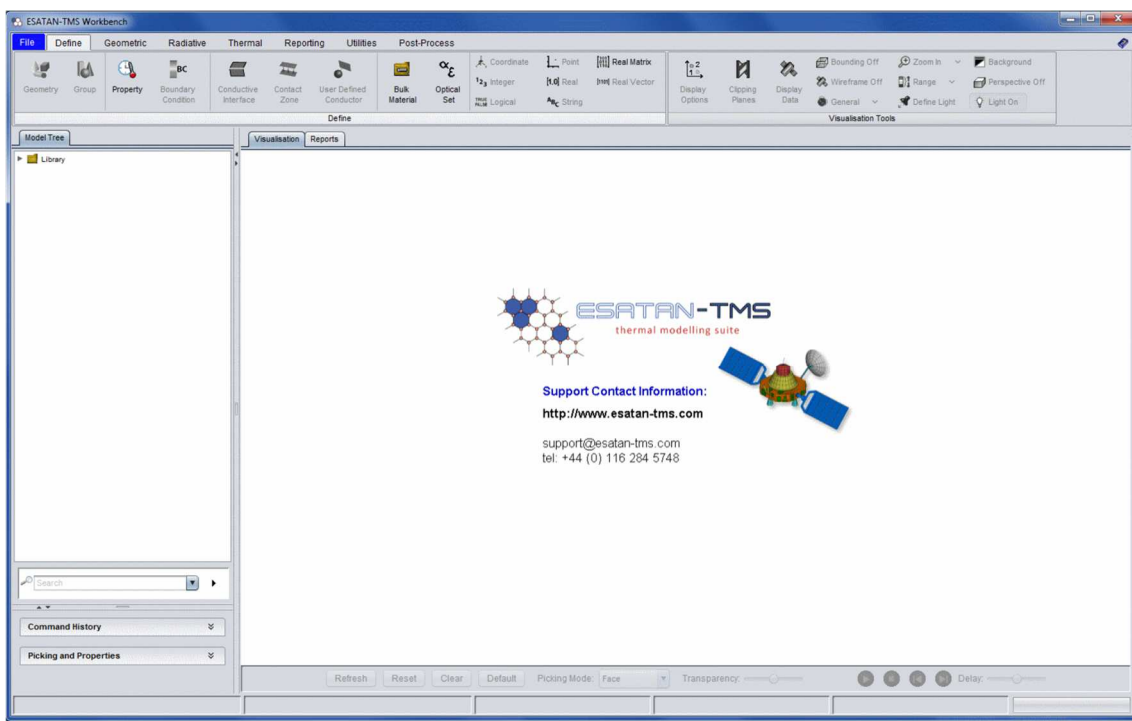


Figure 1.14: ESATAN-TMS workbench window aspect (from ESATAN-TMS workbench user manual).

To find these solutions the lumped system analysis is used. The lumped parameter method is a mathematically way of deriving a first-order finite-difference approximation to obtain a differential equation with which to work more easily.

For this, the temperature of the nodes is considered uniform and is only a function of time. In this way, each node will have an associated temperature and a series of input and output heat flows.

These relations between nodes that allow to calculate the flows are called GLs in the case of linear conductors, which come from those nodes that are in contact with the node considered or that have been manually specified, and the radiative flows, or GRs in the case of radiative conductors, which are calculated taking into account the view factors and the thermo-optic properties of each node with the rest of the model nodes.

By solving the system of equations that is formed, it is possible to obtain the temperature of each node after a time differential has elapsed. Considering n nodes N_1, N_2, \dots, N_n , applying the energy balance to node N_i the following expression is obtained:

$$C_i \cdot \frac{dT_i}{dt} = \sum_{j \neq i} K_{ij} \cdot (T_j - T_i) + \sum_{j \neq i} R_{ij} \cdot (T_j^4 - T_i^4) + Q_i + Q_e + Q_r \quad (1.33)$$

where C_i is the heat capacity, T_i its temperature, Q_i the internal heat source of the node N_i , Q_e the external heat sources (albedo, solar and earth) and Q_r the rest of heat sources. The temperature of the node N_j is T_j . The linear conductance or linear exchange constant, between nodes N_i and N_j is K_{ij} and the radiative exchange constant is R_{ij} . For the steady-state case this expression is:

$$0 = \sum_{j \neq i} K_{ij} \cdot (T_j - T_i) + \sum_{j \neq i} R_{ij} \cdot (T_j^4 - T_i^4) + Q_i + Q_e + Q_r \quad (1.34)$$

1.7. References of this chapter

- [1] J. Meseguer, I. Pérez-Grande, A. Sanz-Andrés - *Spacecraft thermal control* - 1st ed. 2012.
- [2] Frank P. Incropera [et al.] - *Fundamentals of heat and mass transfer* - 6th ed. 2007.
- [3] Yunus A. Cengel - *Heat transfer: A practical approach* - 2nd ed. 2002.
- [4] European Space Agency - *ECSS-E-ST-10-04C Rev.1, Space environment* - 15 June 2020.

(Page intentionally left blank).

Chapter 2.

Mission description

2.1. Introduction

The number of stratospheric balloon missions has increased significantly in recent years due to the advantages that these types of experiments provide. One of these advantages is the fact that it is a cheaper alternative to use a launch vehicle to reach low Earth orbit, which allows entities with less budget, such as universities, to carry out studies in environments very similar to those of the vacuum of the space environment.

However, these types of experiments offer more advantages, such as the fact that at high latitudes it is possible to get a vision of the Sun 24 hours a day in almost stationary conditions, which is impossible to achieve with a low orbit.

As with space systems, the study of the thermal behaviour of all the parts that compose the experiment is of great importance to ensure that it is capable of successfully carry out its mission. For this, the common approach is to assume that the behaviour of the experiment inside the balloon is similar to that which it would have in the vacuum of space, since at the height that stratospheric balloons reach, the air pressure is practically negligible. Although this approach is valid in most situations, the use of stratospheric balloons to test space instrumentation and carry out scientific experiments has made the design process of them more complex with the time.

As already mentioned, the stationary nature of the balloon's float phase, which does not exist in experiments in low orbits in which phases of solar irradiation and eclipse alternate, makes stratospheric balloon missions have a longer residence time over a certain area. This aspect must be considered when designing the thermal control, because thermal inertia of its different elements cannot be used to control its temperature.

The other big difference is related to heat exchange by convection. In the flotation phase, this heat exchange mechanism is negligible compared to the radiative and conductive. However, in certain elements, not considering their effect can lead to an improper thermal design. In addition, during the ascent, forced convection with the atmospheric air is the predominant exchange mechanism, so it may cause some of the elements to operate outside their operating temperature range, especially in the coldest layers of the atmosphere.

Therefore, to collect more data on stratospheric balloon flights to clarify some of uncertainties that exist when modelling and analysing a stratospheric balloon payload from a thermal point of view, an experiment, called TASEC-Lab, has been developed.

2.2. Stratospheric balloons

A stratospheric balloon is any type of balloon that moves through the stratosphere, that is, between 11 and 50 km in height, regardless of its volume, type or purpose.

Its operation is based on the Archimedes principle, by which a gas lighter than air (generally helium or hydrogen) exerts an upward thrust on the inside of the envelope, causing it to rise and carrying its load with it.

2.2.1. Composition

The size, elements or arrangement of the same within a stratospheric balloon will depend to a large extent on its purpose, so there is no single type, but a large number of options are available. Broadly speaking, the components of the system can be separated into two groups, on the one hand the balloon itself and on the other the flight train, where the instruments necessary for the operation of the balloon are located, among which are, the following items:

- Mechanism for payload separation.
- Recovery parachute.
- A communications system to transmit and receive commands, both for the balloon and for the instruments on board.
- Telemetry of height, pressure, temperature and position of the assembly.
- Power supply (batteries) and if necessary, solar panels.

It is also common for the tools to be mounted on a gondola, which serves as protection for the instruments during the flight and especially during the landing.

2.2.2. Types of balloons

As already mentioned, there is a wide variety of stratospheric balloons in terms of size, composition, shape, etc., but they can be functionally divided into two large groups, open or closed.

Open balloons, also called zero pressure balloons, have an opening at the bottom, so that as the gas expands during the ascent until it reaches an equilibrium with the air outside. In this way, any increase in pressure produced inside it (for example, by the heating of the internal gas by the action of the Sun), is automatically compensated by the venting of the gas.

Closed or super-pressure balloons are totally closed and hermetic elements where the internal gas cannot escape, so the increase in internal pressure (a process called super-pressurization) is supported by the reinforced envelope of the balloon, which expands until it reaches an equilibrium height.

The main difference between these two types of balloons is the duration of flight and the load they are capable of lift. Zero pressure balloons can lift a load of up to three tons in the case of the largest models, with a maximum flight duration of seven days. On the other hand, the super-pressure balloons have a much lower weight limit, but they can perform flights with a duration of several months.

Another of the main differences is the fact that balloons of the first type are capable of controlled vertical ascents and descents, which makes them ideal for conducting atmospheric surveys at different heights, while balloons of the second type have the peculiarity of staying at very stable height levels during flight, which makes them ideal for monitoring the horizontal movement of air masses at constant pressure.

2.2.3. Materials and construction

The construction of the stratospheric balloons is carried out using plastic materials such as polyethylene or mylar in the form of films whose thickness is just a few microns, so they are very light, but at the same time very resistant.

For their manufacture, these films are quoted in the form of segments that are joined with heat or with an adhesive that does not excessively increase the weight of the balloon. Also included are an element called load tapes, which help the envelope to withstand the internal pressure and mechanical pull of the payload.

2.2.4. Phases of flight

The phases of the flight of a stratospheric balloon will depend on the peculiarities of each balloon and its payload, however, the following phases can be defined common to most flights.

Launch

The objective of the launch phase is to make the balloon and the flight train rise without any element suffering any type of damage. There are numerous techniques for launching a balloon, which will depend on the characteristics of the balloon and the facilities in which it is carried out.

If the weight of the flight train is reduced, it is distributed on the ground and is taken by the balloon from there or from the hands of some people who hold it and accompany the balloon running. However, when the weight is higher, it is necessary to have some type of launch vehicle that supports the payload and moves with it until the balloon is positioned on the load and lifts it. This prevents the gondola from dragging on the ground.

Initial ascent

Once the assembly is in the air, the ascent begins, the speed of which is related to the weight of the load and the amount of gas introduced into the balloon bubble during inflation (free lift).

The most critical part of the ascent is the moment in which it is in the tropopause, (located between 5 and 10 km high). In this area of the atmosphere there are the lowest temperatures that the balloon will experience and in it there are currents that can cause the balloon envelope to break, especially in large balloons.

Once the tropopause is overcome, the balloon rises to its floating height, in which an equilibrium occurs that will be given by its weight, dimensions and amount of gas it contains. The nominal ascent phase usually lasts between two and three hours. The variation in the shape of the stratospheric balloons during the ascent phase can be seen in the Figure 2.1.

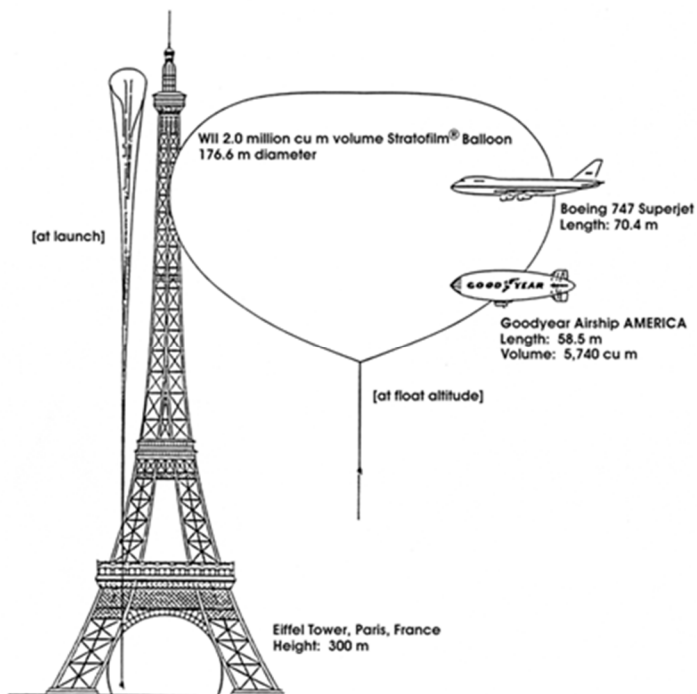


Figure 2.1: NASA balloon size comparison at launch and at float altitude (from []).

Flight phase

During the ascent, the direction of the balloon's movement varies constantly due to the existence of air currents. However, once the flight height is reached, the direction of the displacement is more or less constant and will depend on the prevailing currents at said heights of the atmosphere.

In the case of very long-lasting balloons, the gas contained inside the balloon will experience changes in its temperature due to the effect of sunlight, which will cause it to rise during the day and decrease at night. To avoid this effect, these balloons have ballast tanks that are released at night to gain height, and vent valves, which allow gas to be released from the balloon during the day to prevent an increase in height. This contractions and expansions cannot be sustained for an unlimited time and, therefore, will limit the flight time of the balloon.

Descent and recovery

Once the objectives of the completed experiments have been met, or when the float phase cannot be sustained any longer, the balloon descent phase begins.

When the balloon flies over a suitable area to perform the descent, a signal is transmitted to it and causes the separation of the balloon payload, which remains in free fall until the parachute that prevents it from crashing to the ground opens. Additionally, when the payload begins to fall, the balloon envelope is ripped by a rope attached to the payload, causing it to fall. This phase generally lasts between 30 and 45 minutes.

2.2.5. Main applications

The applications of a stratospheric balloon are very numerous, but the most interesting are those that take advantage of its main characteristics, that is, flight height, relative stability and low cost. This last characteristic makes it possible to carry out measurements and experiments in almost space conditions, but with a much shorter development time, cost and exploitation of data than in a space mission.

2.3. TASEC-Lab description

The Thermal Analysis Support and Environment Characterization Laboratory (TASEC-Lab) is an experiment designed to study the convection heat transfer, the thermal environment and the balloon dynamics during the ascent and float phases of a stratospheric balloon. It consists of an aluminium structure of 130 x 130 x 330 mm with three compartments. The lower one contains the Electrical Power Subsystems, the upper one the Heat Transfer Laboratory and in the middle the Electronics. It also carries a cup anemometer to be tested at low pressure conditions in order to provide the relative speed of the balloon-gondola system in order to characterize the dynamics and the forced convection heat transfer.

The electronics compartment contains a Raspberry Pi 3B+ that acts as an onboard computer, as well as modules compatible with it, as can be seen in Figure 2.2. In this way, it has been possible to adjust both to the reduced development time of the experiment and to limit the budget that was allocated to it, since this type of hardware has already been successfully tested in the stratospheric environment.

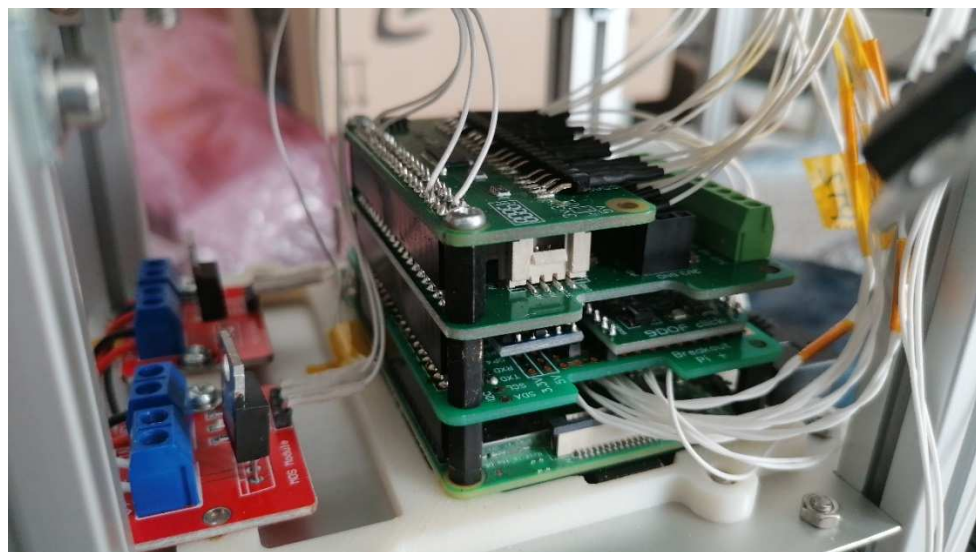


Figure 2.2: View of the electronics compartment, as well as the pressure sensors from the Environmental Lab (on the left).

The Heat Transfer Lab (HTL) is the main experiment of all the TASEC-Lab has. The HTL consists of a 25 x 50 mm flat heated plate inside the upper compartment of the structure, as already mentioned, whose dimensions are 130 x 130 x 140 mm and is totally closed, except for four slots in its upper part, which can be seen in Figure 2.3, and whose purpose is to allow the exchange of air with the environment. The temperature of the plate is controlled during all phases of flight with a power dissipation source fixed to it.

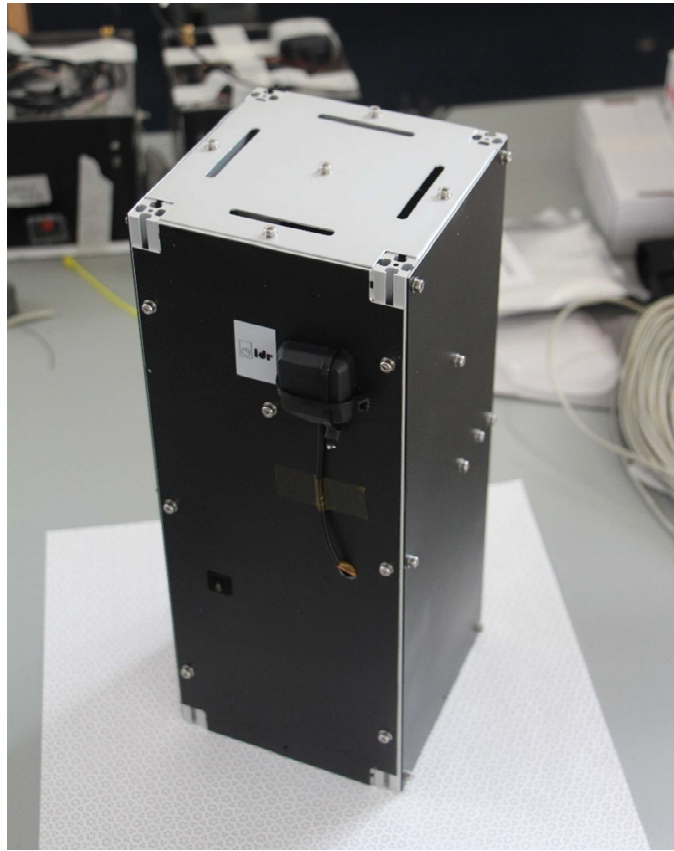


Figure 2.3: View of the upper part of the TASEC-Lab, where it can see the four slots through which the air exchange with the environment occurs.

The purpose of this experiment is to simulate a team equipment that is on board a mission embarked on a stratospheric balloon and to characterize the heat exchange by conduction that said equipment has with its environment. For this reason, radiation and conduction heat exchanges with its environment have been minimized. Inside this compartment, the temperature of both the air in various areas, as well as the closure panels or the plate itself is measured in numerous locations using PT1000 and TC74 digital thermistors.

Another of the experiments found inside the structure is the Attitude Determination Laboratory, which consists of an Inertial Measurement Unit (IMU) and a Global Positioning System (GPS). The aim of this experiment is to characterize the flight dynamics of the balloon-gondola system (inclination and orientation) as well as the positioning to be able to compare it with predictive models.

Finally, the Environmental Lab consists of a series of pressure and temperature sensors as well as a cup anemometer whose objective is to test their performance at low pressure in the stratosphere and which is the only element that is not mounted on the main structure of the TASEC- Lab, as can be seen in the Figure 2.4.



Figure 2.4: View of the gondola arm on which the anemometer is mounted.

Both the design of the gondola on which the experiment is mounted, and the flight of the balloon are carried out by the company B2Space. This gondola, which can be seen in Figure 2.5, is made up of a baseplate made of CFRP with four 350 mm aluminium struts attached to a CFRP square in the upper part, and is anchored to a Pressure Zero balloon, inside which 30 m³ of helium were injected.



Figure 2.5: View of the gondola with the two experiments integrated into the gondola.

This flight is part of the Blue Jay program, which aims to provide students with the opportunity to learn, develop their skills, fly and test their experiments in the stratospheric environment. TASEC-Lab experiment was launched together with another experiment from the Universidad Alfonso X el Sabio, from the Military Airport of León, Spain, on 16th of July 2021.

2.4. References of this chapter

- [1] StratoCat Website - *¿Qué es un globo estratosférico?* - Online, 2021.
<https://stratocat.com.ar/artics/globos0.htm>

Chapter 3.

Model description

3.1. Introduction

The previous chapter described the TASEC-Lab experiment, as well as each of its parts. The next step is to make a finite element model that is capable of adequately simulating its thermal behaviour. In order to carry out this model, different considerations must be taken into account, among which the limitations of the software used (ESATAN-TMS) stand out. In order to make the model properly, it can be divided into two parts.

On the one hand, the **geometric model**, which is the model created in ESATAN, where the different **geometries** that make up the model are represented, as well as their **properties** such as **materials**, **thickness**, **optical finishes**, etc. Figure 3.1 shows the general appearance of the geometric model of the TASEC-Lab.

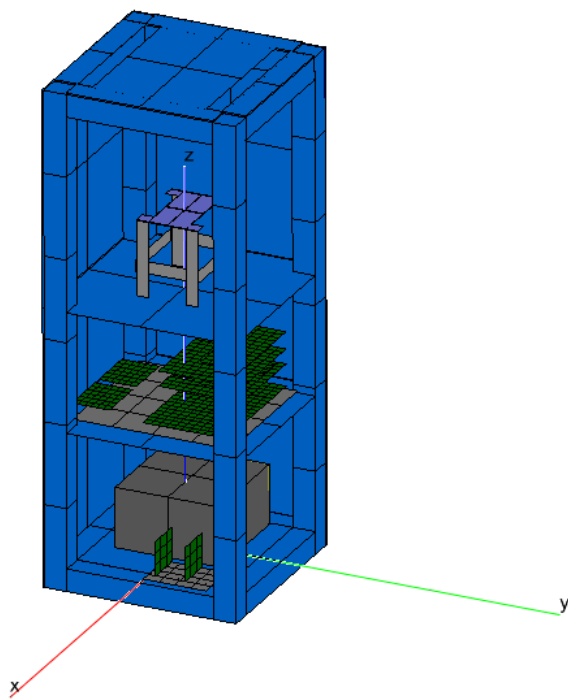


Figure 3.1: Aspect of the interior of the model of the experiment carried out in ESATAN.

On the other hand, the **mathematical model** is defined. This model **contains both the modelling of the air nodes** that has been carried out and the relationship of said nodes with the rest of the model, that is, with the geometric model. This part of the model also includes the **modelling of the thermal environment** during the ascent of the experiment.

3.2. Geometrical model

3.2.1. Used materials and optical sets

To make the model in ESATAN, a series of materials have been used, the properties of which are described below. Six isotropic materials have been used (Aluminium, Delrin, Foam, the material used in PCBs, the one used in the battery and the one used in the heater) and one anisotropic (CFRP). Its properties can be seen in the Table 3.1 and its distribution in the model in the Figure 3.2.

Table 3.1: Properties of the materials used in the model.

Material	ESATAN label	Density (kg/m ³)	Specific Heat (J/kg · K)	Conductivity (W/ m · K)
Aluminium	Alum_Mat	2700	860	168
Delrin	Delrin_Mat	1430	1300	0.43
Heater	Heater_Mat	0.43	1300	1430
PCB	PCB_Mat	2223	589	10
CFRP	CFRP_Mat	1500	840	30 (parallel) 1,25 (perpendicular)

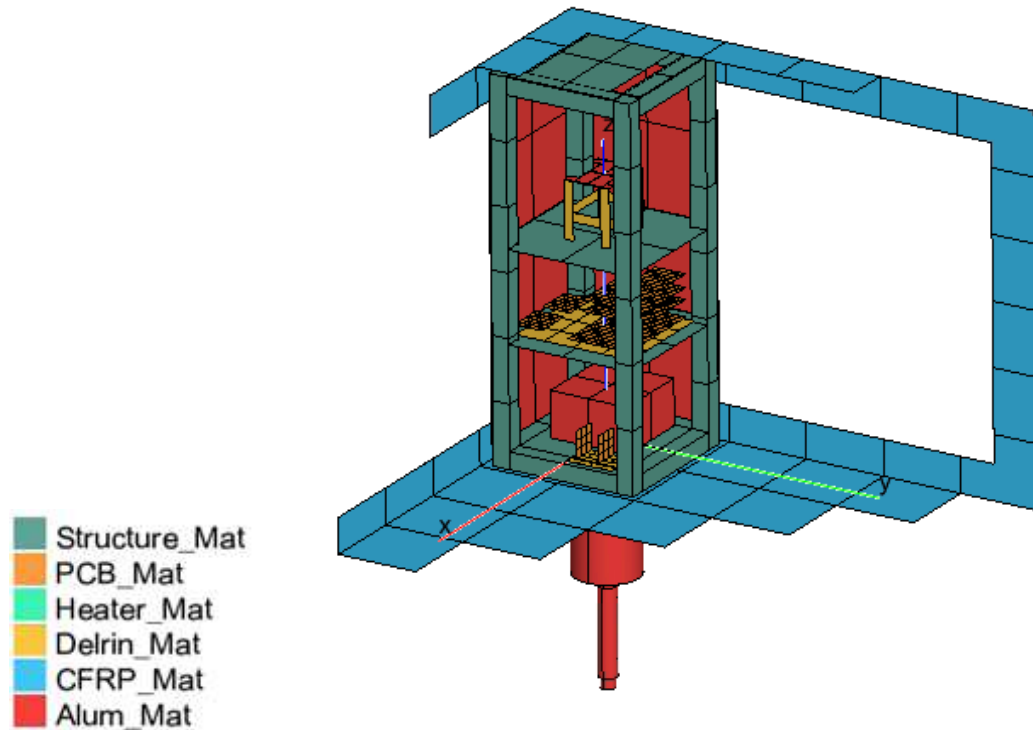


Figure 3.2: Distribution of the different materials in the model.

In the Figure 3.2 legend there is a material called **Structure_Mat** not previously defined. This is because **this material is aluminium**, but it was given a **different name** to be able to make changes in its properties without modifying the rest of the aluminium elements. The **same consideration** has been taken with the thermo-optic properties.

These materials must also have a series of thermo-optic properties that characterize the radiative heat exchange that said surface will have with its environment. The properties of the different optical sets used in the model can be seen in the Table 3.2 and its distribution in the model in the Figure 3.3.

Table 3.2: Optical sets of the materials used in the model.

Optical Set	ESATAN label	Infrared emissivity	Solar absorptivity
Aluminium	Alum_OS	0.6	0.4
Aluminized tape	Plate_OS	0.1	0.03
Black Paint	Black_Paint_OS	0.8	0.96
Black SLI	SLI_Black_OS	0.88	0.92
CFRP	CFRP_OS	0.5	0.5
Delrin	Delrin_OS	0.87	0.96
PCB	PCB_OS	0.8	-

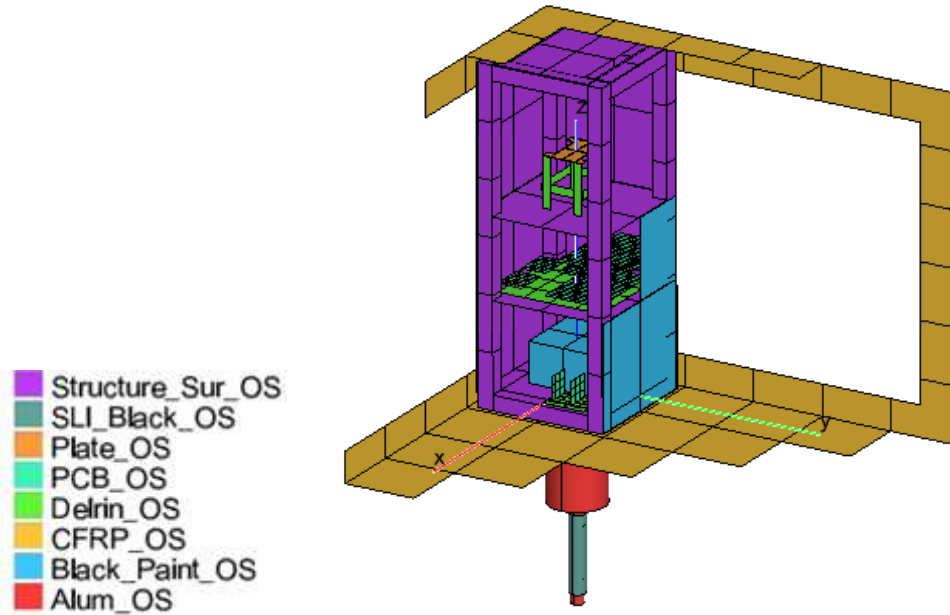


Figure 3.3: Distribution of the different optical sets in the model.

These properties have been obtained from [1] and from [2], as well as data provided by other related works. The methodology that has been followed to establish the properties of the material used in PCBs is detailed in the Annex A.

3.2.2. Geometrical model components

The model has been made in ESATAN looking for the greatest similarity with the real model, both in the materials used and in their interfaces. Next, the model is described part by part, specifying the materials used in them, thermo-optical properties and thermal couplings with other elements.

Frames

The structure of the satellite is formed of frames, all of them with the same shape. The frames used have a 15x15 mm square base, but they are not solid prisms. The geometry of these profiles, shown in Figure 3.4, is too complex to be represented in ESATAN, so simplifications must be made. However, its dimensions mean that its volume cannot be ignored, since there may be radiative heat exchange with the other elements of the satellite.



Figure 3.4: Picture of the frames [3].

The frames have been represented in ESATAN, as can be seen in Figure 3.5, as hollow prisms in which the thickness of the walls has been adjusted in such way that the total mass of said prism per unit length is the same as the real frames. In this way, the nodes have the same heat capacity that they would have if the geometry had been represented exactly, and the behaviour of this part of the structure is simulated with more precision.

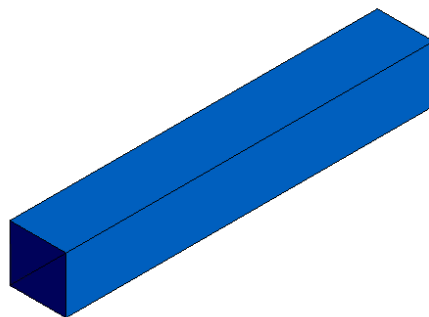


Figure 3.5: Representation of the frames in ESATAN.

Although the frames that have been represented in ESATAN have four faces, they all represent a single node. Both the material and the thermo-optical properties used in the frames are shown in the Table 3.3 and its thermal couplings in the Table 3.4.

Table 3.3: Model details for frames.

Part	Material	Optical Set
Frames	Aluminium	Aluminium

Table 3.4: Thermal couplings for frames.

Part 1	Part 2	Contact conductance, h [W/(m ² · K)]	GLs
Frame i	Frame j	300	-
Frame i	Frame j	-	0.1 (for each screw)

Trays

Inside the satellite there are three trays that will define the three cavities where the different elements of the satellite will be arranged (Battery, electronics and the Heat Transfer Lab), as can be seen in the Figure 3.6, a representation of the structure of the satellite in ESATAN.

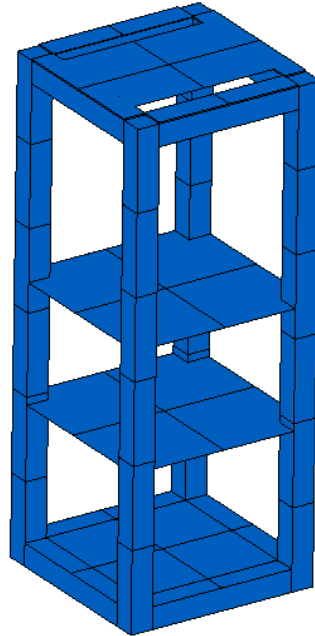


Figure 3.6: ESATAN representation of the structure with the trays.

The simplicity in the geometry of this element makes it possible to represent it exactly in ESATAN as a flat plate with the corresponding dimensions and thickness. These trays have been simulated with four nodes.

The upper closure panel could be added to this group, as it has the same geometry as the trays. However, this closure panel has slots that must be simulated, because although it is not likely, sunlight can hit the experiment plate through these slots.

The trays have been designated A, B, C and D, being Tray A the one located and the lower position, B the one in the immediately higher position, etc. Both the material and the thermo-optical properties used in the frames are shown in the Table 3.5 and its thermal couplings in the Table 3.6.

Table 3.5: Model details for trays.

Part	Material	Optical Set
Trays	Aluminium	Aluminium

Tray A has been attached to the structure by mounting four Delrin washers in the middle of each of its sides to thermally isolate the battery, so there is no direct contact between the tray and the frames.

Table 3.6: Thermal couplings for trays.

Part 1	Part 2	Contact conductance, h [W/(m ² · K)]	GLs
Tray A	Frames	0	-
Tray B	Frames	300	-
Tray C	Frames	300	-
Tray D	Frames	300	-
Tray A	Frames	-	0.00262 (for each washer)
Tray i	Frames	-	0.1 (for each screw)

Closure panels

For the closure panels, the same methodology has been followed as for the trays, as well as the material used. However, in this case the area of the panel that closes each of the cavities has been separated into different surfaces, so that its surface thermo-optical properties can be modified independently.

These properties have been defined by default equal to those of aluminium on the inner surface and black paint on the outer surface, as it can be seen in the Table 3.7.

Table 3.7: Model details for the closure panels.

Part	Material	Optical Set
Closure panel	Aluminium	Aluminium (inside) Black paint (outside)

The methodology followed to define the thermal couplings of the panels with the rest of the structure is analogous to that carried out with the trays, as can be seen in the Table 3.8.

Table 3.8: Thermal couplings for the closure panels.

Part 1	Part 2	Contact conductance, h [W/(m ² · K)]	GLs
Closure panel	Frames	300	-
Closure panel	Frames	-	0.1 (for each screw)

Battery

The battery, whose CAD representation can be seen in the Figure 3.7, is a model that simply consists of a prism of the same dimensions as the battery on which the previously defined battery material has been applied and whose outer surface has black paint, as it can be seen in the Table 3.9. The surface finish of its inner surface has not been specified, as this surface has been defined as conductive only.

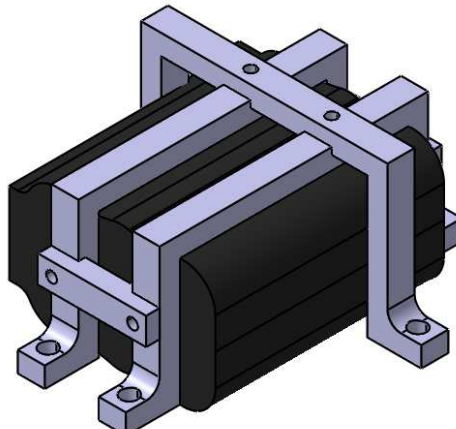


Figure 3.7: Battery representation with its Delrin support.

To isolate the battery from the gondola and prevent it from cooling down, a black SLI has been placed in the lower part of the structure, covering the lower part of tray A.

Table 3.9: Model details for the battery.

Part	Material	Optical Set
Battery	Aluminium	Black paint (outside)
SLI	Aluminium	Black SLI

The battery is only attached to tray A using four screws, so its base is in contact with this tray in addition to the GLs corresponding to the screws, as it can be seen in the Table 3.10.

Table 3.10: Thermal couplings for the battery.

Part 1	Part 2	Contact conductance, h [W/(m ² · K)]	GLs
Battery	Tray A	300	-
Battery	Tray A	-	0.1 (for each screw)

Printed Circuit Boards (PCBs)

Printed circuit boards or **PCBs** have been mounted on a Delrin base that insulates them thermally from the rest of the structure, as these are one of the elements that generates the most heat during operation. Their arrangement can be seen in Figure 3.8.

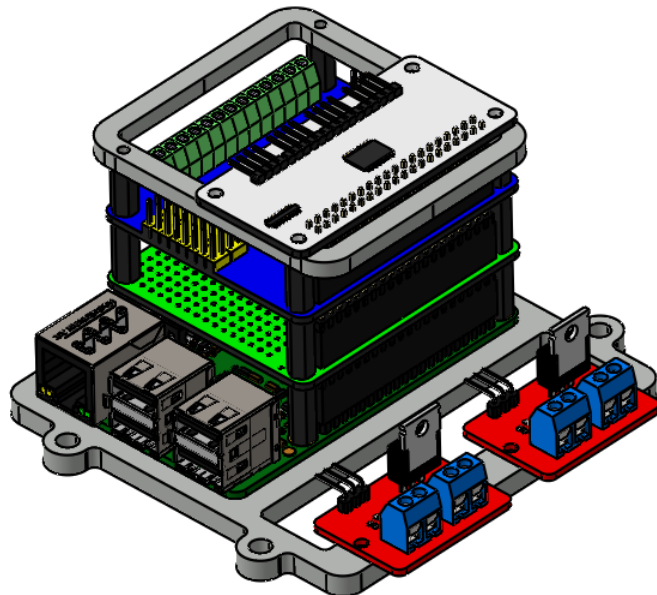


Figure 3.8: PCBs representation over the Delrin base.

The material used in the PCBs and their optical finish appear in the Table 3.11.

Table 3.11: Model details for the PCBs.

Part	Material	Optical Set
PCBs	PCB	PCB

The thermal coupling between the PCBs that are in contact with the Delrin base has been simulated assuming that the value of the contact conductance is not the same as that of said base with the tray B on which they are mounted, as it can be seen in the Table 3.12.

Table 3.12: Thermal couplings for the PCBs.

Part 1	Part 2	Contact conductance, h [W/(m ² · K)]	GLs
PCB	Delrin Base	300	-
Delrin Base	Tray B	100	-
PCB	PCB		0.1 (for each screw)
PCB	Tray B	-	0.1 (for each screw)

To simulate the converters, which can be seen in the Figure 3.9, which are housed in the battery cavity, the same methodology has been followed as for the other PCBs.

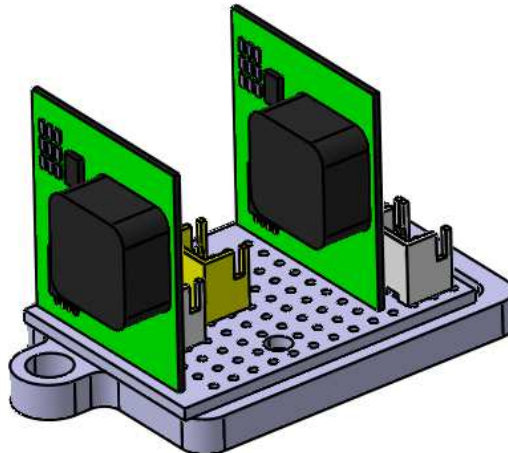


Figure 3.9: Converters representation.

Finally, the GLS that simulate the cables that exist between the Battery, converters and PCBs and between PCBs and the heater of the HTL board have also been calculated.

Heat Transfer Lab

Within the Heat Transfer Lab, not only the plate that forms the experiment should be included, but also the cavity in which it is located. However, since these elements are already defined, it is only necessary to describe the plate and its support. In the Figure 3.10 it can be seen the CAD representation of this element and in the Figure 3.11 its representation in ESATAN:

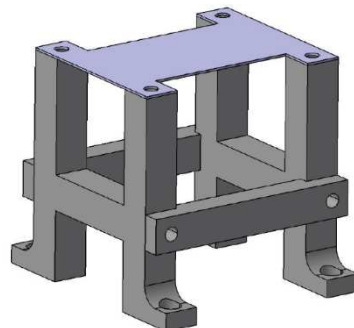


Figure 3.10: CAD representation of the plate and its support.

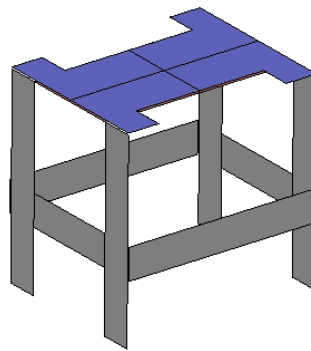


Figure 3.11: ESATAN representation of the plate and its support.

The plate that will be used to characterize the convection has dimensions of 25 x 50 mm, with a thickness of 0.5 mm. This plate is made of aluminium. However, its thermo-optical properties have been modified with aluminized adhesive tape.

On the lower side of the plate a heater that will communicate the necessary power to vary its temperature depending on the ambient air conditions and the temperature of the plate itself. This heater has also been covered with the aluminized tape previously described.

The plate holder is manufactured from Delrin to minimize the conductive heat exchange of the plate with the tray on which it is mounted. The materials used and their thermo-optical properties are shown in the Table 3.13.

Table 3.13: Model details for the HTL.

Part	Material	Optical Set
Plate	Aluminium	Aluminized tape
Heater	Heater	Aluminized tape
Delrin	Delrin	Delrin

The plate is attached to the Delrin supports with an experimentally calculated GL [4]. This value and that of the rest of the contact zones appear in the Table 3.14.

Table 3.14: Thermal couplings for the HTL.

Part 1	Part 2	Contact conductance, h [W/(m ² · K)]	GLs
Plate	Heater	10000	-
Delrin support	Tray B	300	-
Plate	Delrin support	-	0.00008325 (for each contact zone)

Cup anemometer

The cup anemometer, that during the development of the model was located in the lower part of the gondola, is made up of two concentric cylinders, the rotor and the stator, as well as the cups that will make it rotate. these cups have not been represented in ESATAN as they have little thermal influence on the rest of the model. The appearance of the anemometer can be seen in Figure 3.12.



Figure 3.12: CAD representation of the anemometer.

A heater has been placed on the rotor to prevent this element from cooling below the range for which it has been calibrated, as it can be seen in the Figure 3.13. The whole set has been covered with a black SLI. The properties of these elements are shown in Table 3.15.

Table 3.15: Model details for the anemometer.

Part	Material	Optical Set
Anemometer	Aluminium	Aluminium
Heater	Heater	Heater
SLI	Aluminium	Black SLI

Since it has been assumed that the SLI is not in contact with any element of the anemometer, the only thermal coupling that exists is that of the heater with the anemometer, as specified in Table 3.16

Table 3.16: Thermal couplings for the anemometer.

Part 1	Part 2	Contact conductance, h [W/(m ² · K)]	GLs
Anemometer	Heater	10000	-



Figure 3.13: Anemometer with the heater attached.

Gondola

The main problem encountered when making a model of the gondola is the lack of information about it, both in terms of dimensions and materials.

Through the observation of infographics, photographs, etc. of the B2Space program, the approximate size it has as well as the material with which it is built has been estimated. This material is a Carbon Fibre Reinforced Polymer (CFRP) whose properties are those previously defined. These properties, shown in the Table 3.17, are typical values, since there is no more information to characterize it.

Table 3.17: Model details for the Gondola.

Part	Material	Optical Set
Gondola	CFRP	CFRP

The CubeSat is attached to the gondola taking advantage of the screws used to simulate the closure of the panels, in the position that can be seen in the Figure 3.14, so it will be in contact with the gondola on both sides and the base, with the thermal properties that appear in the Table 3.18.

Table 3.18: Thermal couplings for the Gondola and the rest of the elements.

Part 1	Part 2	Contact conductance, h [$W/(m^2 \cdot K)$]	GLs
TASEC-Lab	Gondola	300	-
Anemometer	Gondola	300	-
TASEC-Lab	Gondola	-	0.1 (for each screw)

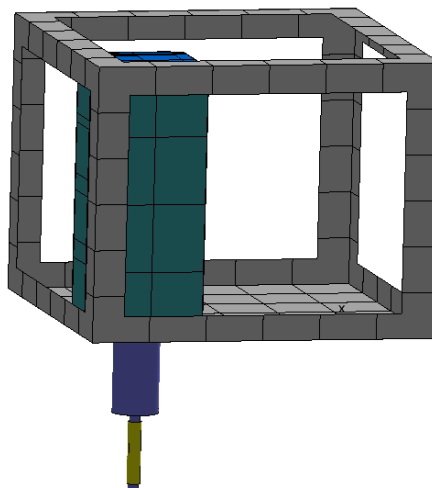


Figure 3.14: Position of the TASEC-Lab and the cup anemometer on the gondola.

3.2.3. Power dissipation

Once the model is defined, the value of the power dissipation of each element must be specified. The power consumption value of the plate heater has been calculated based on the criteria established for its operation mode, both for the hot case and for the cold case.

To know the dissipation that exists in this element when it is in operation, data from the UPMSat-2 battery has been used. As average values obtained from the functional tests, the battery dissipated 0.4 W in discharge and 0.9 during charging.

The power value consumed by the rest of the elements has been obtained from their datasheets. The Table 3.19 lists the different sources of heat that exist inside the experiment.

Table 3.19: Power Consumption of the different elements of the experiment.

Element	Power Consumption (W)	
	COC	HOC
Plate Heater	0.5	0.1
Battery Heater		1.33
Raspberry Pi 3B+		1.8
GPS		0.0858
Pressure Sensor 1		0.000005
Pressure Sensor 1		0.000005
IMU		0.01518
Battery		0.4

3.3. Mathematical model

3.3.1. Atmospheric nodes

ESATAN - TMS is a software developed for the thermal study of space crafts, so the only thermal couplings that can exist in the models created with this software are those that typically exist in the space environment: conduction and radiation. Although it is also possible to model convection, the use of ESATAN modules that allow doing this is very complicated, so another possibility has been sought of considering the relationship that the model could have with the atmosphere, which is the object of study of this project.

To solve this problem, the process that has been followed is to define both the atmospheric nodes and the thermal coupling of these nodes with the rest of the model directly in the different files that the software generates, so that these nodes are not necessarily associated to a geometry.

This means that these nodes do not exist in the geometric model, so they do not have a specific position, but it will be determined by the relationships that these nodes have with the different parts of the model. As it is a relatively small model (3U CubeSat), only three atmospheric nodes are needed inside it, one in each of the cavities that make up the trays, and an outside node that represents the atmospheric air. The position of these nodes can be seen in Figure 3.15.

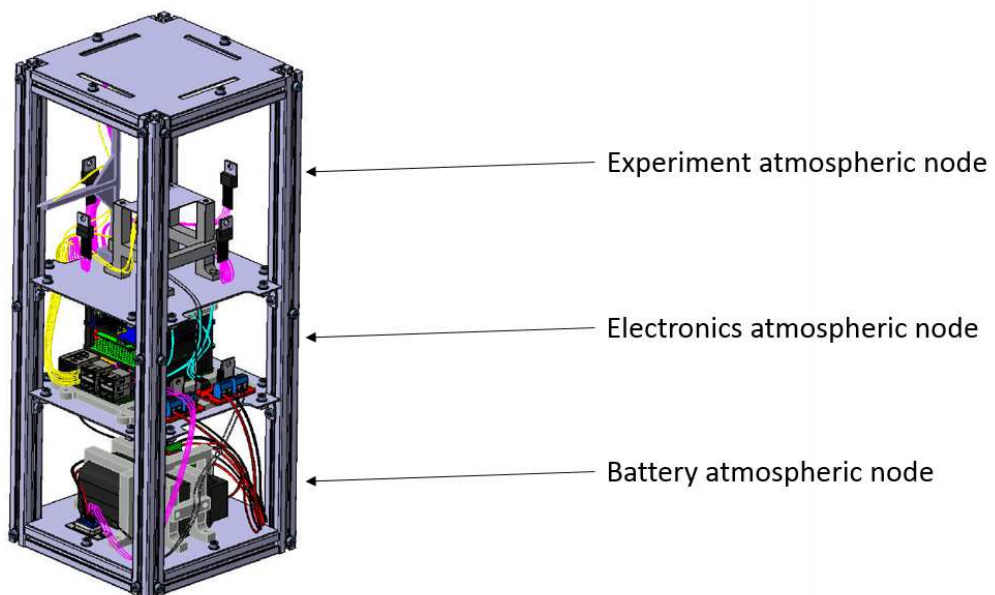


Figure 3.15: Position of the interior atmospheric nodes.

The temperature of the inner nodes is modified according to the properties of the gas at the instant considered and the thermal couplings that are defined, while the temperature of the outer node is considered a restriction when each analysis is carried out and will only vary with the height.

Therefore, to properly define the nodes, it is important to assign the appropriate properties to them. The value of the specific heat of the gas ($C_p = 1000 \text{ J/(kg} \cdot \text{K)}$), as well as its conductivity ($k = 0.025 \text{ W/(m} \cdot \text{K)}$) will be assumed constant and the values of air at 25 °C will be considered. The value of the heat capacity will only need to be defined in the inner nodes (since the temperature of the outer node is a restriction and does not change) and will depend on the volume of the cavity in which the node is located.

The rest of the properties necessary to adequately define the gas and its thermal coupling with the rest of the nodes, such as temperature, density, pressure, etc. will have a value that will be the one defined for the environment at each height, as is as it happened with temperature, or it can be calculated using these properties.

3.3.2. Convective thermal couplings

Once the atmospheric nodes have been defined, the next step to follow is to define the thermal couplings of these nodes with the rest of the model. As previously described, convection heat exchange can be calculated using Equation (1.8) so it is only necessary to determine the convection coefficient to calculate heat exchange. The Equation (1.10) shows that it is possible to obtain the value of h_c if the Nusselt number is known.

Determining the value of the Nusselt number analytically would require extremely complex calculations. Furthermore, as already mentioned, the calculation of the parameters necessary to characterize the value of h_c in each of the model geometries makes the results obtained in this way very imprecise.

Therefore, to measure heat exchange by convection, another work methodology has been followed. Numerous experimental studies have been carried out by various authors seeking to determine the Nusselt number with simple expressions, so, the expressions of the studies that were more similar to the experiment that are being developed have been used to calculate it. The Nusselt number value is obtained through a series of correlations and will depend on the geometry on which the convection acts, its position in space, dimensions, etc. These correlations are described in greater depth below, considering that they have been divided into two groups based on the type of convection: natural and forced.

Natural convection correlations

Natural convection occurs when the fluid is in a state of rest, so there is no external force that forces it to move. However, if a temperature gradient between the fluid and a body immersed in it exists, the part of the fluid that is in contact with said body will be in thermal equilibrium with it, as described when defining the thermal boundary layer.

This change in the temperature of the fluid causes a change in its density, and then, a movement of its particles, since the fluid with more density (the coldest) will tend to be located below the one with less density (the hottest) due to the effect of the gravitational field, which is known as the buoyancy effect.

Assuming a cubic cavity in which the lower surface is heated and has a higher temperature than the fluid that is inside of it, this surface will heat a part of the fluid that will rise, ceasing to be in contact with it and, therefore, cooling down again and descending to be again in contact with the heated surface. This movement of fluid circulation is known as natural convection.

The correlations that allow obtaining the value of the Nusselt number when the convection is natural have been divided into six groups, depending on the geometry and positions of the bodies immersed in the fluid. Although there are infinite correlations, the ones that best fit the model developed have been selected, both due to characteristics and geometry of the experiments.

In order to obtain the Nusselt number, it is necessary to know the value of the Grashof, Prandtl and Rayleigh numbers. The physical meaning of these numbers could be defined as has been done with the Nusselt number, however, for the study that is being carried out this physical meaning is not of interest, so only the expression used will be defined to calculate its value.

The Grashof number, Gr , can be expressed as (from page 368 of [5]):

$$Gr = \frac{g \cdot \beta \cdot |T_i - T_j| \cdot x^3}{\nu^2} \quad [-] \quad (3.1)$$

where g is the acceleration due to gravity, β is the coefficient of expansion, x the characteristic length, T_i and T_j the temperatures of the plate and the temperature of the fluid (air) respectively between which there is convective heat exchange and ν the kinematic viscosity.

The Prandtl number, Pr , when its calculate for the air, can be expressed as (from page 376 of [5]):

$$\text{Pr} = 0.804 - 3.25 \cdot 10^{-4} \cdot \frac{T_i + T_j}{2} \quad [-] \quad (3.2)$$

Finally, the Rayleigh number can be calculated as the product of the Grashof and Prandtl numbers (from page 369 of [5]):

$$\text{Ra} = \text{Gr} \cdot \text{Pr} \quad [-] \quad (3.3)$$

It must also be taken into account that, for vertical plates, the characteristic length considered is its vertical length and for horizontal plates the area of the plate divided by its perimeter.

Vertical surfaces correlations

Churchill and Chu (1975)

The first of the correlations used for the case of vertical plates is the one provided by Churchill and Chu (from page 571 of [5]), since it is the one most frequently found when consulting studies on this topic and is of the form:

$$\text{Nu} = 0.68 + \left\{ \frac{0.387 \cdot \text{Ra}^{1/6}}{[1 + (0.492/\text{Pr})^{9/16}]^{8/27}} \right\}^2 \quad (3.4)$$

Although Equation (3.4) is suitable for most engineering calculations, it is recommended to use the following expression to obtain greater accuracy using:

$$\text{Nu} = 0.68 + \frac{0.670 \cdot \text{Ra}^{1/4}}{[1 + (0.492/\text{Pr})^{9/16}]^{4/9}} \quad 10^3 \leq \text{Ra} \leq 10^9 \quad (3.5)$$

However, it must be considered that Equation (3.4) is valid for any value of the Rayleigh number, while Equation (3.5) is only valid when the value of the Rayleigh number is within a certain range. These correlations are also valid for any value of the Prandtl number.

McAdams (1954)

Another of the most typically found correlations is the one proposed by McAdams Yunus A. Cengel - Heat transfer: A practical approach - 2nd ed. 2002.

[7]. in this case the value of the Nusselt number has the form:

$$\text{Nu} = m \cdot \text{Ra}^n \quad (3.6)$$

where the values of m and n depend on the range of the Rayleigh number, as it can be seen in

Table 3.20.

Table 3.20: Value of the parameters m and n as a function of the Rayleigh number vertical surfaces.

Ra range	m	n
$10^{-1} \leq \text{Ra} \leq 10^4$	1.363	1/6.43
$10^4 < \text{Ra} \leq 10^9$	0.590	1/4
$10^9 < \text{Ra} \leq 10^{12}$	0.129	1/3

Liu (2018)

The value of the Nusselt number proposed by the correlation proposed by Liu [8] also depends on the range in which the value of the Rayleigh number is found, having a constant part and one that varies in the same way as the McAdams correlation:

$$\text{Nu} = 4.3 \quad 10 \leq \text{Ra} \leq 10^3 \quad (3.7)$$

$$\text{Nu} = 1.106 \cdot \text{Ra}^{0.214} \quad 10^3 < \text{Ra} \leq 10^7 \quad (3.8)$$

In addition to a certain value of the Rayleigh number, it must also be considered that this correlation is only valid when the air pressure is between 1000 Pa and 100 kPa.

Suriano (1968)

Suriano's study [9] is especially interesting, the values of the Rayleigh number for which it is valid are very small, a range in which none of the other correlations considered is valid. In this case, the value of the Nusselt number does not have an expression to calculate it, but rather several values of said number are provided based on the Rayleigh number, as can be seen in

Table 3.21.

Table 3.21: Nusselt numbers as a function of the Rayleigh number for vertical plates.

Ra	Nu
0	1.078
0.01	1.079
0.1	1.079
1	1.095
5	1.108
10	1.180
50	2.210
80	2.711
100	2.950
200	3.974
250	4.271
300	4.354

It should also be noted that these values are calculated for a Prandtl number of 0.72.

Chosen correlation

The result of representing all the correlations for vertical plates is shown in Figure 3.16.

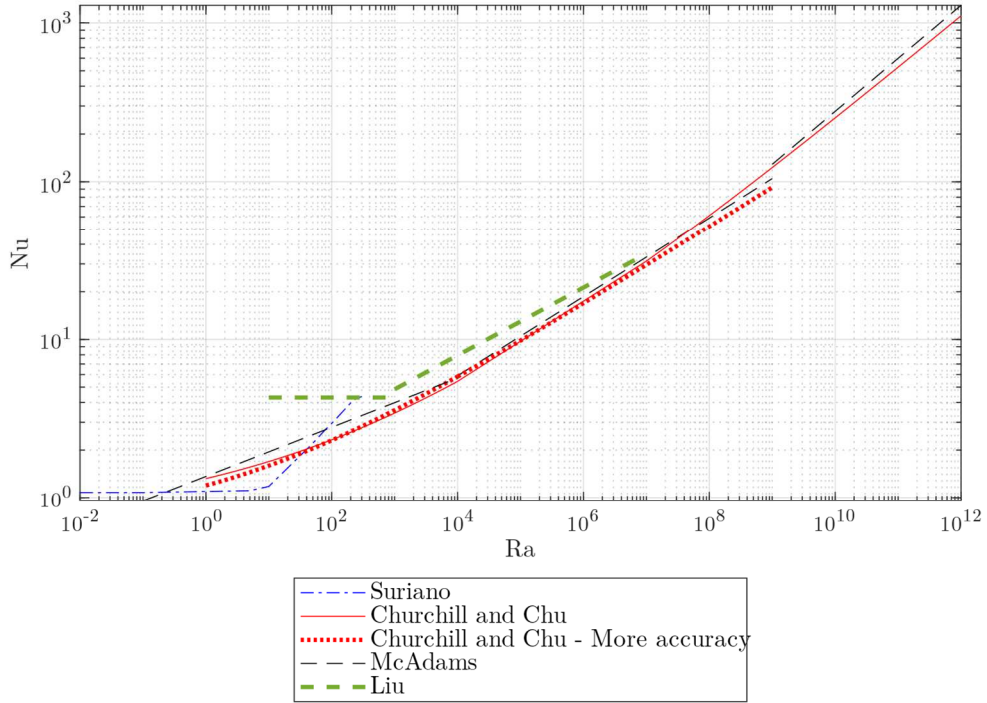


Figure 3.16: Correlations for vertical plates.

Since none of the proposed correlations is valid for any range of Rayleigh number without losing accuracy, the most appropriate correlation has been selected for each section. The first of the correlations that has been discarded is Liu, since it is the one that has the least similarity with the rest. McAdams correlation has also been discarded, since it is very similar to Churchill and Chu one, but this one is considered more appropriate.

The Suriano correlation has been considered for the range $0 \leq Ra \leq 10$, the Churchill and Chu correlation shown in Equation (3.5) for the range $10^2 \leq Ra \leq 10^7$ and the Churchill and Chu correlation shown in Equation (3.4) for the range $Ra \geq 10^{10}$, as it can be seen in Figure 3.17.

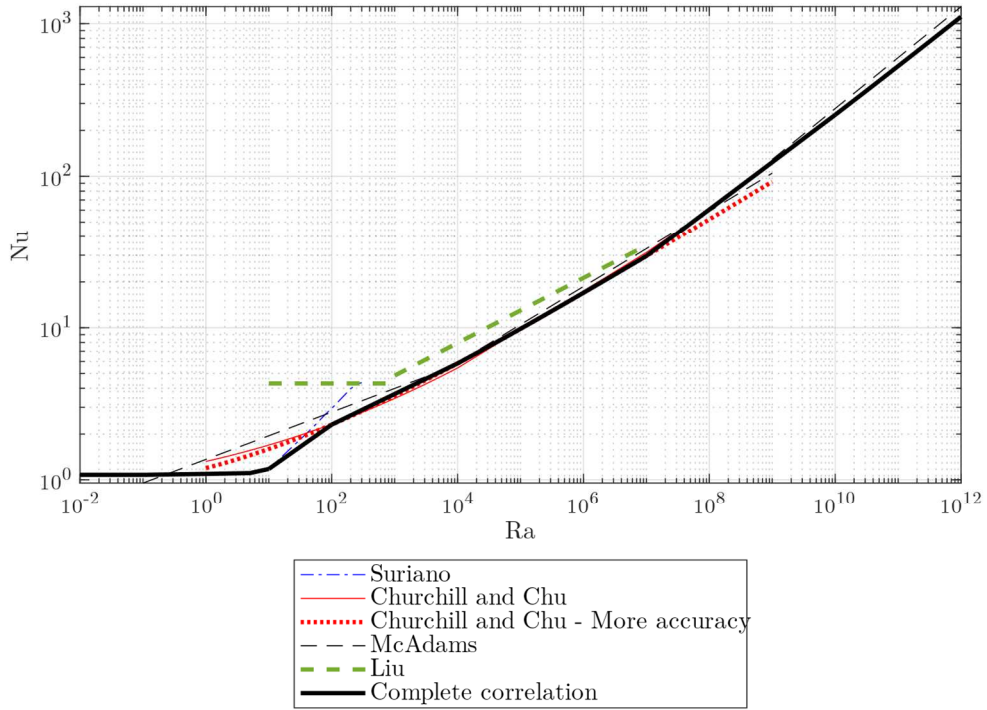


Figure 3.17: Selected correlation for vertical plates.

In the sections in which no correlation has been considered, the value of the Nusselt number is calculated as an interpolation of the extreme values of that range. In this way it is achieved a correlation in which the value of the Nusselt number varies smoothly. The correlation chosen based on the number of the Rayleigh number is shown in the Table 3.22.

Table 3.22: Range of each correlation for vertical surfaces.

Rayleigh	Correlation
$0 \leq Ra \leq 10$	Suriano
$10 \leq Ra \leq 10^2$	Interpolation
$10^2 \leq Ra \leq 10^7$	Churchill and Chu - Equation (3.5)
$10^7 \leq Ra \leq 10^{10}$	Interpolation
$Ra \geq 10^{10}$	Churchill and Chu - Equation (3.4)

Horizontal surfaces correlations

Suriano (1968)

In this case the Suriano correlation [9] is the same as in the case of vertical plates, which means that the value of the Nusselt number is calculated as an interpolation of the values provided in that study.

However, in this case, a differentiation must be made between the upper surface and the lower surface of the plate, since the Nusselt number will be different in each of them. The value of the Nusselt number as a function of the Rayleigh number, for the upper and lower surface, it is shown in the Table 3.23.

Table 3.23: Nusselt numbers as a function of the Rayleigh number for horizontal plates.

Ra	Nu (upper surface)	Nu (lower surface)
0	1.047	1.049
0.01	1.047	1.050
0.1	1.045	1.052
1	1.041	1.104
5	0.946	1.201
10	0.932	1.406
50	1.259	2.879
100	1.330	4.041
200	1.492	6.166
250	1.594	7.194
300	1.678	7.620

As in the case of vertical plates, It should also be noted that these values are calculated for a Prandtl number of 0.72.

Goldstein (1983)

The Goldstein correlation [10] has the same form as those of McAdams and Liu, as can be seen in Equation (3.9) and in Equation (3.10). In this case, it is also necessary to differentiate between the upper surface and the lower surface of the plate.

$$\text{Nu} = 0.621 \cdot \text{Ra}^{1/5} \quad \text{Upper surface} \quad (3.9)$$

$$\text{Nu} = 0.524 \cdot \text{Ra}^{1/5} \quad \text{Lower surface} \quad (3.10)$$

In this case the calculations are considered valid when the Prandtl number has a value of 0.7.

Chambers (1997)

The correlation of Chambers [11] has the following expression:

$$\text{Nu} = m \cdot \text{Ra}^n \quad (3.11)$$

The values taken by the parameters m and n as a function of the value taken by the Rayleigh number for the upper surface of the plate are shown in the Table 3.24 and for the lower surface in the Table 3.25.

Table 3.24: Value of the parameters m and n as a function of the Rayleigh number for horizontal surfaces (upper surface).

Ra range	<i>m</i>	<i>n</i>
$86 \leq \text{Ra} \leq 1.4 \cdot 10^3$	1.030	1/7
$1.4 \cdot 10^3 < \text{Ra} \leq 9.1 \cdot 10^5$	0.677	1/5
$9.1 \cdot 10^5 < \text{Ra} \leq 1.6 \cdot 10^8$	1.076	1/6

Table 3.25: Value of the parameters m and n as a function of the Rayleigh number for horizontal surfaces (lower surface).

Ra range	<i>m</i>	<i>n</i>
$86 \leq \text{Ra} \leq 9.1 \cdot 10^5$	1.033	1/7
$9.1 \cdot 10^5 < \text{Ra} \leq 1.6 \cdot 10^8$	0.747	1/6

Liu (1968)

Liu's correlation [8] is the same as the one used for vertical plates. In this case, in addition, experimental data are available that will later be represented.

Incropera (1996)

The Incropera correlation [5] has the same shape as the previous ones, and it must also differentiate between the upper and lower surface of the plate. However, in this case it must also be considered whether the plate has a temperature higher than air or lower. For the upper surface of a hot plate or the lower face of a cold plate the correlation has the form:

$$\text{Nu} = 0.54 \cdot \text{Ra}^{1/4} \quad 10^4 \leq \text{Ra} \leq 10^7 \quad (3.12)$$

$$\text{Nu} = 0.15 \cdot \text{Ra}^{1/3} \quad 10^7 < \text{Ra} \leq 10^{11} \quad (3.13)$$

For the lower surface of a hot plate or the upper face of a cold plate the correlation has the form:

$$\text{Nu} = 0.27 \cdot \text{Ra}^{1/4} \quad 10^5 \leq \text{Ra} \leq 10^{10} \quad (3.14)$$

Chosen correlation

The result of representing all the correlations for horizontal plates is shown in Figure 3.18 (upper surfaces) and in Figure 3.19 (lower surfaces).

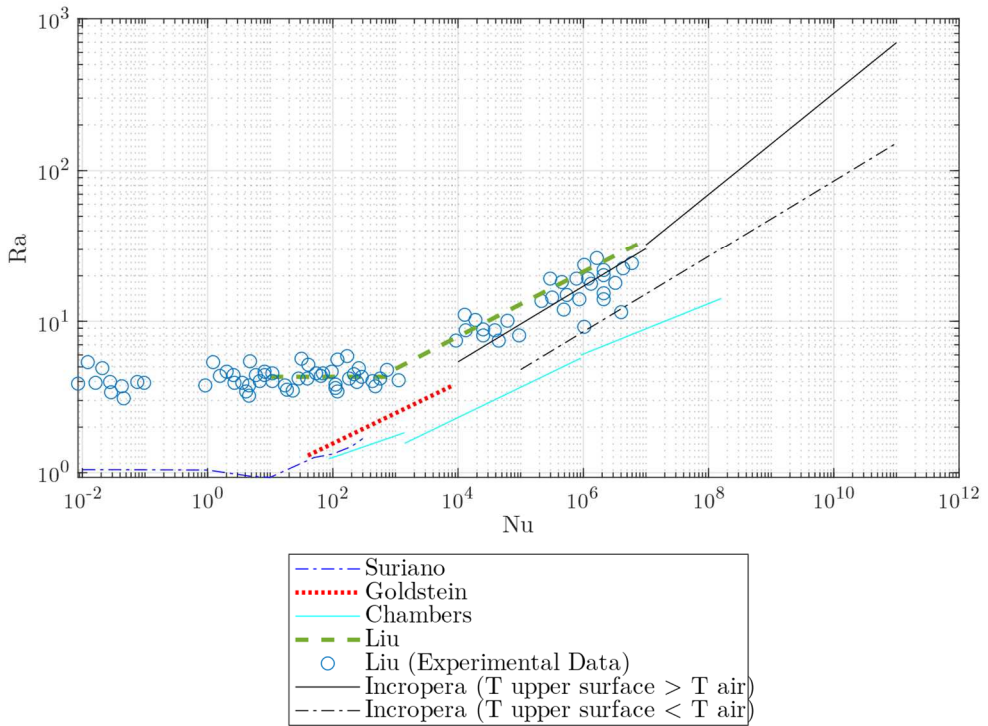


Figure 3.18: Correlations for horizontal plates (Upper surfaces).

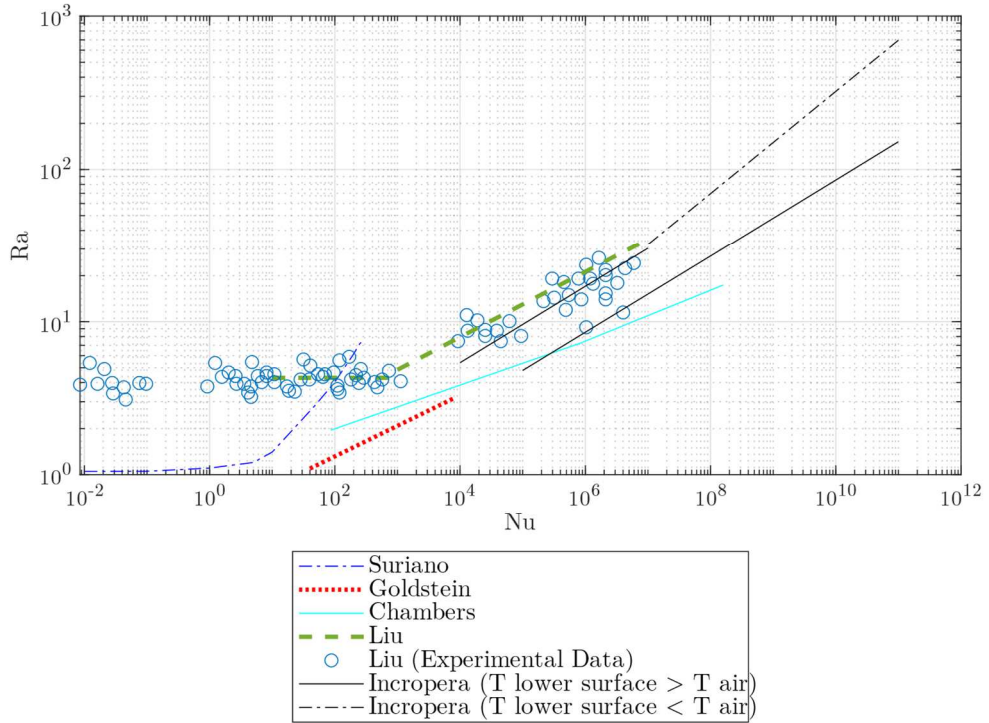


Figure 3.19: Correlations for horizontal plates (Lower surfaces).

As in the case of vertical plates, the Liu correlation has been discarded because it has the least similarity with the rest. The Goldstein correlation for the lower surface of a plate is also very different from the rest so this correlation has also been discarded.

The Suriano correlation has been considered for the range $0 \leq Ra \leq 10$, the Chambers correlation for the range $86 \leq Ra \leq 1400$ and the Incropera correlation in its entire range of application, as it is shown in Figure 3.20 (upper surfaces) and in Figure 3.21 (lower surfaces).

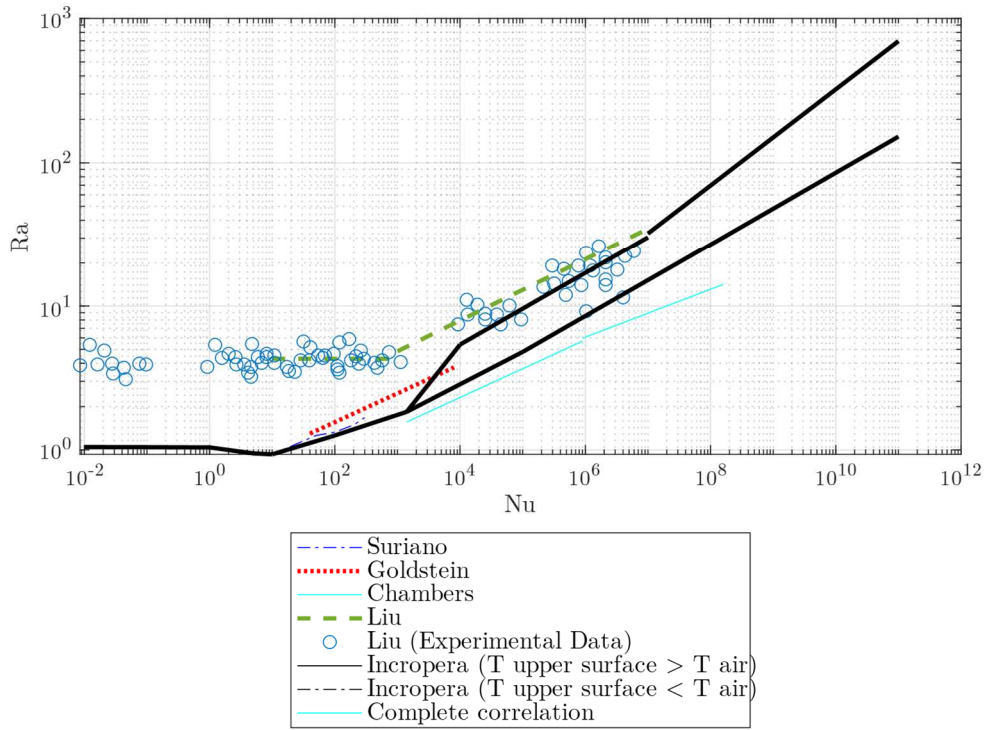


Figure 3.20: Selected correlation for horizontal plates (Upper surfaces).

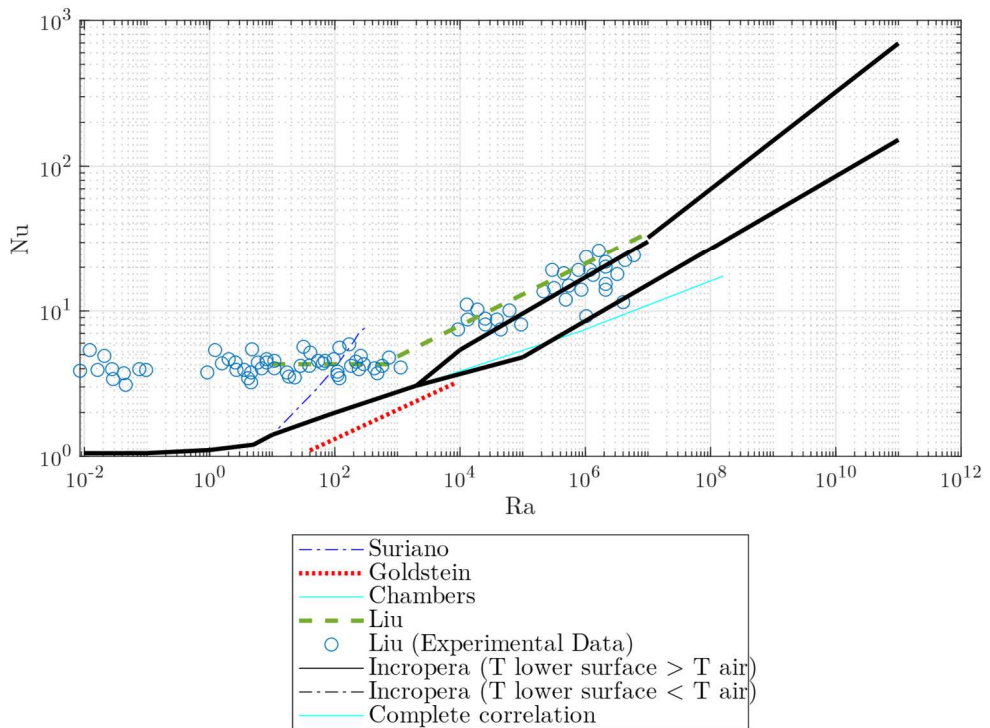


Figure 3.21: Selected correlation for horizontal plates (Lower surfaces).

In the sections in which no correlation has been considered, the value of the Nusselt number is calculated as an interpolation of the extreme values of that range. In this way it is achieved a correlation in which the value of the Nusselt number varies smoothly. The correlation chosen based on the number of the Rayleigh number is shown in the Table 3.26.

Table 3.26: Range of each correlation for horizontal surfaces.

Rayleigh	Correlation
$0 \leq Ra \leq 10$	Suriano
$10 \leq Ra \leq 86$	Interpolation
$86 \leq Ra \leq 1400$	Chambers
$1400 \leq Ra \leq 10^4$	Interpolation
$Ra \geq 10^4$	Incropera

Parallel plates correlations

In this case there is only one correlation for each of the cases, so it will not be necessary to carry out the process followed in the previous cases. The following correlations are valid for parallel plates between which there is not a very high separation, so they are useful to specialize in the case of PCBs (printed circuit boards), and they have been taken from Cengel (from pages 474 and 457 of [6]).

Constant temperature

The correlation can be expressed as:

$$Nu = \left[\frac{576}{(Ra \cdot S/x)^2} + \frac{2.873}{(Ra \cdot S/x)^{0.5}} \right]^{-0.5} \quad (3.15)$$

where S is the separation between the plates and x the characteristic length.

Constant flux

The correlation can be expressed as:

$$Nu = \left[\frac{48}{Ra \cdot S/x} + \frac{2.51}{(Ra \cdot S/x)^{0.4}} \right]^{-0.5} \quad (3.16)$$

where S is the separation between the plates and x the characteristic length.

Forced convection correlations

As previously mentioned, natural convection occurs when there is a temperature gradient within a fluid at rest. Forced convection occurs when fluid has a relative velocity with an immersed body, caused by an external force. This causes that a temperature gradient is generally much greater and therefore the corresponding convection transfer rates are also greater.

In this case, considered that the air in the atmosphere is calm, this fluid speed is the speed at which the balloon rises to its floating height. Also, it is necessary to know the value of the Reynolds number, that can be expressed as (from page 360 of [5]):

$$\text{Re} = \frac{\rho \cdot u_{\infty} \cdot x}{\mu} \quad [-] \quad (3.17)$$

where ρ is the density of air, u_{∞} its velocity, x the characteristic length and μ the dynamic viscosity. All the following correlations are taken from Incropera [5].

Heated plate (T constant) parallel to the flow

The value of the Nusselt number proposed by this correlation is considered valid when the plate temperature is constant and the Prandtl number is greater than 0.6, and has the following expression:

$$\text{Nu} = 0.664 \cdot \sqrt{\text{Re}} \cdot \text{Pr}^{1/3} \quad (3.18)$$

Constant heat flow in a plate parallel to the flow

This correlation is applied in the case of flat plates parallel to the flow (laminar and turbulent) and has the following expression:

$$\text{Nu} = 0.68 \cdot \sqrt{\text{Re}} \cdot \text{Pr}^{1/3} \quad (3.19)$$

Plate perpendicular to the flow

In the case of plates perpendicular to the flow and with a value of the Prandtl number around 0.7, the value of the Nusselt number has the following expression, this correlation being valid when the value of the Reynolds number is in the range $4 \cdot 10^3 \leq \text{Re} \leq 1.5 \cdot 10^4$.

$$\text{Nu} = 0.208 \cdot [(u_\infty \cdot x \cdot \rho/\mu)^{0.731} \cdot (\text{Pr}^{1/3})] \quad (3.20)$$

Cylinders in cross flow

In this case, the correlation is valid for Prandtl number values greater than 0.7 and has the following expression:

$$\text{Nu} = C \cdot \text{Re}^m \cdot \text{Pr}^{1/3} \quad (3.21)$$

where the value of the parameters C and m varies as a function of the value of the Reynolds number as can be seen in the Table 3.27.

Table 3.27: Nusselt numbers as a function of the Reynolds number for cylinders in cross flow.

Re range	C	m
$0.4 \leq \text{Re} \leq 4$	0.989	0.330
$4 < \text{Re} \leq 40$	0.911	0.385
$40 < \text{Re} \leq 4000$	0.683	0.466
$4000 < \text{Re} \leq 40000$	0.193	0.618
$40000 < \text{Re} \leq 400000$	0.027	0.805

In this case, this correlation has been completed with the one proposed by Churchill-Bernstein [12]. This correlation is valid for Reynolds number values in the range $10^2 < \text{Re} \leq 10^7$ and for $\text{Re} \cdot \text{Pr}$ values greater than 0.4 and has the following expression:

$$\text{Nu} = 0.3 + \frac{0.62 \cdot \text{Re}^{1/2} \cdot \text{Pr}^{1/3}}{[1 + (0.4/\text{Pr})^{2/3}]^{1/4}} \cdot \left[1 + \left(\frac{\text{Re}}{282000} \right)^{5/8} \right]^{4/5} \quad (3.22)$$

3.3.3. Comparison with experimental results.

In order to check the suitability of these calculations when modelling convection, it is necessary to compare the value of the Nusselt number obtained analytically using the appropriate correlation with the value obtained by carrying out experimental measurements.

For this, once these correlations were implemented in ESATAN, the Nusselt number has been calculated for a rectangular aluminium plate, 50 x 25 cm and 0.5 mm thick. This plate is attached to the base of the test chamber using four Delrin thermal insulation supports, with a section 0.5 x 0.5 cm and 10 cm in height. Additionally, this plate has a heater attached to its underside.

The experimental process has been carried out in parallel to the development of the finite element model and the results obtained have been taken from [13].

The Table 3.28 compare the Nusselt number obtained through the simulation in ESATAN and through the experimental results.

Table 3.28: Result comparison for different level pressures.

Pressure [mbar]	T_{air} [K]	T_{plate} [K]	Nu_{Experimental}	Nu_{ESATAN}	Ra_{Experimental}	Ra_{ESATAN}
951	288.32	329.48	4.724	4.910	1620.08	1717.93
100	290.38	330.83	2.879	2.430	19.09	18.19
1	292.87	329.36	2.463	2.096	0.00139	0.00163
0.05	293.26	325.20	2.576	2.096	3.10E-06	3.67E-06

It can be seen that the value is not exactly the same. This may be due to the difference that exists in the boundary conditions of each model, or in its realization, since the same power was applied to both models through the heater. However, the values have the same order of magnitude and, moreover, follow the same trend.

3.3.4. Thermal Environment

The balloon float phase takes place at an altitude of around 30 km, being above 99% of the atmosphere. In this situation the environment is very similar to space, which means that the low air pressure (less than 0.3 kPa) makes the heat transfer by convection negligible compared to the heat transfer by radiation, which is caused mainly by the flow of heat from solar radiation, albedo, the Earth infrared radiation and deep space radiation.

As already mentioned, the environmental conditions during this floating phase are very stable. However, the thermal environment that the balloon encounters during the ascent phase is very different, and heat transfer by convection cannot be neglected. During this phase, not only do changes occur in atmospheric parameters such as air pressure, temperature or density, but also radiative fluxes depend to a great extent on the amount of atmosphere above the considered altitude. Furthermore, some of these parameters also depend on the time of day, as the Solar Zenith Angle (SZA) has an influence on radiative heat transfer.

In order to determine which conditions are going to occur during the ascent, it is necessary to carry out an in-depth study of the local conditions where the launch will take place. The environmental parameters to be considered are shown in Figure 3.22.

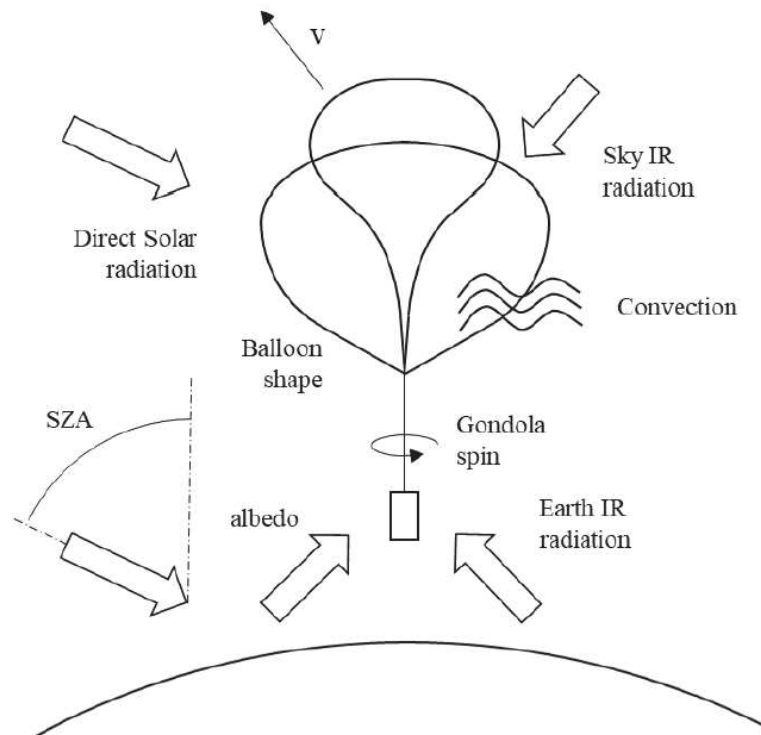


Figure 3.22: Scheme showing the parameters which affect the system during the ascent phase (from [14]).

A brief description of the parameters that affect the ascent of the balloon and therefore will be the boundary conditions of the simulations carried out is shown below.

Radiative influencing parameters

- **Direct solar radiation:** Is the predominant source of heat in most cases. To measure its value, it is necessary to know the solar irradiance, G , a parameter that depends on the altitude due to atmospheric absorption. This parameter also varies depending on the SZA.
- **Sky IR radiation:** When the heat exchange of a satellite with its surroundings is studied, it is known that the equivalent temperature of deep space is around 3 K. However, in this case, since the instrument is in the upper layers of the atmosphere this temperature is considerably higher and must be considered since there is a flow of infrared radiation.
- **Albedo:** Albedo, α , is defined as the radiation emitted by the Sun that is reflected by the Earth. It varies with altitude, but also with the SZA, since as this angle increases, so does the albedo.
- **Solar zenith angle:** The SZA is the parameter that most influences the thermal behaviour of the balloon during the ascent, since it not only influences itself, but also other previously described parameters depend on its value. This parameter is defined based on the time and date of the launch, as well as the latitude and longitude of the balloon.
- **Earth IR radiation:** it is the Outgoing Long Wave Radiation (OLR). this parameter usually varies in the same way that albedo does. To control its influence on the system, the thermo-optic properties can be modified.
- **Gondola spin:** As mentioned, friction with the air could cause the system to start spinning. Most of the Long Duration Balloons (LDB) missions have reaction wheels to provide stability and ensure the required aiming during the mission. However, due to the high density of the air and drag forces, the reaction wheels cannot control the rotation of the nacelle up to a certain altitude, so this spin must be considered.
- **Shape of the balloon:** the shape of the balloon envelope must be considered, since depending on its thermo-optic properties, the radiation it reflects could not be negligible.

Convective influencing parameters

- **Air density:** The convection heat transfer coefficient is proportional to the Reynolds number, which is also proportional to the density of the fluid. The lower it is, the higher the altitude and the lower the convective heat transfer. All the convective parameters have been defined using data from ECMWF MARS [15] and the data used correspond to 15 June to 15 July of the years 2018, 2019 and 2020. The density profile used appears in the Figure 3.23.

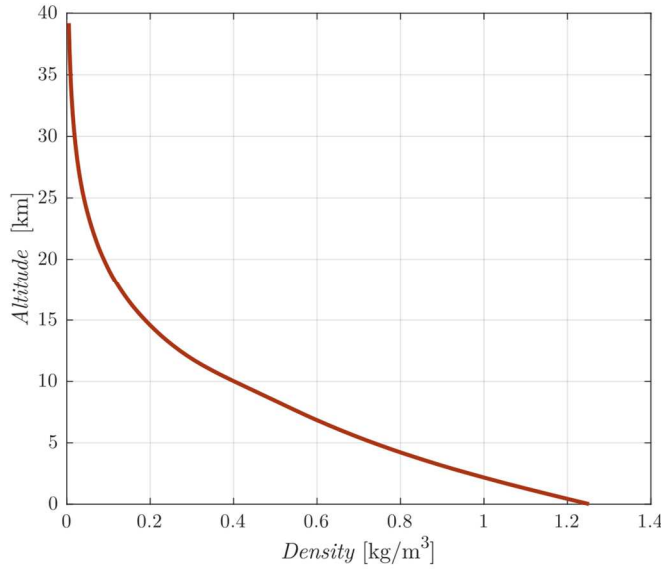


Figure 3.23: Density profile during the ascent of the balloon.

- **Air temperature:** Air temperature not only directly affects convection heat transfer, but also determines the conductivity, k , and dynamic viscosity, μ , of the fluid. The temperature profile during the ascent is shown in the Figure 3.24.

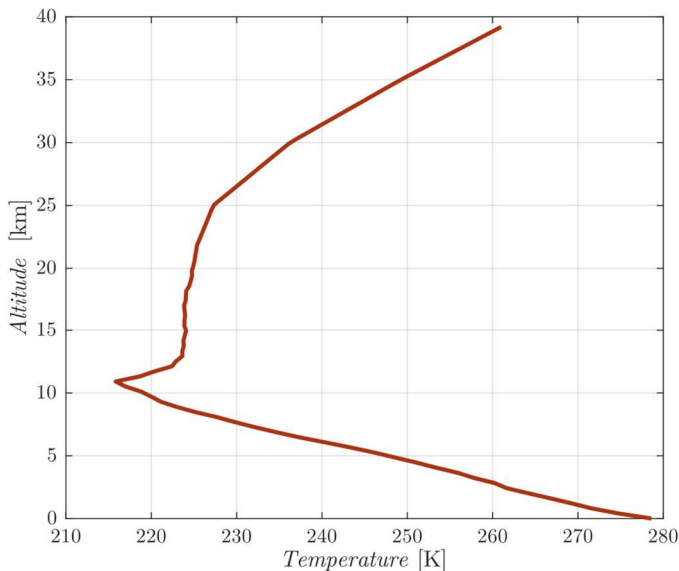


Figure 3.24: Temperature profile during the ascent of the balloon.

- **Ascent speed:** the relative speed between a surface and the fluid is one of the most important parameters when defining forced convection. Assuming that the vertical component of the wind is negligible, the relative speed of the system with the air during the ascent will depend on the ascent speed.
- **Relative horizontal wind speed:** The balloon tends to follow horizontal winds, so its horizontal path will be determined by them. However, when the intensity of this wind is modified, the balloon tends to accelerate, so its effect must be considered.

Radiative ambient.

The approximate launch date was known from the early stages of the project. This makes it possible to model the radiative environment using specific data from the dates on which it will occur, being these dates the months of June and July of the year 2021, because although initially the date was not fixed, it was known what it would be during those months.

This fact makes it necessary to take into account that the SZA varies throughout the day and therefore also the solar charge that the experiment receives. To take this fact into account, the two extreme cases have been considered, which will determine the cold case and the hot case:

- **Cold Operating Case or COC:** In the first case, the launch would occur at 7:00 p.m., which implies that the SZA is very high and therefore the solar and albedo radiative loads are minimal. In this case, the lower limit of the temperature range that each element must withstand will be obtained.
- **Hot Operating Case or HOC:** In the second case, the launch would occur at 12:00 p.m. which implies that the SZA is minimum and therefore the solar and albedo radiative loads cause a greater flow since the direction of said loads is more perpendicular to the faces of the experiment. In this case, the upper limit of the temperature range that each element must withstand will be obtained.

That is, given that the exact time at which the launch will take place is not known and since it is practically impossible to predict which will be with sufficient advance, the two extreme cases that the experiment will have to face must be studied.

3.4. References of this chapter

- [1] Isidoro Martinez. - *Thermo-optical properties*. - Online, 2021.
<http://webserver.dmt.upm.es/~isidoro/>
- [2] Isidoro Martinez. - *Heat conduction in an electronics plate*. - Online, 2021.
<http://imartinez.etsiae.upm.es/~isidoro/bk3/c11/Exercise3.pdf>
- [3] MISUMI. - *Aluminum Extrusions 15mm Square*. - Online, 2021.
<https://uk.misumi-ec.com/vona2/detail/110300465870/?rid=rid2>
- [4] F. Ayape Alonso - *Caso de Estudio 2. Caracterización de la transferencia de calor en placas planas a baja presión*. - 2021.
- [5] F. Incropera, and D. DeWitt. - *Fundamentals of Heat and Mass Transfer* - John Wiley & Sons, Inc., New York City, New York, 4th Edition, 1996.
- [6] Yunus A. Cengel - *Heat transfer: A practical approach* - 2nd ed. 2002.
- [7] McAdams, W. H. - *Heat Transmission*, - 3d ed., chap. 2. New York: McGraw-Hill, 1954.
- [8] Wei Liu, Jing Wang, Yu Li, Zhaowei Zhu, Dianfu Qie & Li Ding, 2018. - *Natural convection heat transfer at reduced pressures*. - Experimental Heat Transfer.
- [9] Francis J. Suriano. and Kwang-Tzu Yang. - *Laminar free convection about vertical and horizontal plates at small and moderate Grashof numbers* - Int. J. Heat Mass Transfer, vol. 11, p. 473-490, 1968.
- [10] R. J. Goldstein and Kei-Shun Lau. - *Laminar natural convection from a horizontal plate and the influence of plate-edge extensions*. - Int. J. Fluid Mech., vol. 129, p. 55-75, 1983.
- [11] B. Chambers and Tien-Yu T. Lee. - *A Numerical Study of Local and Average Natural Convection Nusselt Numbers for Simultaneous Convection Above and Below a Uniformly Heated Horizontal Thin Plate*. - The American Society of Mechanical Engineers, vol. 119, p. 102-108, 1997.
- [12] Churchill, S. W. and M. Bernstein. - *A Correlating Equation for Forced Convection From Gases and Liquids to a Circular Cylinder in Crossflow*. - The American Society of Mechanical Engineers, vol. 99, p. 300-306, 1977.

- [13] F. Ayape Alonso - *Caso de Estudio 3. Caracterización de la transferencia de calor en placas planas a baja presión.* - 2021.
- [14] Instituto Universitario de Microgravitación “Ignacio da Riva” (Universidad Politécnica de Madrid). - *Ascent Phase Thermal Analysis of Long Duration Balloons with B-TASEC and ESATAN-TMS.* - 2021.
- [15] Meteorological Archival and Retrieval System (MARS) of the European Centre for Medium-Range Weather Forecasts (ECMWF). - Online, 2021.
<https://www.ecmwf.int/en/forecasts/access-forecasts/access-archive-datasets>

Chapter 4.

Vacuum chamber tests

4.1. Tests description

Testing in a vacuum chamber is essential in that equipment that will be subjected to this type of low pressure and extreme temperature conditions. The objective of these tests is to demonstrate the survivability of the tested device when faces with these environmental conditions, as well as to confirm the validity of thermal mathematical models and correlation of thermal models. In the Figure 4.1 it can be seen the experiment inside the vacuum chamber.



Figure 4.1: Experiment in the vacuum chamber before the tests.

The realization of these tests has a double purpose, since not only the experiment to be tested has been developed by students, but the construction and design of the chamber itself is part of the work carried out by students at the university. Although the experiment will be subjected to a very extreme thermal environment, it will not face such demanding conditions as those that exist in the space environment, so it is an ideal opportunity to test its operation.

4.1.1. Thermal balance test (TBT)

The first of the tests performed is a Thermal Balance Test (TBT). The objective of the thermal balance test was to ensure the capability of the spacecraft's thermal design to maintain all elements of the spacecraft within the specified temperature range throughout the mission.

The data collected during the thermal balance test are used to update the mathematical thermal model of the experiment to increase its fidelity and give a more accurate prediction of the temperature variations during flight. Once updated, the thermal model will be used to predict more accurately the temperatures of all experiment parts, so, its main objective is to correlate the thermal model.

To carry out a TBT it is necessary to simulate at least two scenarios, a hot case and a cold case, which will represent the most extreme conditions that the tested element will experience.

Although all the elements that dissipate power must be turned on in order to correctly simulate the thermal behaviour of the experiment, during the TBT it is not necessary to check their proper operation.

4.1.2. Low pressure functional test

The first of the tests performed is a Thermal Vacuum Test (TVT). The main objective of this test is to check that all systems work properly during all the operating modes, especially those related to the plate heater power control, software and thermocouple measures. That is, the objective of this type of test is to complement the TBT.

The results obtained in the TVTs are not useful to correlate the thermal model, since it is not intended to obtain a situation of thermal stability, but the data obtained are necessary to verify that the experiment works as it should under the specified temperature and pressure conditions for TBT. For this reason, the results obtained during this test will not be discussed.

4.2. TBT set up

As previously specified, to carry out a TBT it is necessary to modify both the pressure inside the chamber and the temperature of each of its interfaces. In addition, the dissipation of each of the interior elements of the experiment must also be considered, such as the plate heater, the onboard computer or the battery. The values that these parameters have at each moment of the test are specified below.

4.2.1. Pressure profile

Since the test to be carried out has to simulate both the conditions of the hot case, which occurs during the floating phase, and those of the cold case, which occurs at an altitude of 18 km (because it is the point where the temperature of the atmosphere is lower), the pressure inside the chamber will have to vary between these two values, as can be seen in the Figure 4.2.

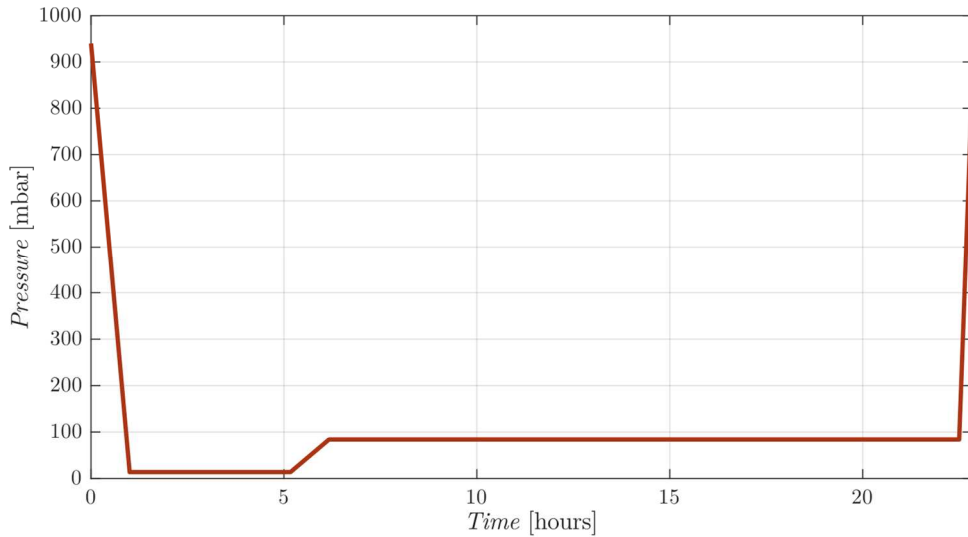


Figure 4.2: Pressure profile of the TBT.

As it can be seen in the Figure 4.2, the pressure value of the HOC is 13.81 mbar and the COC value is 84.08 mbar.

To establish this pressure profile, the time that the vacuum chamber needs to reach the vacuum conditions has been taken into account, as well as the estimated time that is necessary for the thermal interfaces of the vacuum chamber to reach the specified temperatures and the necessary time that the experiment needs to reach the stability conditions that will be specified later.

4.2.2. I/F boundary conditions

In order to define the temperature profile, it is important to know which are the thermal interfaces that the vacuum chamber has. Inside the vacuum chamber there are only two elements whose temperature can be modified. Assuming that the vacuum chamber has a cubic shape, the baseplate would be the bottom face of this cube and the shroud the other five remaining faces. In this case, these interfaces are of two types, conductive and radiative interfaces:

- **Conductive interfaces:** The CubeSat is simply supported over the baseplate through rubber supports without bolts.
- **Radiative interfaces:** Baseplate and shroud are the radiative interfaces.

This means that the experiment will have heat exchange by conduction with the baseplate of the vacuum chamber and heat exchange by radiation with both the baseplate and the shroud.

The way to set these temperatures of these elements is by calculating the sink temperature between the TASEC-Lab and its surroundings, that is, the gondola and the environment. The baseplate temperature will be the linear sink temperature, while the shroud temperature will be the radiative sink temperature. Mathematically these temperatures are obtained in the following way.

The radiative sink temperature, $T_{S,r}$, of the thermal item (node i) with respect to the environment (group of nodes n) is defined by:

$$\left(\sum_{j \in n} [\sigma \cdot GR_{ij}] \right) \cdot (T_i^4 - T_{S,r}^4) = \sum_{j \in n} [\sigma \cdot GR_{ij}] \cdot (T_i^4 - T_j^4) \quad (4.1)$$

The linear sink temperature, $T_{S,l}$, of the thermal item (node i) with respect to the environment (group of nodes n) is defined by:

$$\left(\sum_{j \in n} [GL_{ij}] \right) \cdot (T_i - T_{S,l}) = \sum_{j \in n} [GL_{ij} \cdot (T_i - T_j)] \quad (4.2)$$

Solving for the temperatures sought from Equations (4.1) and (4.2), the value that the interfaces of the vacuum chamber must have during the test is obtained. This calculation must be carried out for both the hot and cold cases, thus obtaining four temperatures, which are listed in the following table:

Table 4.1: Calculated temperature of each interface for the hot and the cold case.

	Baseplate temperature [°C]	Shroud temperature [°C]
HOC	31	42
COC	– 30	– 3

However, the characteristics of the vacuum chamber make the specified baseplate temperature not achievable. The minimum temperature that this can reach is -21 °C, but it has been set at -10 °C, since the time required to reach this minimum was too high, the temperatures that each interface have as specified below:

Table 4.2: Final temperature of each interface for the hot and the cold case.

	Baseplate temperature [°C]	Shroud temperature [°C]
HOC	31	42
COC	– 10	– 3

4.2.3. Temperature profile

As with the pressure profile, the temperature profile must simulate the conditions of both the hot case and the cold case. In this case, it must be taken into account that the baseplate and the shroud are at room temperature until the pressures stabilize at the one set for each case. Then, the temperature control of the thermal interfaces is put into operation and it begins to change. Therefore, once the estimated time to perform the test ends and the pressure begins to change to go from the hot case to the cold case, the baseplate and shroud temperature should also begin to change. Considering the previous considerations, the temperature profile is obtained, which appears in the Figure 4.3.

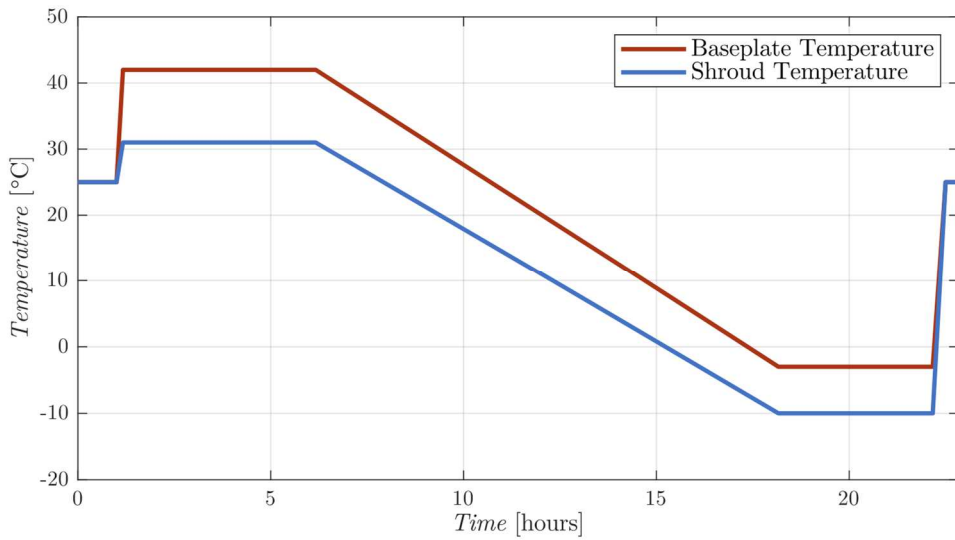


Figure 4.3: Baseplate and shroud temperature profile of the TBT.

It should be mentioned that, although both in the pressure profile and in the temperature profile the test is carried out uninterruptedly, as it can be seen in the Figure 4.2 and in the Figure 4.3, the time limitations in access to the facilities where the vacuum chamber is located caused them to be carried out separately, so a TBT was performed for the hot case and another TBT for the cold case. Therefore, as can be seen in the results that will be discussed later, in both cases the starting temperature is the ambient one and the tempering of the experiment and the different elements of the chamber is carried out simply by turning it off and letting the set reach room temperature by itself.

4.2.4. Power dissipation profile

The last of the variables that must be defined is the power dissipated by each of the elements of the experiment. Although the on-board computer and other electronic elements are switched on from the beginning, the board heater, which is the main source of heat dissipation inside the experiment, only activates when the pressure has stabilized. as was the case with the baseplate and the shroud. The powers dissipated by all the elements are considered constant over time and are specified in the following table:

Table 4.3: Power Consumption of the different elements of the experiment.

Element	Power Consumption (W)	
	COC	HOC
Plate Heater	0.5	0.1 ¹
Raspberry Pi 3B+		1.8
GPS		0.0858
Pressure Sensor 1		0.000005
Pressure Sensor 1		0.000005
IMU		0.01518
Battery		0.4

Notes:

¹ Initially, the value of power dissipated by the plate heater during the cold case was also defined as 0.5, but the high temperature that was reached in said element during the test led to a decision to reduce its value to 0.1.

Although the values that this dissipation was calculated in such a way that they were those that should be experienced during the conditions that occur in the hot case and in the cold case depending on the operating mode, in Figure 4.4 it can be observed that in the hot case this value was adjusted during the test so that the temperature of the plate did not increase excessively, which could damage some of the elements or simply could cause the automatic shutdown of the heater due to safety criteria.

For this reason, for the specification of the plate heater power, there are two curves, Figure 4.4 being the one corresponding to the hot case and Figure 4.5 the one corresponding to the cold case.

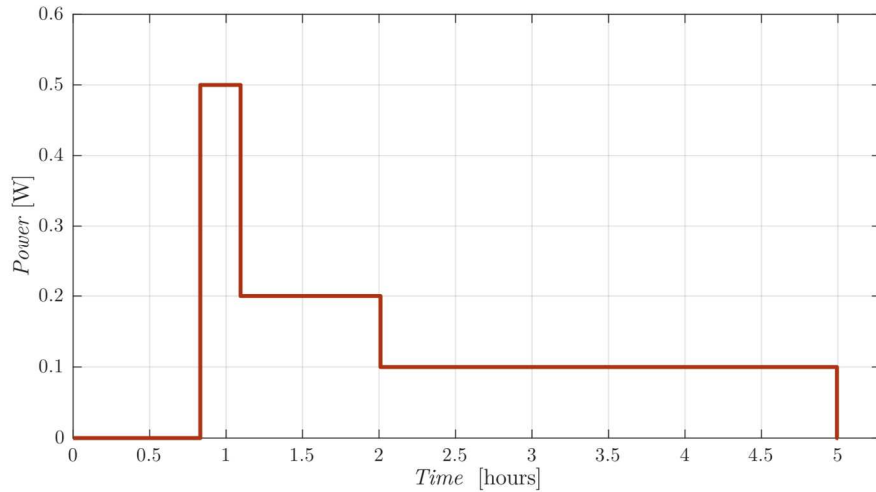


Figure 4.4: Plate heater power dissipation profile for the hot case.

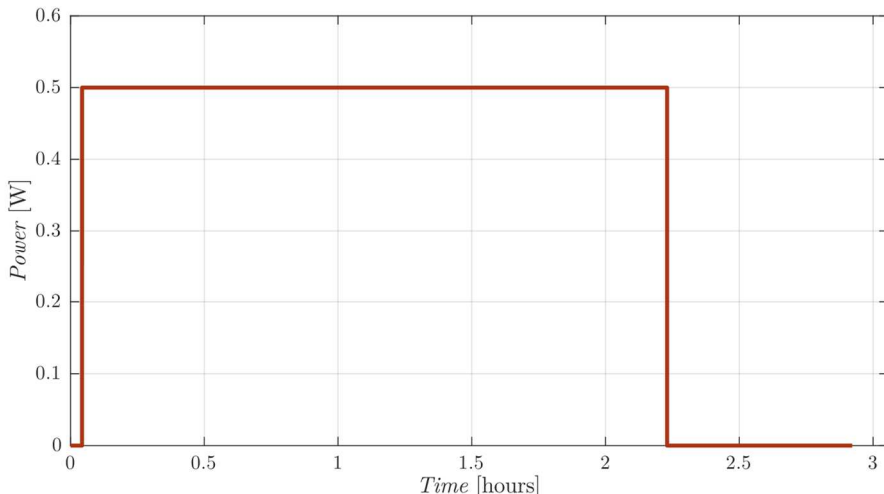


Figure 4.5: Plate heater power dissipation profile for the cold case.

As already specified, a TBT was carried out for the cold case and another for the hot case, whose duration is shorter than that estimated for the complete TBT, as it can be seen in the Figure 4.4 and in the Figure 4.5, since the individual TBTs are terminated when the temperature is stabilizes and shuts down the set.

4.2.5. Thermocouples positions

The position in which the different items are placed must be chosen carefully, since they must measure the thermal behaviour of the experiment with the maximum possible clarity. The vacuum chamber used can measure the temperature at fifteen different points, which added to the internal thermocouples of the experiment itself offer a very complete thermal characterization of its behaviour. The position of each thermocouple in the vacuum chamber is specified in the following table:

Table 4.4: Position of each thermocouple on the elements of the experiment and vacuum chamber.

TC Number	Sensor location	Element
1	Baseplate below the CubeSat.	Baseplate
2	Baseplate at a corner.	Baseplate
3	Shroud surface.	Shroud
4	External surface of lower tray of the CubeSat (Z-) (Battery tray).	CubeSat
5	External surface of upper tray of the CubeSat (Z+).	CubeSat
6	External surface of lateral panel of the CubeSat (X+), half upper area.	CubeSat
7	External surface of lateral panel of the CubeSat (X+), half lower area.	CubeSat
8	External surface of lateral panel of the CubeSat (Y+), half upper area.	CubeSat
9	External surface of lateral panel of the CubeSat (Y+), half lower area.	CubeSat
10	External surface of lateral panel of the CubeSat (X-), half upper area.	CubeSat
11	External surface of lateral panel of the CubeSat (X-), half lower area.	CubeSat
12	External surface of lateral panel of the CubeSat (Y-), half upper area.	CubeSat
13	External surface of lateral panel of the CubeSat (Y-), half lower area.	CubeSat
14	Air horizontally separated from the CubeSat (5 cm from the CubeSat).	Air
15	Air between the lower tray and the baseplate.	Air

To the data obtained by these thermocouples, we must add those obtained by the thermocouples that are located inside the HTL compartment. As already mentioned, these sensors are of the TC74 and PT1000 type, having the second ones the highest precision. The position of each thermocouple is specified in the following table:

Table 4.5: Position of each thermocouple of the CubeSat.

TC Number	Sensor location	Element	Type
1	Internal surface of lateral panel of the HTL compartment (X+).	CubeSat	TC74
2	Internal surface of lateral panel of the HTL compartment (Y+).	CubeSat	TC74
3	Internal surface of lateral panel of the HTL compartment (X-).	CubeSat	TC74
4	Internal surface of lateral panel of the HTL compartment (Y-).	CubeSat	TC74
5	Internal surface of the upper panel of the HTL compartment.	CubeSat	TC74
6	Upper surface of the HTL plate.	HTL	PT1000
7	Lower surface of the HTL plate.	HTL	PT1000
8	Air below the plate.	Air	PT1000
9	Air at the height of the plate.	Air	PT1000
10	Air over the plate (compartment side).	Air	PT1000
11	Air over the plate (compartment centre).	Air	PT1000

4.2.6. Test Results

Once the tests have been carried out, the results that will be discussed below are obtained. To make viewing the figure data easier, the measurements obtained by the twenty-six thermocouples (15 from the vacuum chamber and 11 from the CubeSat) have not been represented together. A graph shows the most representative measurements of the thermocouples in the vacuum chamber and another graph the most representative measurements of the CubeSat thermocouples. The representation of the fifteen thermocouples of the vacuum chamber can be seen in the figures in Annex B.

First, the results obtained during the hot case will be discussed. Figure 4.6 shows the temperatures measured by the selected thermocouples in the vacuum chamber

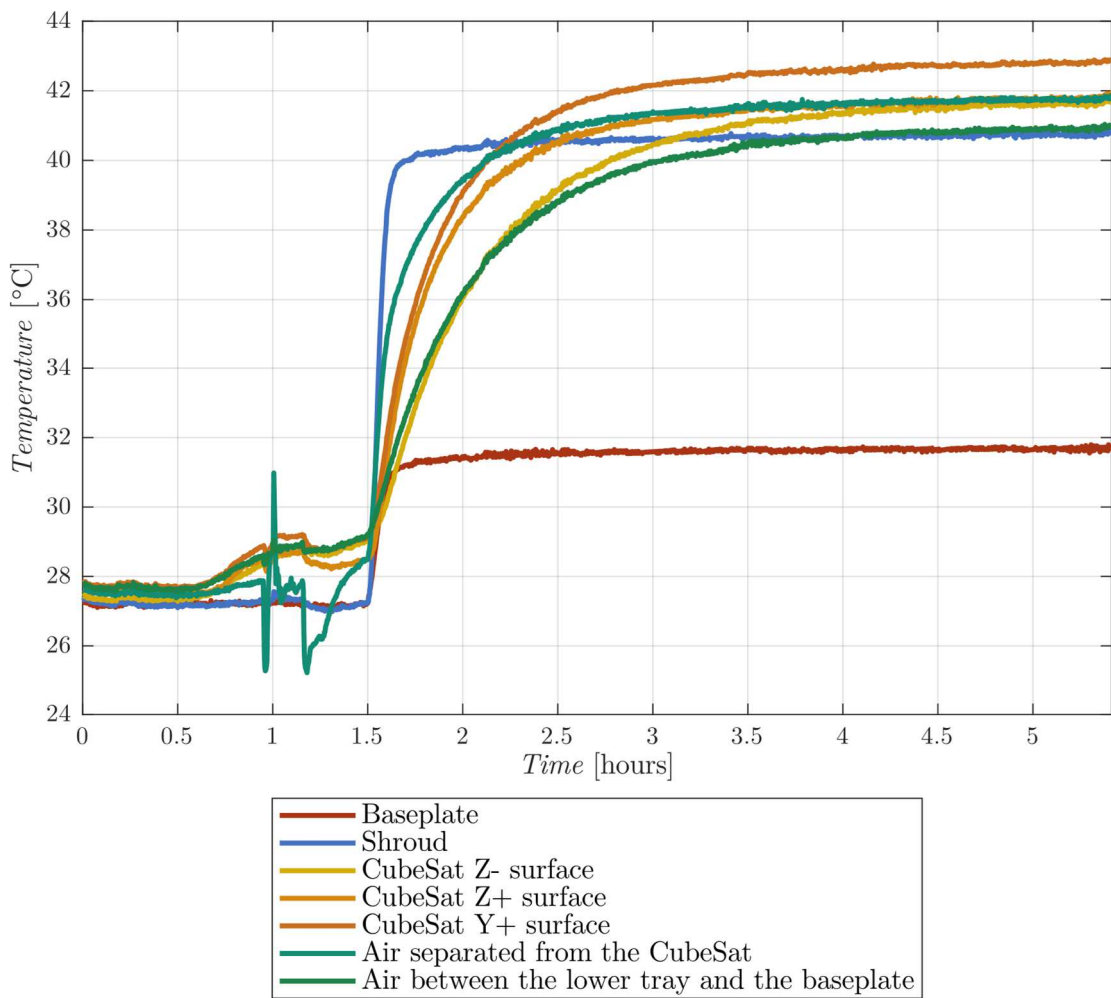


Figure 4.6: Temperature measurements during the hot case test.

It can be seen that around 1.5 hours the temperature of the interfaces of the vacuum chamber changes and therefore the temperature of the entire structure of the experiment begins to change. Two hours later, it can be considered that an equilibrium situation is reached in which the temperatures hardly change, although the test lasts five hours.

Around the first hour it can be observed that there are some fluctuations in temperature measurements. These fluctuations are due to the performance of functional tests before the TBT as well as to the connection of the electronics and the heater of the plate, which is connected before the temperature of the baseplate and the shroud begins to change, as it can be seen in Figure 4.7.

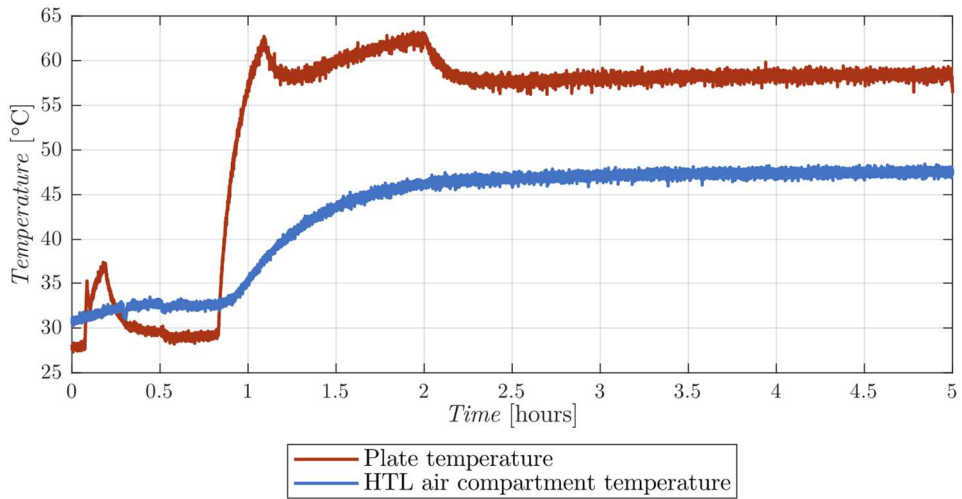


Figure 4.7: Temperature measurements of the plate and the air in the experiment compartment during the hot case test.

The results obtained after carrying out the test corresponding to the cold case can be seen in the following figures. Figure 4.8 shows that the time required to reach equilibrium in the cold case is around two hours. Fluctuations are also observed at the beginning of the test, also due to functional tests as well as a rapid increase in temperature at the end of the test once the vacuum chamber is disconnected.

In this graph it can be seen that the temperature of the baseplate and the shroud are not those that had been previously set, since they are around 0 °C. This is due to the limitations of the vacuum chamber itself, which led to this decision during the test. After the fifth hour a slight increase in temperature is observed, which is due to the ignition of the plate heater, whose temperature can be observed in Figure 4.9.

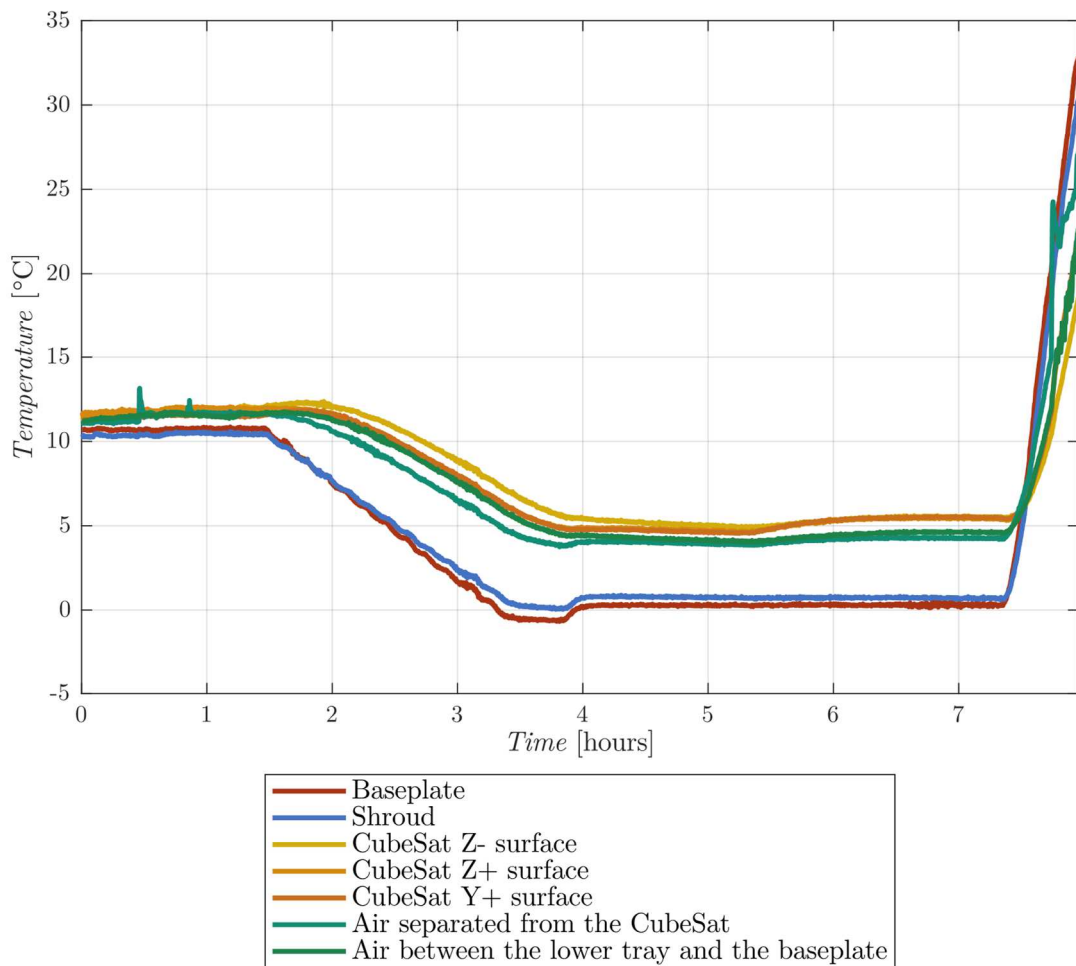


Figure 4.8: Temperature measurements during the cold case test.

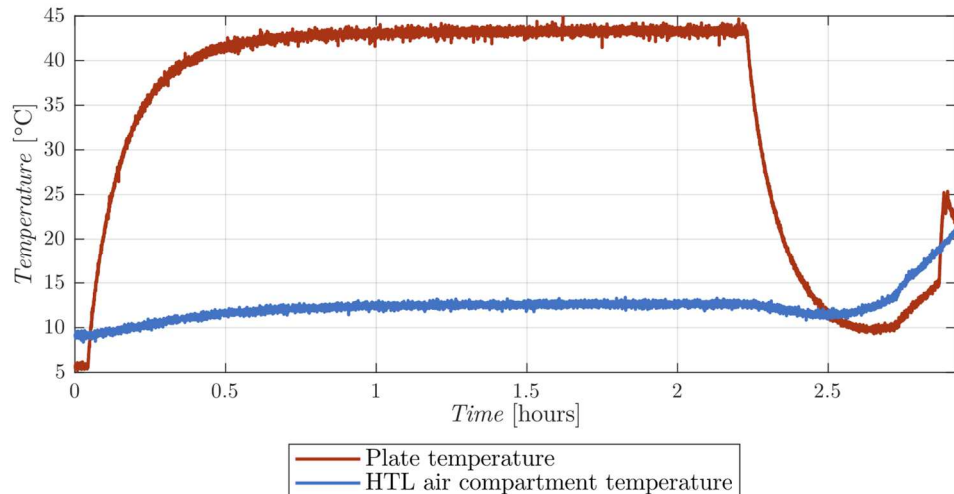


Figure 4.9: Temperature measurements of the plate and the air in the experiment compartment during the cold case test.

4.3. Functional test set up

The objective of this test is to check the operation of the software that controls the change of the HTL operating mode, among other elements. Since the mode change criteria are related to the elapsed mission time or pressure variation, it is not necessary to modify the temperature of the vacuum chamber interfaces. The only parameter that is modified in this test is the pressure, which is done in such a way that it is as similar as possible to the ascent profile but taking into account that it must be ensured that all operating modes occur consecutively. These power modes are the following ones:

- Mode A1: Ascent mode 1.
- Mode A2: Ascent mode 2.
- Mode F1: Float mode 1.
- Mode F2: Float mode 2.
- Mode F3: Float mode 3.

The change of power modes follows the criteria in the following table, occurring automatically.

Table 4.6: Heat Transfer Lab power consumption of each mode, end mode criterion and safety criterion.

Mode	HTL power dissipation (W)	TASEC-Lab status	End mode criterion	Safety criterion (turn OFF the HTL)	Safety criterion (turn ON the HTL) ³
A1	0.8 ⁴	ON	$p \leq p(10 \text{ km})$ and $t_{mission} \geq 30 \text{ min}$		
A2	0.6	ON	$p \leq p(18 \text{ km})$ or $t_{mission} \geq 80 \text{ min}$	$T_{plate} \geq 65 \text{ }^{\circ}\text{C}$ or $ T_{plate} - T_{air} \geq 60 \text{ }^{\circ}\text{C}$	$T_{plate} \leq 55 \text{ }^{\circ}\text{C}$ and $ T_{plate} - T_{air} \leq 50 \text{ }^{\circ}\text{C}$
F1	P_{A2}^1	ON	$t_{F1} \geq 120 \text{ min}$		
F2	$P_{F1}/2^2$	ON	$t_{F2} \geq 120 \text{ min}$		
F3	0	ON	Until end of mission	N/A	N/A
Notes:					
¹ Variable: At least the last power dissipation of Mode A2 or lower.					
² Variable: At least $\frac{1}{2}$ the last power dissipation of Mode F1 or lower.					
³ After meeting the Safety criterion (turn OFF HTL).					
⁴ Power update after the completion of the TBT.					

Chapter 5.

Model correlation

5.1. Introduction

One of the main objectives of carrying out a TBT is, as already mentioned, the thermal correlation, in this case carried out using the ESATAN-TMS software.

From the design of the thermal control system, a certain expected temperature values are obtained, which are calculated based on the worst operational cases (hot and cold). These values will vary with the ones that will be presented in the real element, a deviation that must be considered.

Design margins can be applied to the predicted temperature range and, based on the design temperature range, so, acceptance margins ($\pm 5^{\circ}\text{C}$) and qualification margins ($\pm 10^{\circ}\text{C}$) are applied. In Figure 5.1 it can be seen the temperature margins as defined in the ECSS.

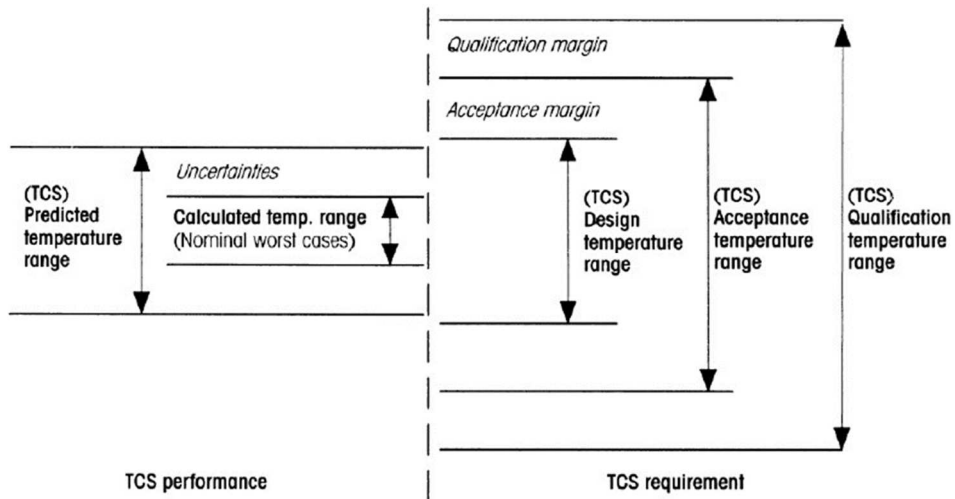


Figure 5.1: Temperature margins defined in the ECSS standard (from [1]).

For a model to be validated, the actual temperature values must be within the acceptance and qualification margins for this element to be suitable for use in the spatial environment.

These uncertainties in temperature measurements can be divided into two groups, the random uncertainties and the epistemic uncertainties. Random uncertainty is associated with natural phenomena, so it cannot be reduced, while epistemic uncertainty is due to the lack of information during the modelling process, so it can be reduced. This means that epistemic uncertainties should be reduced through testing.

The parameters that affect temperature variations of the model have a probability distribution so that these uncertainties can be managed. For this reason, the value of many properties is shown as a mean value plus a certain uncertainty.

Starting from a mathematical model, whose inputs are the independent variables, the constants and certain parameters with a determined statistical distribution, the dependent variables are obtained. When passing the statistical distributions through the mathematical model, a propagation of uncertainties is made, so in this way, the value of these uncertainties can be reduced.

The three most common methods for calculating the uncertainty of temperatures are the use of fixed margins, Statistical Error Analysis (SEA) or Monte Carlo Simulation (MCS). In this case, the use of methods such as the SEA or the development of an algorithm that allows adjusting different parameters of the model implied a workload that was not acceptable for time reasons, so a series of parameters have been modified manually to adjust the thermal model to the results obtained in the TBT.

5.2. ESATAN-TMS predicted results

Once the model has been defined and the profiles of pressure, temperature and power dissipated by the heater on the HTL plate have been defined, the simulation of the test is carried out in ESATAN-TMS. For this, two simulations are made, one for the hot case and the other for the cold case.

5.2.1. Hot Operational Case

In the case of the hot case, the conditions that must be defined to characterize the test are those that were defined to carry out the hot case of TBT. Figure 5.2 shows the temperatures obtained in the same nodes where the thermocouple selection that was made to show the TBT results in the previous chapter are found.

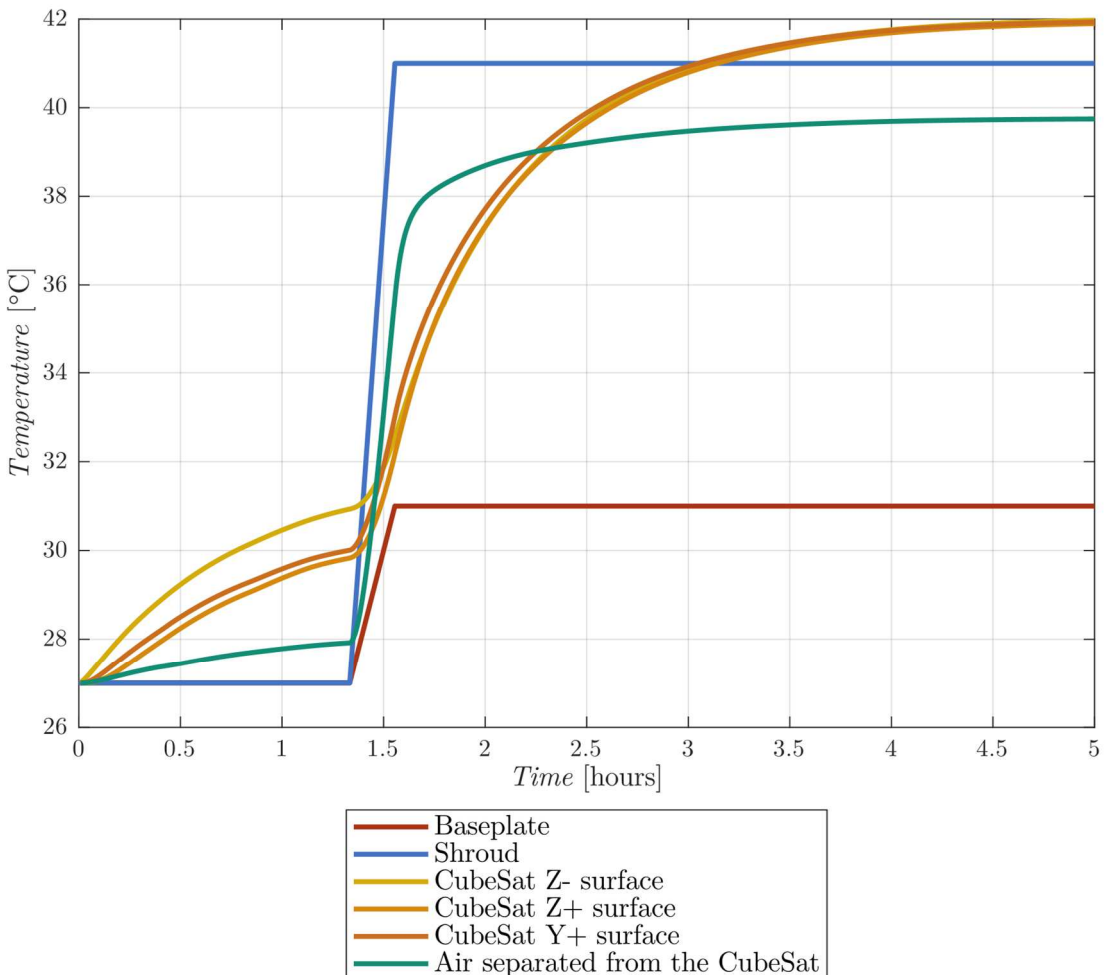


Figure 5.2: Temperature prediction during the hot case simulation.

In Figure 5.2 it can also be seen that the thermal behaviour of the different parts of the structure is very similar to those they had during the test, temperatures that can be seen in Figure 4.6. Later these data will be compared in greater depth.

Regarding the temperature of the plate and the air of the experiment compartment, it can be observed in Figure 5.3 that the behaviour of these temperatures is similar to the behaviour showed during the TBT, which can be seen in Figure 5.4 (analogous to Figure 4.7), but the maximum value of the plate temperatures is higher. and, the temperature change in the air node is slower, which could be a sign that the heat exchange by convection is not as intense as it should be.

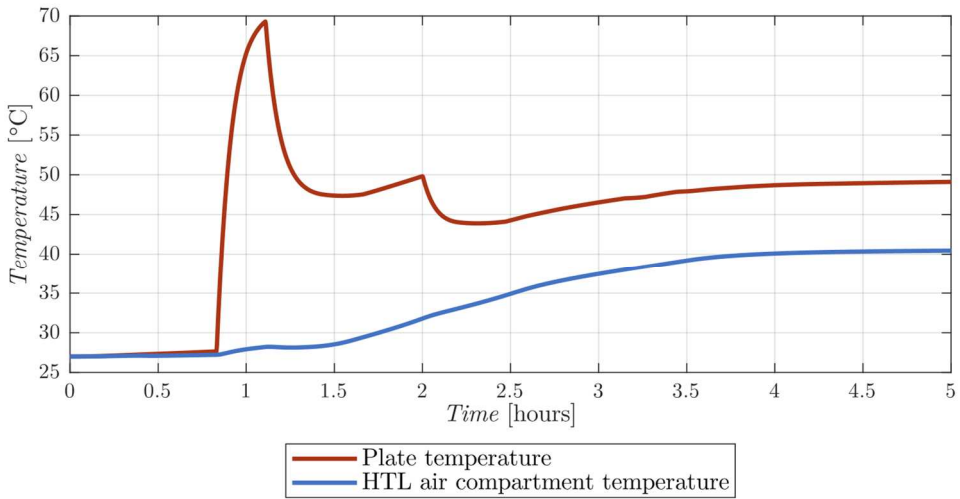


Figure 5.3: Temperature prediction of the plate and the air in the experiment compartment during the hot case simulation.

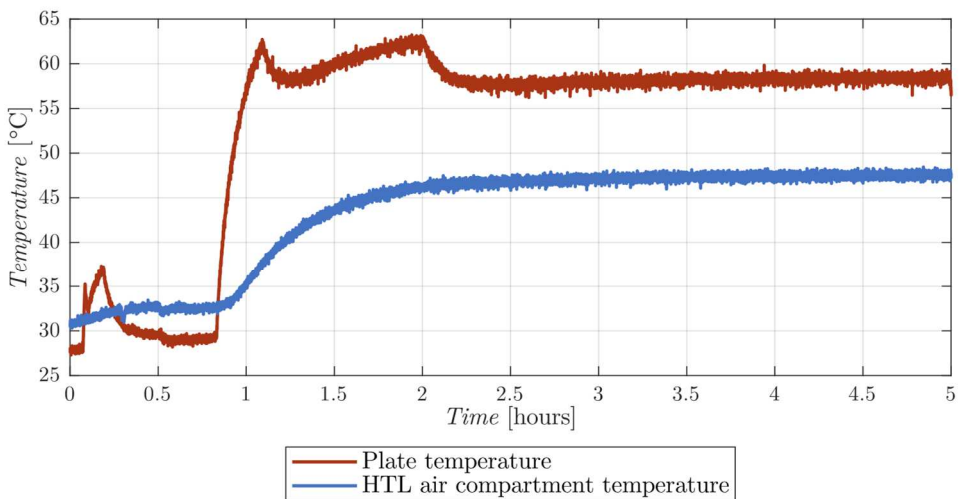


Figure 5.4: Temperature measurements of the plate and the air in the experiment compartment during the hot case test.

5.2.2. Cold Operational Case

As for the hot case, during the cold case simulation the temperatures of the different parts of the structure, showed in Figure 5.5, are very similar to those obtained during the test, which can be observed in Figure 4.8.

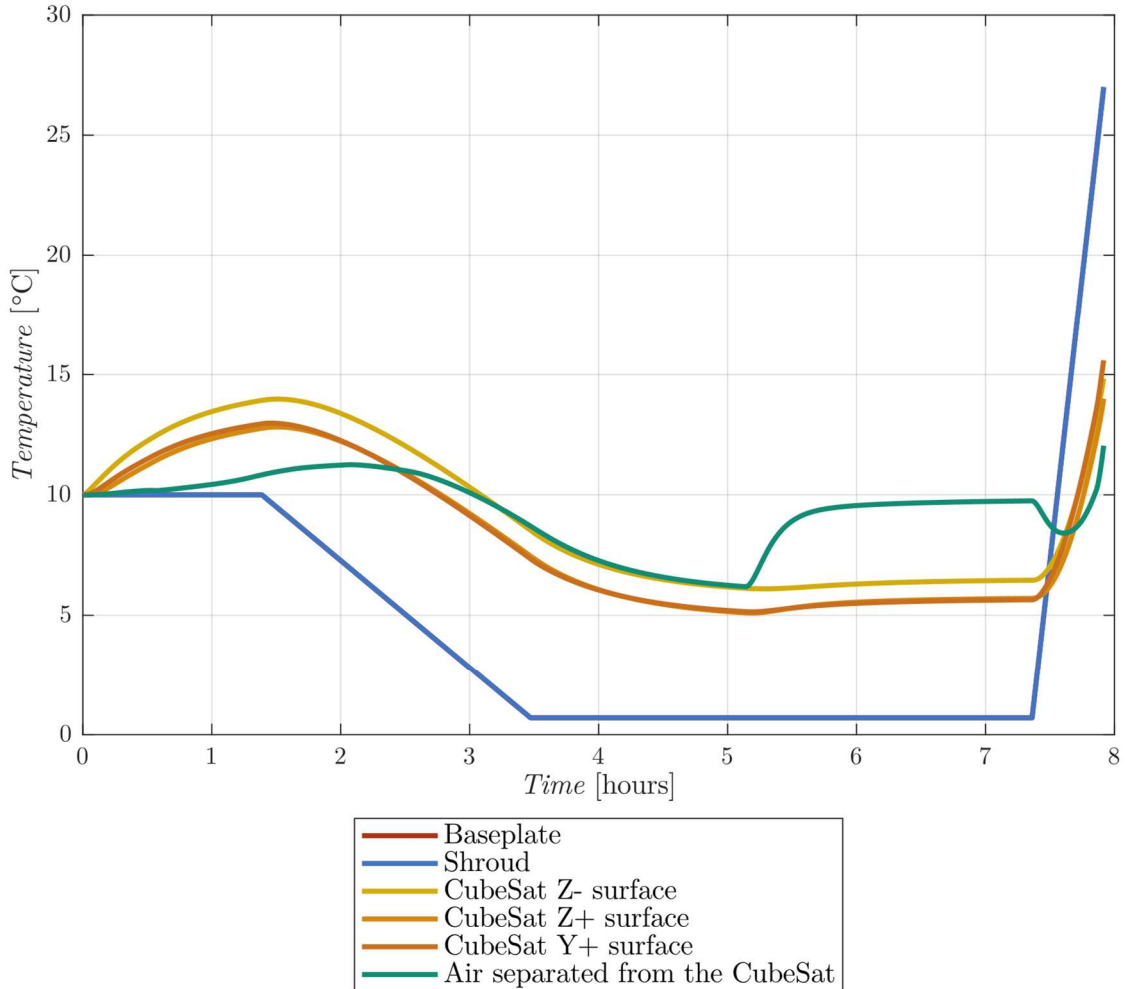


Figure 5.5: Temperature prediction during the cold case simulation.

In the case of the plate temperature, this is also higher in the simulation, as can be seen in Figure 5.6, than those obtained during the tests. which can be seen in Figure 5.8. However, in this case the variation of the air node temperature is more similar to that obtained in the real measurements.

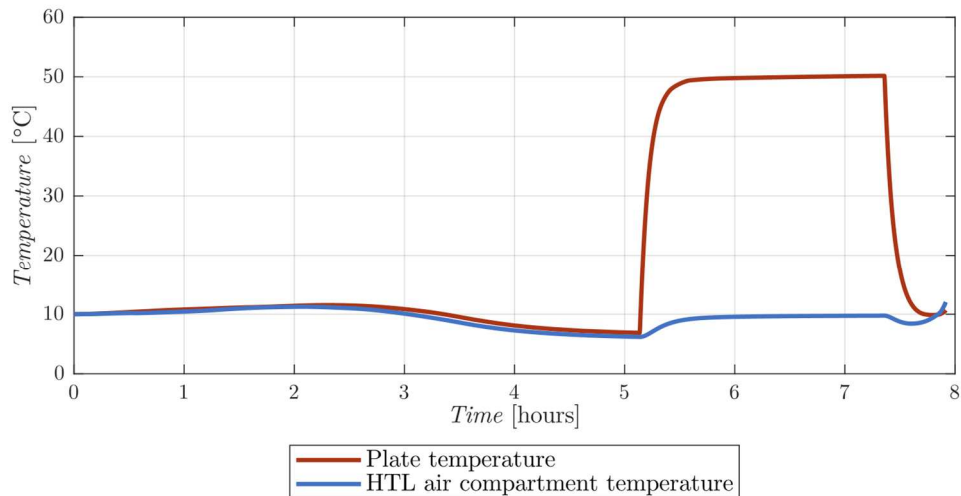


Figure 5.6: Temperature prediction of the plate and the air in the experiment compartment during the cold case simulation.

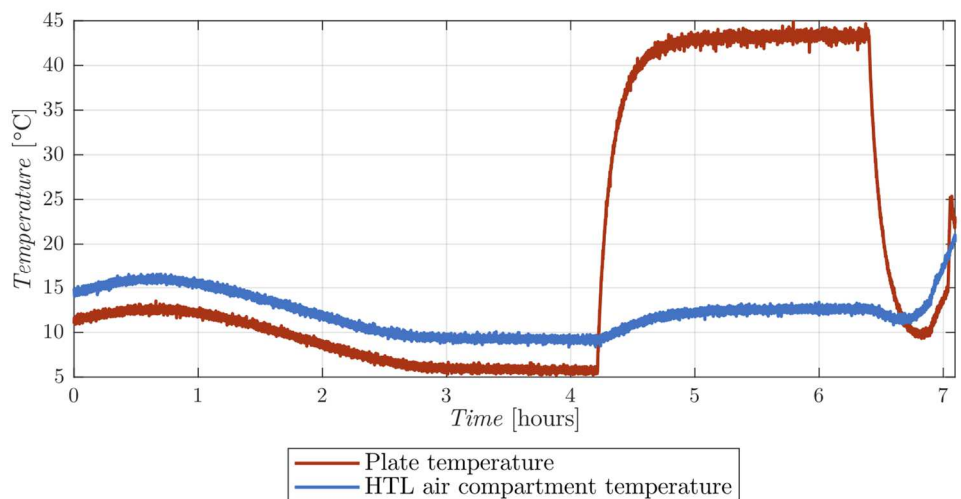


Figure 5.7: Temperature measurements of the plate and the air in the experiment compartment during the cold case test.

5.3. Modified parameters in the model

Since the beginning of the correlation process, a very similar results were achieved in the thermal model to those obtained in the TBT. The main consideration that has been taken to correlate the model is to ignore the temperature that was presented on the HTL plate, since the variations of this element were too high due to the uncertainty that convection introduces in it. However, it has been verified that the trend that the temperature follows does correspond to that shown in the tests.

Therefore, the elements that have been adjusted have been the interfaces between the experiment and the baseplate of the vacuum chamber and the thermal contact conductance between the electronics and the tray on which these elements are screwed.

The modification of the first parameter was motivated by the fact that the structure of the experiment presented a temperature closer to the baseplate in the thermal model than in reality, which was a sign that these elements were more thermally coupled. than they really were.

Initially it was assumed that the aluminium structure was in contact with the baseplate ($GL_{old} = 1.25$). However, during the TBT a series of rubber supports were mounted that isolated the structure of the experiment from the baseplate. Taking this consideration, this interface was modelled, modifying the heat exchange by conduction between these elements ($GL_{new} = 0.108$), reducing it by 91 %.

For the modification of the second parameter, it has been taken into account that the electronics are the main source of heat that is in operation throughout the test. Since the temperatures of the structure are higher than those expected, the electronics must therefore be more isolated from the structure, so the value of the thermal contact conductance was reduced from the value $h_{old} = 300 \text{ W}/(\text{m}^2 \cdot \text{K})$ to the value $h_{new} = 100 \text{ W}/(\text{m}^2 \cdot \text{K})$, that is, it has been reduced by 67 %.

5.4. Correlation of the thermal model

For the thermal model to be considered valid, the temperature deviations measured in the TBT and those predicted by said model must be within certain margins. These typical permitted temperature deviations are included in the corresponding ECSS standard [1], and, broadly speaking, are the following:

- Temperature deviation for inner units < 5 K and for outer units < 10 K. In this case, as the anemometer has not been tested inside the vacuum chamber, it will be assumed that the range is only that of inner units.

$$\Delta T_i = T_{Mi} - T_{Pi} \quad (5.1)$$

where T_{Mi} is the measured temperature and T_{Pi} the temperature predicted by analysis.

- Average temperature deviation within ± 2 K. This value is calculated using the following expression [1]:

$$\Delta T_{mean} = \frac{1}{N} \cdot \sum_{i=1}^N (T_{Mi} - T_{Pi}) \quad (5.2)$$

where N is the number of samples.

- Standard deviation of temperature < 3 K. This value is calculated using the following expression [1]:

$$\sigma_T = \sqrt{\frac{1}{N-1} \cdot \sum_{i=1}^N [(T_{Mi} - T_{Pi}) - \Delta T_{mean}]^2} \quad (5.3)$$

The results obtained after applying equations (5.1), (5.2) and (5.3) using the data obtained from the TBT and from the simulations carried out in ESATAN-TMS are detailed below.

5.4.1. Temperature deviation

The first of the requirements that must be met is that the difference in temperatures measured in the tests in the vacuum chamber and those predicted in the ESATAN simulation be less than 5 K.

Hot Operational Case

Figure 5.8 shows the temperature difference between the value measured by the vacuum chamber thermocouples and the predicted value at each instant of time for the hot case, while the Figure 5.9 the temperature difference between the value measured by the CubeSat thermocouples and the predicted value.

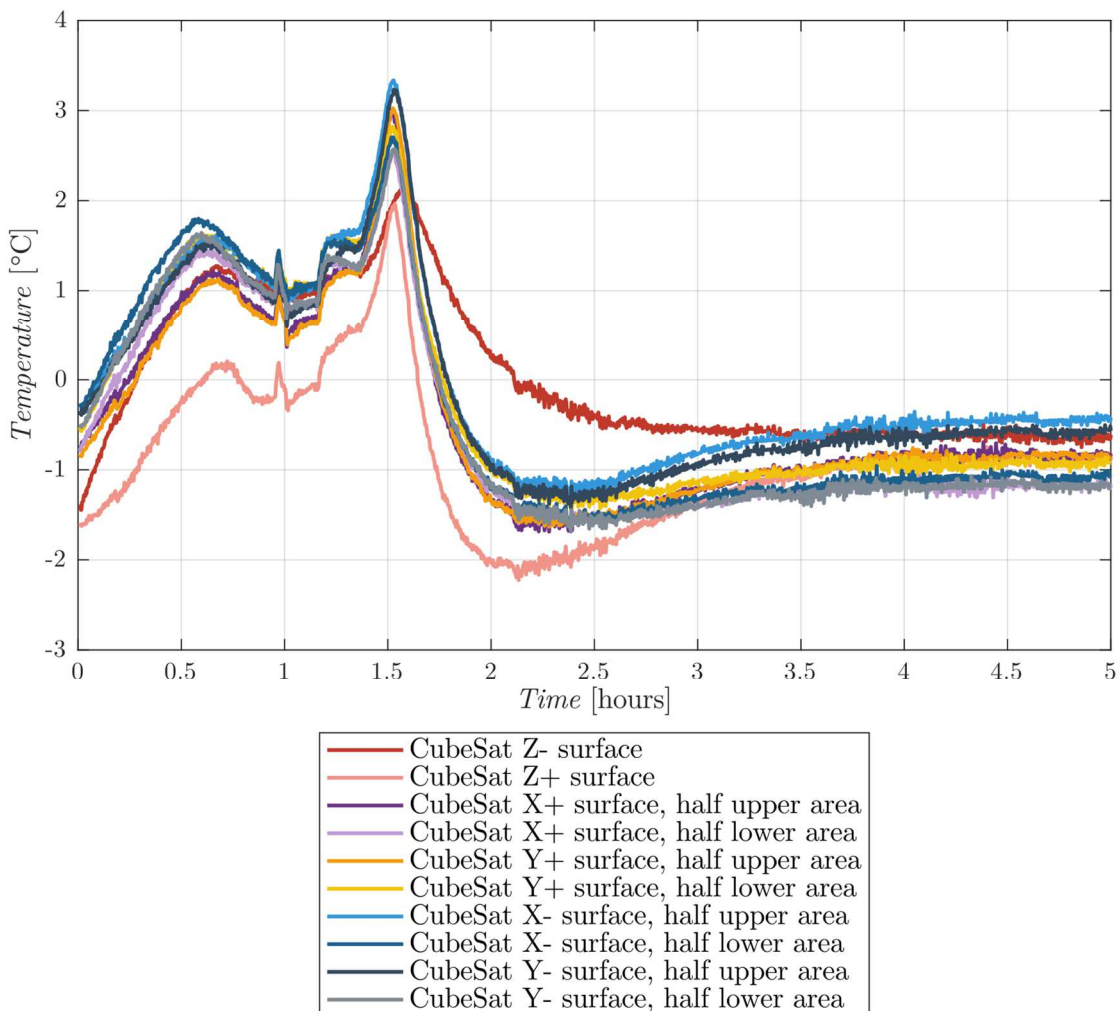


Figure 5.8: Temperature difference between the measured by the vacuum chamber thermocouples value and the predicted value at each instant of time during the hot case.

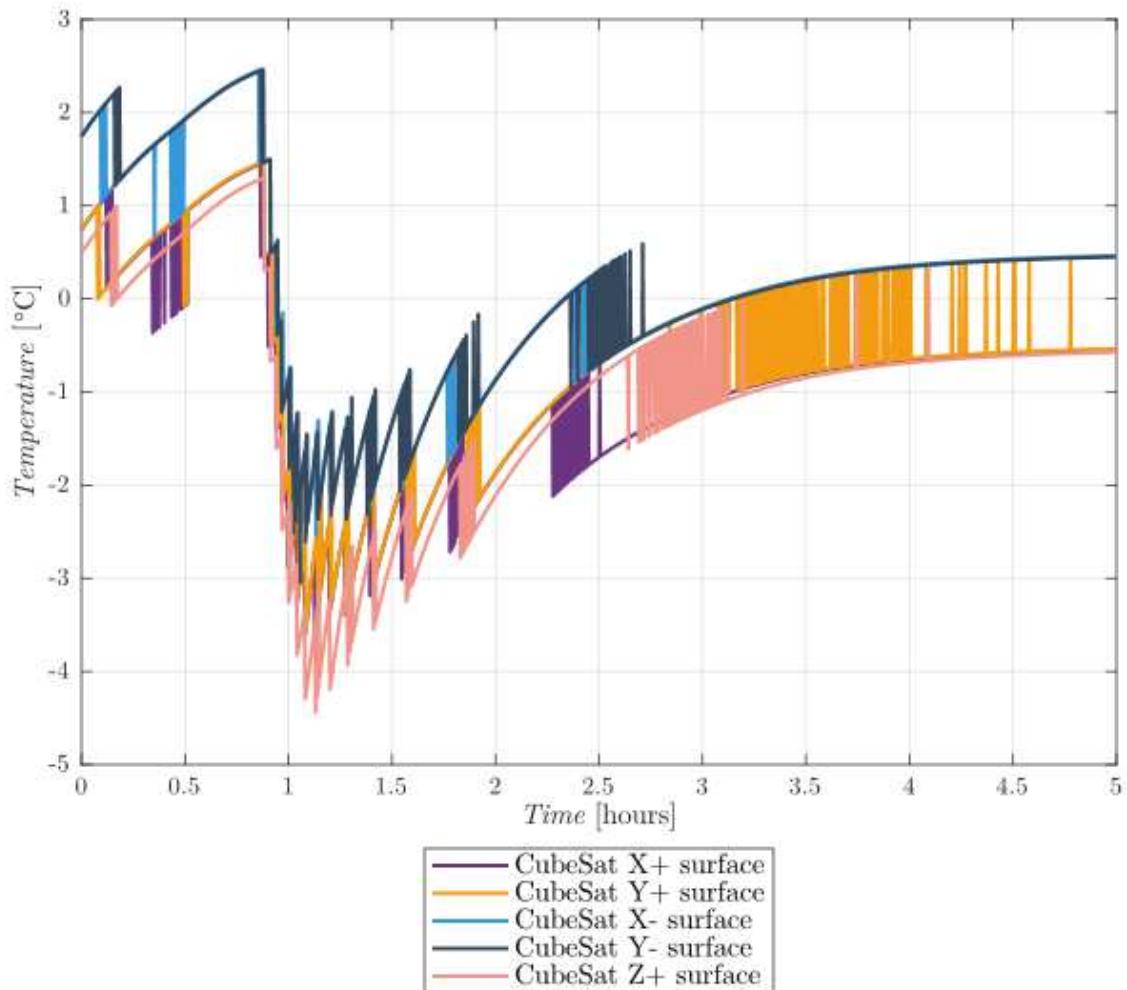


Figure 5.9: Temperature difference between the measured by the CubeSat thermocouples value and the predicted value at each instant of time during the hot case.

In both figures it can be seen that this condition is fulfilled in all instants of time, especially at the moment in which equilibrium is reached, where the maximum temperature difference is less than 2 K. The point at which the most difference is the moment in which the temperature of the thermal interfaces of the vacuum chamber begins to change, which may be due to a poor synchronization between the test time and the ESATAN simulation time or due to a slower variation of the temperature in the simulation.

Cold Operational Case

The Figure 5.10 shows the temperature difference between the measured value and the predicted value at each instant of time for the cold case, while the Figure 5.11 the temperature difference between the value measured by the CubeSat thermocouples and the predicted value.

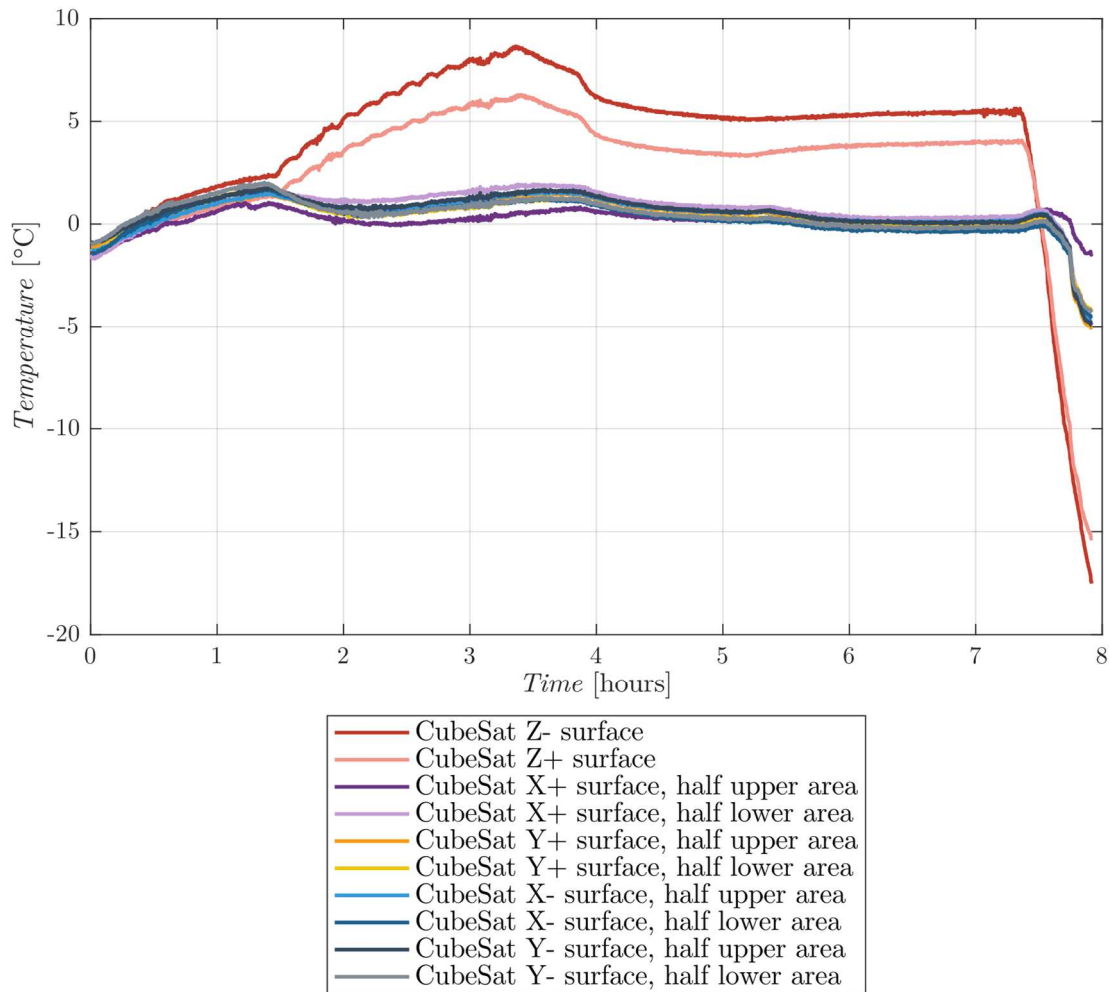


Figure 5.10: Temperature difference between the measured by the vacuum chamber thermocouples value and the predicted value at each instant of time during the cold case.

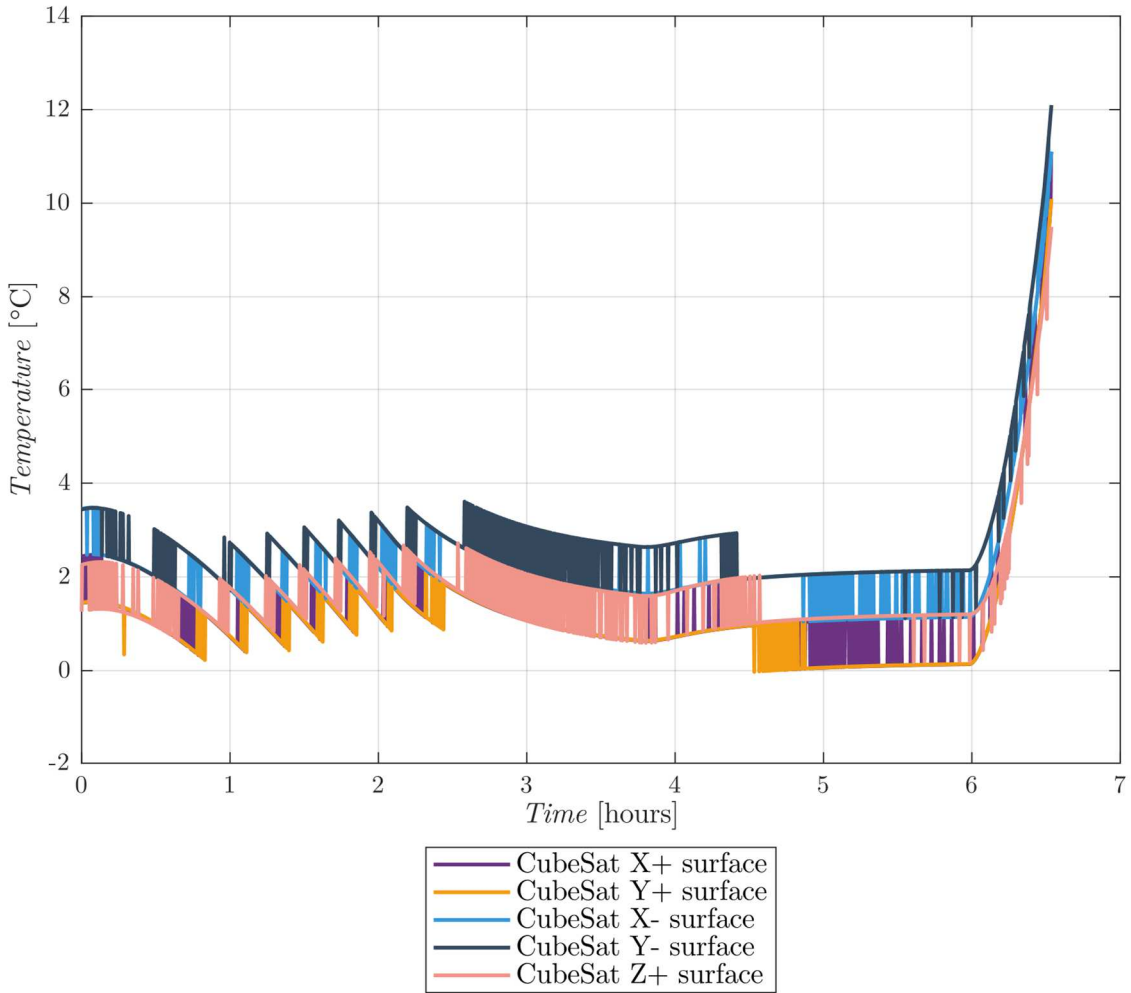


Figure 5.11: Temperature difference between the measured by the CubeSat thermocouples value and the predicted value at each instant of time during the cold case.

In this case, it can be observed that the requirement is not fulfilled in all instants of time, since the external faces $Z +$ and $Z -$ of the experiment have a temperature difference that is around 5 K in equilibrium. This may be due to the fact that the convection heat exchange on horizontal surfaces is lower than the expected.

In the case of the TC74 thermocouples the condition is fulfilled in less moments. One of the main reasons why this occurs is the fact that these thermocouples have a higher margin of error, which causes the measurement obtained to fluctuate.

5.4.2. Average temperature deviation

The second of the requirements that must be met is that the average temperature deviation is less than ± 2 K. The results obtained are shown in Table 5.1. In that table it can be seen that this requirement is met on all surfaces in the hot case, but not in the cold case. As with the previous requirement, faces Z+ and Z- do not meet this requirement. To carry out this calculation, the data of the last half hour of the TBT of the cold case have been omitted, since these data have been taken when the test had finished.

Table 5.1: Average temperature deviation of each vacuum chamber thermocouple sensor for the hot and the cold case.

TC Number	Sensor location	Average temperature deviation (K)	
		Hot case	Cold case
4	External surface of lower tray of the CubeSat (Z-) (Battery tray).	0.0195	-4.8957
5	External surface of upper tray of the CubeSat (Z+).	0.8812	-3.3636
6	External surface of lateral panel of the CubeSat (X+), half upper area.	0.4406	-0.2296
7	External surface of lateral panel of the CubeSat (X+), half lower area.	0.5406	-0.8732
8	External surface of lateral panel of the CubeSat (Y+), half upper area.	0.4606	-0.6191
9	External surface of lateral panel of the CubeSat (Y+), half lower area.	0.3129	-0.5039
10	External surface of lateral panel of the CubeSat (X-), half upper area.	0.0424	-0.6499
11	External surface of lateral panel of the CubeSat (X-), half lower area.	0.4047	-0.4302
12	External surface of lateral panel of the CubeSat (Y-), half upper area.	0.1528	-0.7938
13	External surface of lateral panel of the CubeSat (Y-), half lower area.	0.5034	-0.5659

In the case of TC74 thermocouples, something similar happens to what happened with the thermocouples of the vacuum chamber. The requirement is met on all the surfaces for the hot case but not for the cold case. However, in this case the value of the average temperature deviation is not so different from the rest as in the previous case, so it can be attributed to a lack of precision in the measurement.

Table 5.2: Average temperature deviation of each CubeSat thermocouple sensor for the hot and the cold case.

TC Number	Sensor location	Average temperature deviation (K)	
		Hot case	Cold case
1	Internal surface of lateral panel of the HTL compartment (X+).	0.9455	-1.0235
2	Internal surface of lateral panel of the HTL compartment (Y+).	0.6673	-0.8893
3	Internal surface of lateral panel of the HTL compartment (X-).	-0.0934	-2.0157
-1.0235	Internal surface of lateral panel of the HTL compartment (Y-).	-0.1215	-2.5290
-0.8893	Internal surface of the upper panel of the HTL compartment.	0.9825	-1.508

In the tables above, the values that meet the requirement are highlighted in green and those that do not meet it in red.

5.4.3. Standard deviation of temperature

The last of the requirements that must be met is that the standard deviation of temperature is less than 3 K. The results obtained are shown in Table 5.3. In this case, it can be observed that this requirement is fulfilled for all surfaces, both in the hot and cold cases.

Table 5.3: Standard deviation of temperature of each vacuum chamber thermocouple sensor for the hot and the cold case.

TC Number	Sensor location	Standard deviation of temperature (K)	
		Hot case	Cold case
4	External surface of lower tray of the CubeSat (Z-) (Battery tray).	0.8196	2.2906
5	External surface of upper tray of the CubeSat (Z+).	0.7774	1.8540
6	External surface of lateral panel of the CubeSat (X+), half upper area.	1.0166	0.3953
7	External surface of lateral panel of the CubeSat (X+), half lower area.	1.1109	0.6824
8	External surface of lateral panel of the CubeSat (Y+), half upper area.	1.0055	0.5545
9	External surface of lateral panel of the CubeSat (Y+), half lower area.	1.1059	0.5727
10	External surface of lateral panel of the CubeSat (X-), half upper area.	1.0276	0.5777
11	External surface of lateral panel of the CubeSat (X-), half lower area.	1.1965	0.6437
12	External surface of lateral panel of the CubeSat (Y-), half upper area.	1.0252	0.5811
13	External surface of lateral panel of the CubeSat (Y-), half lower area.	1.1554	0.6085

For TC74 thermocouples the requirement is also met on all surfaces, both for hot and cold cases.

Table 5.4: Standard deviation of temperature of each CubeSat thermocouple sensor for the hot and the cold case.

TC Number	Sensor location	Standard deviation of temperature (K)	
		Hot case	Cold case
1	Internal surface of lateral panel of the HTL compartment (X+).	1.2016	0.5658
2	Internal surface of lateral panel of the HTL compartment (Y+).	1.1139	0.5643
3	Internal surface of lateral panel of the HTL compartment (X-).	1.0651	0.5542
4	Internal surface of lateral panel of the HTL compartment (Y-).	1.0930	0.5443
5	Internal surface of the upper panel of the HTL compartment.	1.1108	0.4842

5.5. Correlation conclusions

In view of the results obtained it can be concluded that, in general, the ESATAN approximation is good, but a large error occurs in the outer horizontal surfaces of the satellite when the cold case of TBT is carried out.

To consider the correlation as good, however, the results obtained on the HTL plate must be ignored, since in this element the error is high and the convection acting on that element must be reviewed.

5.6. References of this chapter

- [1] European Space Agency - *ECSS-E-ST-31C, Thermal control general requirements* - 15 November 2008.

(Page intentionally left blank).

Conclusions and future work

Once the data from the different tests have been analysed and adequately compared with the data obtained from the simulations carried out in ESATAN, one of the first observations that can be made is the need to adjust the heat exchange by convection, especially the one that produced between the air and the horizontal surfaces, since both the outer horizontal faces of the experiment and the plate itself show that this heat exchange is less intense in the simulations.

In order to make a more precise adjustment, one of the first things that should be done is the detailed study of the data that the experiment has collected during its flight in the stratospheric balloon, this being one of the main tasks that must be carried out in the future, because with the data of a single test in the vacuum chamber, that is to say, the TBT, it has only been possible to make a suitable model of the satellite, but not of the convection acting on the experiment plate.

On the other hand, the selection of a certain number of design parameters and the development of some type of algorithm that calculates the optimal value of said walls and the influence that the change in their value has on the thermal behaviour of the set would also be of great useful for making a more precise model, although due to the simplicity of the experiment this work might not be as interesting as in more complex models.

Finally, it should be noted that this model adjustment process has been very fast, for two reasons, the first is the lack of time since obtaining the test results in the vacuum chamber, and the second due to the great similarity that presented the data from the first simulations, a fact that was given by the adequate assumptions that they made based on previous knowledge.

(Page intentionally left blank).

Annex A

Design processes of the Printed Circuit Boards (PCBs).

For the estimation of the properties of the different PCBs that are in the electronics cavity, it has been assumed that these properties will be identical for all electronic devices. This estimate will be made using the results obtained from the Raspberry Pi 3B+, since this is the element about which more information can be found online. It is known that when idle, the Raspberry Pi consumes 1.91 W, while when it is running at full performance it consumes 5.77W [2].

Since thermal images of these two cases are available, as can be seen in the Figure A.1 and in the Figure A.2. The next step is to make a model that fits this temperature distribution as closely as possible. To do this, the board representing the Raspberry has been divided into enough nodes to allow an adequate representation of the temperature distribution.

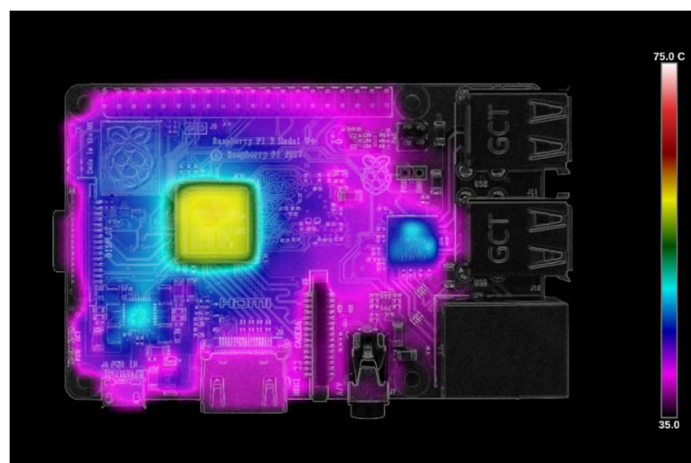


Figure A.1: Raspberry Pi 3B+ heat distribution (load) [2].

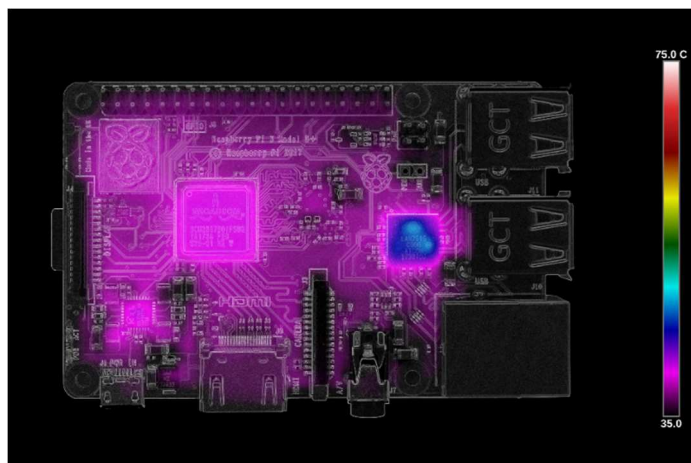


Figure A.2: Raspberry Pi 3B+ heat distribution (idle) [2].

To define the properties, different sources have been searched and the values used in the design of the thermal control of the Spacecraft MIST have been selected to simulate the PCBs [1]. The thermal conductivity through the PCB has a value of $20.5 \text{ W}/(\text{m} \cdot \text{K})$, the density an average value of $2223 \text{ kg}/\text{m}^3$ and an average specific heat of $589 \text{ J}/(\text{kg} \cdot \text{K})$.

However, the solution obtained with these values was not precise enough, so in the absence of suitable sources, the thermal conductivity of the plate has been estimated to achieve a temperature distribution similar to that of the Figure A.1 and Figure A.2.

Finally, establishing a conductivity of $10 \text{ W}/(\text{m} \cdot \text{K})$ and distributing the power dissipated by the plate appropriately (also in an estimated way), the results shown in the Figure A.3 and in the Figure A.4 are obtained.

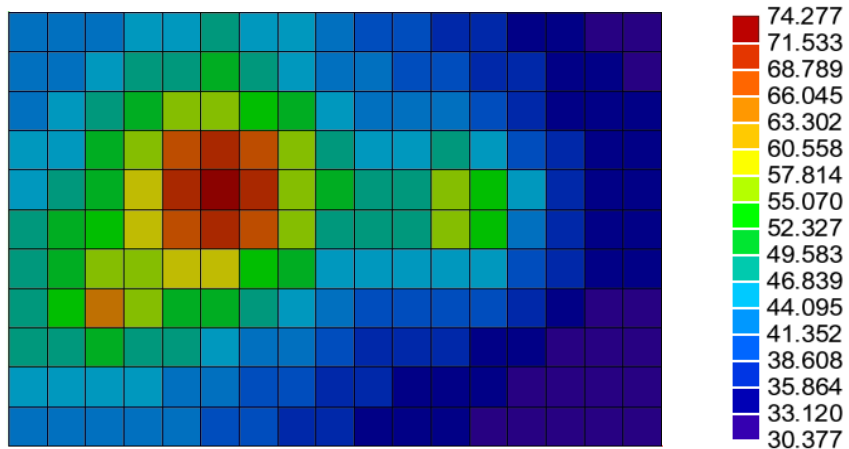


Figure A.3: Achieved temperature distribution on the board (load).

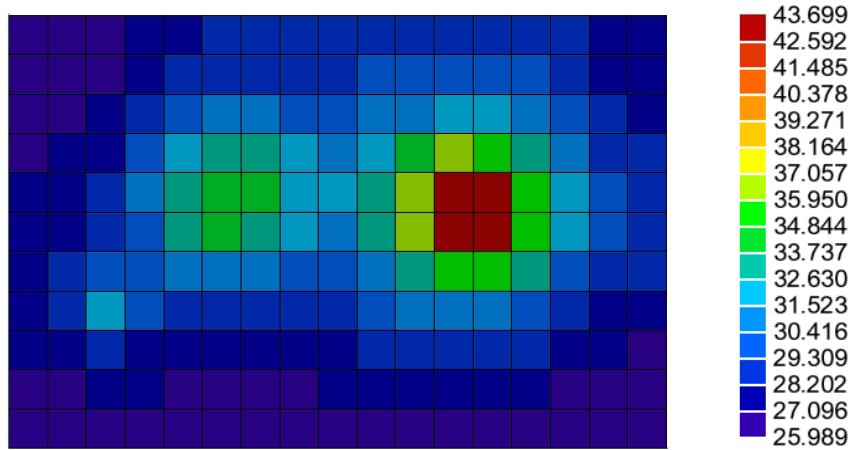


Figure A.4: Achieved temperature distribution on the board (idle).

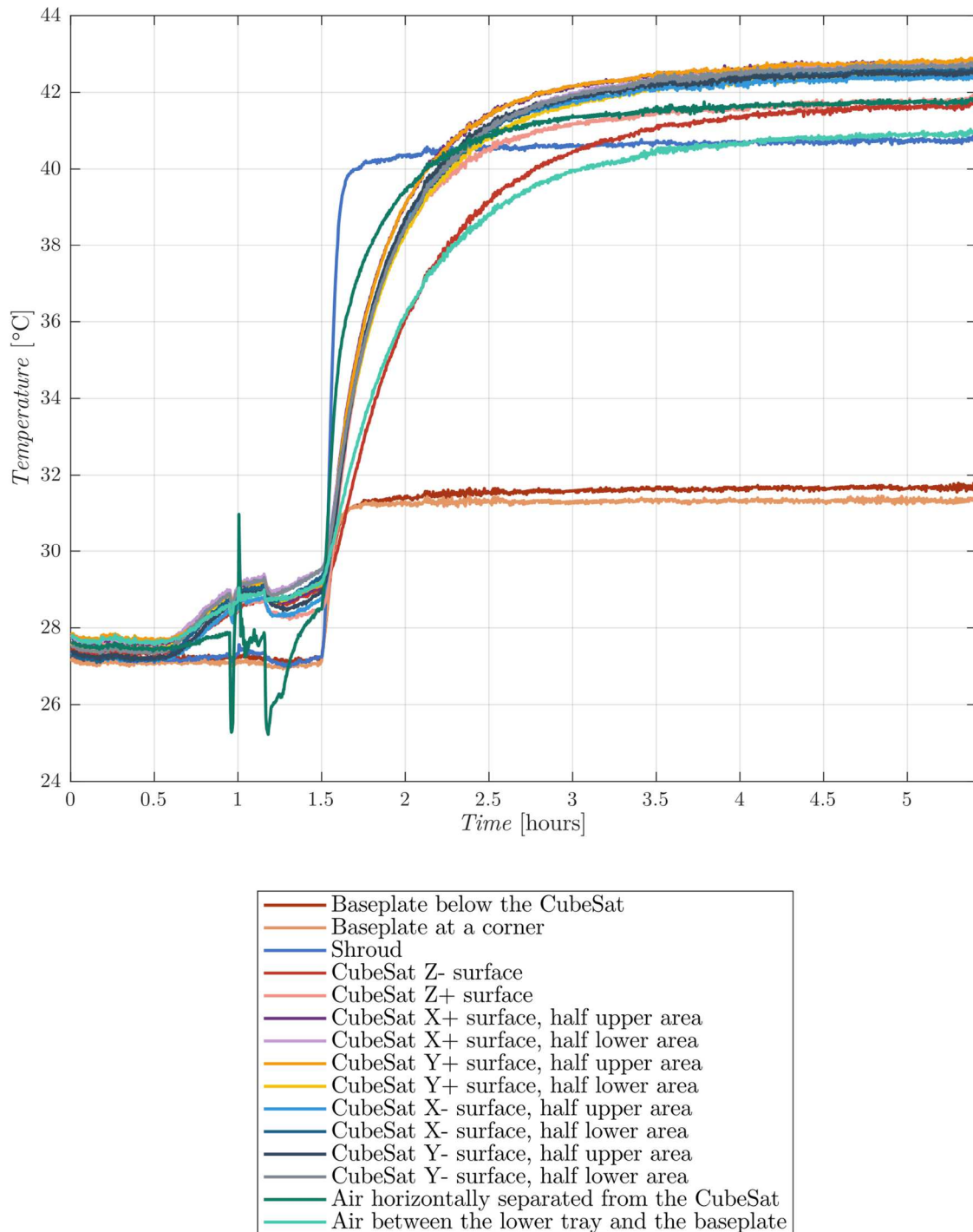
References

- [1] Alex Bate. - *Thermal testing Raspberry Pi 4* - Raspberry Pi Blog. Online, 2021.
<https://www.raspberrypi.org/blog/thermal-testing-raspberry-pi-4/>
- [2] Andreas Berggren. - *Design of Thermal Control System for the Spacecraft MIST* - Stockholm (Sweden), 2015

(Page intentionally left blank).

Annex B

Temperature measurements during the hot case test.



Temperature measurements during the cold case test.